Diss. ETH N° 19765

MRI of the Orbit during Eye Movement

A dissertation submitted to

ETH ZURICH

for the degree of

Doctor of Sciences

presented by

Marco Piccirelli
Dipl. Phys. ETH
born September 30th, 1977
citizen of Prilly (VD), Switzerland and Torricella Peligna (CH), Italy

accepted on the recommendation of

Prof. Dr. Peter Boesiger, examiner
Prof. Dr. Matthias Stuber, co-examiner
PD. Dr. Oliver Bergamin-Rémy, co-examiner

Zurich, 2011

Ai miei Antenati, i cui sacrifici sono riconoscente,
pour Danaé Thalia et Nephélie Maria.

Contents

Abbreviations

1D, 2D, resp. 3D	one, two, resp. three Dimensional
CDENSE	Complementary DENSE
CLEAR	Constant LEvel AppeaRance
CN3	third Cranial Nerve or oculomotor nerve
CN6	sixth Cranial Nerve
CSPAMM	Complementary SPAtial Modulation of Magnetization
CT	Computer Tomography
DENSE	Displacement ENcoding with Stimulated Echoes
DSTI	Duane's Syndrome Type I
DTI	Diffusion Tensor Imaging
DWI	Diffusion Weighted Imaging
EOM	ExtraOcular Muscle
EPI	Echo Planar Imaging
FAcE	FID-Acquired-Echos
fastHARP	fast HARmonic Phase
FEEPI	Fast field Echo with EPI
FFE	Fast Field Echo (gradient echo sequence)
FOV	Field Of View
HARP	HARmonic Phase
IOM	Inferior Oblique Muscle
IRM	Inferior Rectus Muscle
k-t BLAST	Broad-use Linear Acquisition Speed-up Technique
LRM	Lateral Rectus Muscle
MR	nuclear Magnetic Resonance
MRI	nuclear Magnetic Resonance Imaging
MRM	Medial Rectus Muscle
NSA	Number of Signal Average
ON	Optic Nerve
Q-Flow	Quantitative phase contrast Flow measurement
SENC	Strain-ENCoded
SENSE	SENSitivity Encoding
SNR	Signal to Noise Ratio
SOM	Superior Oblique Muscle
SPAMM	SPAtial Modulation of Magnetization
SPIR	Spectral Presaturation Inversion Recovery
SRM	Superior Rectus Muscle
StdDevs	Standard Deviations
T1	spin-lattice or longitudinal relaxation time
T2	spin-spin or transverse relaxation time

T2W	T2 Weighted
TE	Time of Echo
TFE	Turbo Field Echo
TR	Repetition Time
TSE	Turbo Spin Echo
VOR	Vestibulo-Ocular Reflex
WSE	Water Selective Excitation

Zusammenfassung

Ein grundlegenderes Verständnis der peripheren okulomotorischen Pathophysiologie könnte zur Verbesserung der Strabismuschirurgie beitragen. Konventionelle strabologische Untersuchungsmethoden sind hilfreich, um Augenmotilitätsstörungen zu erkennen. Dennoch ist in komplexen Fällen eine präzise Diagnose mit den pathophysiologischen Erkenntnissen, die durch diese Untersuchungen und mit einem quasi agonist-antagonist extraokular Muskel-Modell gegeben sind, nicht möglich; besonders nach einer Chirurgie der extraokularen Muskeln, welcher sich das okulomotorische System anpasst. Das Problem liegt in der Verbindung von Daten der dynamischen Augenbewegung mit statischen Orbitagewebe-Konformationen.

Das unvollständige Verständnis der Umwandlung der neuronalen Steuerungssignale in mechanische Augenbewegungen provozierte eine jahrzehntelange Kontroverse über die aktive oder passive Rolle des orbitalen Bindegewebes, die noch geklärt werden muss. Momentan stehen keine geeigneten dynamischen Daten zur Beurteilung des orbitalen Gewebeverhaltens zur Verfügung, selbst wenn dynamische (Un-)Gleichgewichte existieren, wie z.B. bei Verletzungen des Listingschen Gesetzes während schnellen Augenbewegungen, in bestimmten Fällen. Dies hat, zusammen mit der Komplexität der orbitalen Biomechanik, die Entwicklung eines angemessenen neuro-biomechanischen Orbitamodells verzögert. Gleichzeitige hohe räumliche und zeitliche Auflösung der Kinetik des Orbitalgewebes während der Augenbewegung würde die Umwandlung des neuronalen Signals in eine mechanische Wirkung besser beschreiben.

Daraus ergeben sich die Ziele dieser Arbeit: Erstens soll ein klinisch benutzbarer visueller Reiz entwickelt werden, welcher periodisch wiederholende Augenbewegungen im Inneren des Scanners erzeugt. Damit sollen segmentierte Magnetresonanz-Bilder (MR-Bilder) ohne Bewegungsartefakte in einer genügend kurzen Zeit synchron aufgenommen werden. Zweitens soll die Bildaufnahme mit Hilfe von TFEPI durch Wahl eines reduziertes Sichtfeldes (FOV) und k-t BLAST beschleunigt werden. Drittens soll die Bewegung (CDENSE, CSPAMM) und Geschwindigkeit (Q-Flow) direkt in Bilder der Augenhöhlen kodiert werden, um zusätzliche Bewegungsdaten in der begrenzten Aufnahmezeit zu liefern. Viertens ist die dynamische Verformung der Orbitagewebe durch neue, bildrauschresistente, modellfreie Methoden zu quantifizieren.

Weiter war die Messung der (vermuteten) inhomogenen Kontraktion entlang den Augenmuskeln und die Differenzierung der normalen gegenüber der pathologischen Deformation während den Augenbewegungen ein wichtiges Ziel. Diese neue Messgrößen der Augenhöhlenmechanik und deren Steuerung sollten das Verständnis der Strabismusätiologie verbessern.

Die ersten hoch aufgelösten anatomischen, bewegungs- und geschwindigkeitskodierten Bilder der Deformationsdynamik der Augenhöhlen wurden mit der beschriebenen Methode erfolgreich aufgenommen. Dreidimensionale anatomische und bewegungskodierte MR-Bilder konnten mit hoher räumlicher und zeitlicher Auflösung in weniger als 10 Minuten durch eine Beschleunigung der Bildaufnahme gewonnen werden. Die Verformung des Orbitagewebes während der Augenbewegung konnte quantifiziert werden.

Zum ersten Mal konnten die räumlich-zeitlichen Verformungsmuster des Glaskörpers visualisiert und viskoelastische Modellparameter quantifiziert werden. Verschiedene Arten von Deformationsmustern des Glaskörpers konnten beschrieben werden. Die Viskosität und Elastizität des Glaskörpers wurden durch ein viskoelastisches Modell bestimmt. Somit sind relevante Modellierungsparameter der Augenhöhlebiomechanik in vivo quantifiziert worden.

Die Differenzierung des dynamischen Deformationsprofils entlang der Augenmuskeln von Duane-Syndrom Patienten gegenüber physiologischen Deformationsprofilen erlaubte die nicht funktionellen Segmente der pathologischen Muskeln zu bestimmen und lieferte neue Einblicke in die okulomotorische Steuerung.

Das erweiterte Verständnis der Physiologie des Orbitagewebes und deren neuronalen Kontrollmechanismen könnte bisher unerkannte Ursachen des Schielens klären, welche traditionelle Konzepte verbessern oder alternative Behandlungen vorschlagen könnten. Die Ursachen von Krankheiten wie neuronal bedingte Lähmung, verzögerte neuromuskuläre Übertragung, mechanische Beschränkung und Entzündung der Augenmuskeln voneinander zu differenzieren kann jetzt geplant werden.

Résumé

Une meilleure compréhension de la physiopathologie oculomotrice périphérique permettrait d'améliorer les soins strabologiques. Les méthodes classiques d'investigations strabologiques caractérisent utilement les troubles de la motilité oculaire. Néanmoins, dans les cas complexes, les informations fournies par ces méthodes et la compréhension courante de l'action des muscles extra-oculaires comme paires agonistes-antagonistes ne suffisent pas pour un diagnostic précis. Ceci est d'autant plus vrai à la suite d'une chirurgie orbitale, puisque le système oculomoteur s'y adapte spécifiquement. Le nœud du problème réside dans la combinaison de conformations statiques des tissus orbitaires fournies par l'IRM et les données dynamiques de motilité oculaire.

La compréhension insuffisante de la conversion des commandes neuronales en mouvement oculaire a provoqué une controverse sur le rôle des tissus conjonctifs orbitaux, longue de plusieurs décennies et pas encore résolue. Trop peu est connu sur la déformation dynamique des tissus orbitaires, pour expliquer des (dés-)équilibres dynamiques, comme la violation de la loi de Listing dans certains cas particuliers. Une résolution spatiotemporelle fine de la cinématique des tissus orbitaux durant le mouvement oculaire clarifierait la transformation du signal neuronal en action mécanique et permettrait le développement de modèles neuro-biomécaniques applicable cliniquement.

Par conséquent, les objectifs de ce travail étaient tout d'abord d'obtenir, avec des stimuli visuels cliniquement utilisables, des mouvements oculaires répétitifs afin d'acquérir synchroniquement des images IRM séquentielles, sans flou dû au mouvement et d'une durée d'acquisition suffisamment brève pour maintenir des mouvements oculaires précis. Puis, d'accélérer l'acquisition en utilisant TFEPI, un champ d'acquisition réduit, et k-t BLAST. Et d'augmenter la pertinence des données en codant directement le déplacement (CDENSE, CSPAMM) et la vitesse (Q-Flow).

La dynamique de la déformation des tissus orbitaires a été quantifiée à l'aide de méthodes nouvelles résistantes au bruit des images, et n'utilisant pas de modèle afin d'éviter l'interférence de préconceptions avec de nouvelles découvertes. La différenciation de la contraction musculaire normale (présumée inhomogène) et pathologique (par exemple, syndrome de Duane), devrait améliorer la compréhension de la mécanique orbitale et de l'origine des déficiences de la motilité oculaire.

Les premières images IRM anatomiques, ainsi que codées en déplacement et en vitesse, de l'orbite durant le mouvement oculaire ont été obtenues. En accélérant l'acquisition IRM, des images 3D anatomiques et codées en mouvement avec une résolution spatiale et temporelle fine ont été obtenues en moins de 10 minutes. La déformation des tissus orbitaux a été quantifiée automatiquement.

Pour la première fois, la déformation spatio-temporelle du corps vitré au cours de mouvements oculaires sinusoïdaux a été visualisée. Différentes géométries de déformation ont été révélées. La viscosité et l'élasticité ont été déterminées par l'utilisation d'un modèle viscoélastique du corps vitré. Ainsi, des paramètres pertinents pour la modélisation de la biomécanique orbitale ont été quantifiés.

La différenciation de la déformation des muscles extra-oculaires de patients affectés par le syndrome de Duane et de muscles normaux a permis de spécifier les segments musculaires pathologiques, et de donner un nouvel aperçu du système oculomoteur.

La quantification des paramètres physiologiques des tissus et du contrôle neuronal aidera à clarifier les causes du strabisme, ce qui pourrait remettre en cause les concepts étiologiques traditionnels, motiver des traitements alternatifs, améliorer la modélisation chirurgicale et l'exécution de la procédure optimale. La différenciation étiologique de maladies telles que la

paralysie neuronal, l'altération de la transmission neuromusculaire, la limitation mécanique, et l'inflammation des muscles extra-oculaires peut maintenant être envisagée.

Riassunto

Una migliore comprensione della fisiopatologia del sistema oculomotore periferico potrebbe consentire di migliorare le cure per le malattie neuro-oftalmologiche. I metodi convenzionali d'indagine oftalmici contribuiscono utilmente a individuare i disturbi della motilità oculare. Tuttavia, nei casi più complessi, le informazioni fornite da questi metodi e l'attuale conoscenza della fisiologia orbitale, come ad esempio l'accoppiamento agonista-antagonista dei muscoli extraoculari, sono insufficienti ad ottenere una diagnosi accurata. In particolar modo, dopo l'intervento chirurgico orbitale, poiché il sistema oculomotore si adatta alla cura in modo specifico. Il problema sorge, in quanto, l'ordinaria RM fornisce dati statici della conformazione dei tessuti oculari, mentre i dati della mobilità oculare sono dinamici. Una migliore comprensione della dinamica del sistema oculomotore è quindi richiesta, per perfezionare le procedure chirurgiche.

L'insufficiente conoscenza della conversione dei comandi neuronali nel movimento oculare ha causato una polemica decennale (e non ancora risolta) sul ruolo dei tessuti connettivi orbitali. Troppo poco si sa sulla dinamica della deformazione dei tessuti orbitali per spiegare i disequilibri dinamici, come ad esempio, la violazione della legge di Listing, in alcuni casi particolari. Una misura ad alta risoluzione spazio-temporale, della cinematica dei tessuti orbitali durante il movimento oculare, potrebbe chiarire la trasformazione dei segnali neuronali nell'azione meccanica e consentire lo sviluppo di modelli neuro-biomeccanici clinicamente applicabili.

Il scopo é di differenziare la contrazione muscolare normale (presumibilmente non omogenea) dalla contrazione patologica (ad esempio, la sindrome di Duane), per migliorare la comprensione della meccanica orbitale e dell'origine dei difetti della motilità oculare.

Gli obiettivi di questo lavoro sono stati quindi, di ottenere, con stimoli visivi utilizzabili in clinica, movimenti oculari ripetitivi per acquisire immagini RM senza artefatti da movimento e in tempi di acquisizione abbastanza brevi da avere movimenti oculari accurati durante tutta la misura. L'acquisizione è stata accelerata, utilizzando TFEPI, un campo d'acquisizione ridotto, e k-t BLAST. La pertinenza dei dati è stata aumentata codificando direttamente lo spostamento (CDENSE, CSPAMM) e la velocità (Q-Flow). La dinamica della deformazione dei tessuti orbitali è stata quantificata utilizzando nuovi metodi resistenti al rumore delle immagini e senza adoperare modelli, per evitare interferenze dei preconcetti sui nuovi dati.

Per la prima volta sono state ottenute immagini RM anatomiche e immagini codificate in movimento e velocità dell'orbita durante movimento oculare. Accelerando l'acquisizione RM, è stato possibile misurare, in meno di 10 minuti, immagini 3D anatomiche e codificate in movimento con un'alta risoluzione temporale e spaziale. La deformazione dei tessuti orbitali è stata quantificata automaticamente.

Per la prima volta la deformazione spazio-temporale del corpo vitreo durante movimenti oculari sinusoidali è stata visualizzata. Diverse geometrie di deformazione sono state rivelate. La viscosità e l'elasticità sono state determinate utilizzando un modello visco-elastico del vitreo. Quindi, parametri rilevanti per la modellazione della biomeccanica orbitale sono stati quantificati.

La distinzione delle deformazioni dei muscoli extraoculari dei soggetti sani e dei soggetti affetti dal sindrome di Duane, ha permesso di individuare i segmenti muscolari patologici e dare una nuova visione del sistema oculomotore.

La quantificazione dei parametri fisiologici dei tessuti e del loro controllo neurale aiuterà a chiarire le cause dello strabismo, rivoluzionare i concetti etiologici tradizionali e motivare trattamenti alternativi. La rivelazione di parametri nascosti e di caratteristiche insolite dei tessuti orbitali potrà migliorare la modellazione chirurgica, per assistere il medico nella pianificazione ed esecuzione della procedura ottimale. La distinzione etiologica di disabilità dovuta a paralisi

neuronale, trasmissione neuromuscolare deficiente, limitazioni motorie, o infiammazioni dei muscoli extraoculari può adesso essere considerata.

Summary

A better understanding of the peripheral oculomotor pathophysiology would improve the treatment of ocular misalignment and, in particular, make surgery more effective. While conventional strabological investigations have usefully characterized most eye motility disorders, in complex cases an adequate diagnosis is not possible with the pathophysiological insight given by these investigations. Quasi agonist-antagonist extraocular muscle (EOM) models are insufficient, especially after EOM surgery to which the oculomotor system adapts. The combination of eye movement data with static orbital tissues conformations is problematic.

The missing understanding of the conversion of neuronal commands into eye movement has provoked a decades long controversy about the role of the orbital connective tissues. No appropriate dynamic data of the orbital tissue deformations are available, even where dynamic (dis-)equilibrium exists, like the violation of the Listing's Law during saccades. This, added to the complexity of the orbital biomechanics, has inhibited the development of neuro-biomechanically adequate eye plant models. High spatiotemporal resolution data of the orbital tissue kinetics during eye movement would clarify the transformation of the neuronal signal into a mechanical action.

Aimed was, thus, the differentiation of the normal (presumably inhomogeneous) EOM contraction from pathologic (e.g., Duane's syndrome) EOM deformation during eye movement, to provide new observables for clinical models of the orbital mechanics and eye movement control, and thus to improve the insight into the orbital mechanics and origins of eye misalignment.

Therefore, the objectives of this work were to obtain, with a clinically usable setup for visual stimuli presentation, repetitive eye movements inside a MRI scanner in order to synchronously acquire segmented MR images, without motion blurring, in a scantime short enough to maintain accurate eye movements. Image acquisition was accelerated using TFEPI, reduced FOV, and k-t BLAST. The relevance of the data acquired in the limited scantime was increased using motion (CDENSE, CSPAMM) and velocity (Q-Flow) images of the orbit. Dynamic orbital tissue deformation was quantified using new, image noise resistant, model-free tracking methods, to avoid a priori conceptions to interfere with new discovery.

The first high-resolution anatomical, motion- and velocity-encoded images of the orbit during smooth pursuit eye movement were obtained. Three-dimensional anatomical and motion-encoded MR images with high spatiotemporal resolution could be acquired in less than 10 minutes by accelerating the image acquisition. The orbital tissues' deformation during eye movements was automatically quantified.

The spatiotemporal deformation pattern of the vitreous during sinusoidal eye movement could be visualized and visco-elastic model parameters quantified. Different types of vitreous deformation patterns were revealed. The vitreous viscosity and elasticity were determined by fitting to the vitreous deformation a viscoelastic model. Parameters relevant for the modeling of the biomechanics of the orbit were quantified.

The differentiation of the dynamical deformation pattern along the EOMs of Duane's syndrome Type I patients from physiological EOMs during eye movement determined which segments of the EOMs were behaving pathologically, and gave new insights into the oculomotor plant.

New access to tissue physiology and neuronal-control may clarify causes of strabismus that are challenging traditional etiology concepts and suggests alternative treatments. Differentiation of diseases such as neural palsy, impaired neuromuscular transmission, mechanical restriction, and inflammation of the extraocular muscles can now be intended.

Chapter 1: Introduction

1.1 Research Area

> *"The outcomes of surgeries to correct disabling movement abnormalities are unpredictable, and sometimes unsuccessful. Theoretically, patients' abnormal movement patterns can be improved by identifying the biomechanical factors that contribute to abnormal movement and designing treatments accordingly. However, many factors can contribute to the abnormal movement. For example, persons with cerebral palsy exhibit disturbances in voluntary control, [other examples are: ...] static muscle contractures, bone deformities that alter muscle paths, and limb malalignment. Current diagnostic methods do not allow clinicians to reliably differentiate between the potential causes of abnormal movement to determine the most appropriate treatment."[Blemker, et al. 2007]*

This introductory statement given by Blemker, et al. in their recent review on image-based musculoskeletal modeling could, mostly, also apply to the outcomes of orbital surgery for complex strabismus etiologies. Nevertheless, the general problem of correcting pathological biomechanical plants with surgery is a crucial and quotidian problem of the strabology clinical routine. Therefore new and exhilarating insights and solutions for this problem are sought.

To have a thorough understanding of the human biomechanical plants, to construct detailed functional models of its neural control, and to comprehend its physical interaction with the environment, will have a profound impact on numerous domains relevant for our actual society. The virtual (artistic) simulations of dynamic reality, bio-inspired robotics,[Pfeifer, et al. 2007] and the understanding of human movement in science and medicine would be revolutionized,[Pai 2010] including diagnosis of residual function following neuronal, muscular, or orthopedic injuries.[Dovat, et al. 2010] Surgical planning, rehabilitation,[Nef, et al. 2009] and control of neuroprosthetics[Tillery and Taylor 2004] would also benefit from such developments.

One of the most interesting biomechanical plants of the human body,[Schovanec 2001] the oculomotor system, controls the eye movements and maintains gaze alignment and synchronization. This system includes neuronal (central and peripheral) and mechanical components such as the extraocular muscles (EOMs) and connective tissues. A particularly striking observation is that the eyes have to move to give us a big share of our sensory inputs,[Oyster 1999a] upon other also for the perception of movements in the environment. This motion perception-execution duality, as well as its particular bony architecture (at the periphery of the plant and not at its center), and the relatively low number of muscles involved (only six per eye) makes it privileged for biomechanical and perceptual studies. Therefore it is not surprising that orbital biomechanical hardware models were already developed by Theodor Ruete during the nineteenth century,[Simonsz 2004; Keeler, et al. 2009] and was also reported by Hermann Helmholtz.[Helmholtz 1856]

The clinical relevance of eye movements is conspicuous, as well as the importance of the sensory input provided by the eyes, and the social interactions involving the eyes.[van de Graaf, et al. 2009] Clinical care of eye movement disorders is not simple, since the EOMs are not purely ordered in an agonist-antagonist fashion. Therefore, the concurrent action of all six muscles has to be considered for almost any eye movement. For example, the superior and inferior rectus muscles (SRM, IRM) are able to induce horizontal eye movements, and the oblique muscles are

activated during horizontal and vertical eye movements. Further, the orbital connective tissues play a crucial role in muscular force development, and the control of the EOMs of both eyes as well as the head movements have to be synchronized; which drastically increases the number of actuators.

The complexity of EOM interactions becomes clearer in pathologies. Abnormal up- or downward eye movements are often associated with pathological horizontal eye movements. The surgery of one eye muscle is often not sufficient to correct eye movements' deviations, so usually several muscles are modified during strabismus surgery. Pathologic eye movements are diagnosed mostly through their symptomatic impact on the eye movements themselves. Pathologic EOMs are investigated mostly through their effect on the eye movement and only rarely is EOM imaging performed, even if it has been proven to be a valuable information source for diagnosis.[Demer, et al. 2002]

In this introductory chapter, the role of imaging in the development of dynamic biomechanical understanding will be shown. The introduction will consider optical, X-ray, and MRI techniques, and chronologically summarize, on chosen examples, the development of methodological ideas for motion imaging, and show how similar ideas re-emerge for each imaging technology. The developments of motion imaging techniques that have led to the imaging methods used in this thesis will be presented. A review of the ophthalmological issues that motivated this work, as well as of the previous attempts made to resolve these will then be presented. Finally, a brief outline of the approach used to achieve the objectives of this work will conclude this chapter.

1.1.1 Biomechanical Modeling in Need of Observables

One of the aims of biomechanical modeling is to understand how the central nervous system controls movements.[Pai 2010] Nevertheless, some of the movement features and coordination may be controlled at a peripheral level, directly by the biomechanical plant itself.[Demer 2002] To understand and thereby create useful models of biomechanical systems, insight into the function of its constituents is required.[Schovanec 2001] The coordination of such systems is intricate and takes place in a large scale biomechanical system, with numerous muscles, connective tissues, and bones, for which non-invasive in vivo measurements of their properties is needed.[Sheehan, et al. 1997]

The muscular insertion is a complex network of tendons and connective tissues, which could couple the action of different muscles, in a nonlinear three dimensional (3D) conformation. A commonly known example of this complexity is the hand, but even for the apparently simple oculomotor system a complex architecture of connective and disperse smooth-muscles tissues might contribute to the eye movement control.[Robinson 1975] Even though it is believed that these structures are functionally important, their precise function is still subject to controversy.[Jampel 2009; Piccirelli, et al. 2009b]

The neuronal control of the mechanical components is also complex. The proprioceptive information from muscle spindles and golgi tendon organs, has to be modeled from the strains, strain rates, and stresses within muscles.[Windhorst 2007] Moreover, properties such as mass, elasticity, viscosity, and motorneuron activation can vary within the muscles and other tissues, as well.[Schoemaker, et al. 2006]

Models of the human orbit with realistic anatomy, including the EOMs, connective tissues, pulleys, ligaments, and dynamic tendon sheaths and contact constraints, have to generates realistic gaze positions and trajectories given neuronal command, and even simulate pathologies.[Haslwanter, et al. 2005] But in addition, muscle and connective tissue models have to be incorporated and represent in detail their mechanical action,[Pai 2010] as well as the tissue inhomogeneous properties,[Pappas, et al. 2002; Drost, et al. 2003; Blemker, et al. 2005; Wakeling 2009; Lopata, et al. 2010] as the surgeon will act on these constituents of the oculomotor system.[Bergamin, et al. 2008]

More generally, models of biomechanical and neuronal systems should be able to predict mechanical or chemical results on which their model parameters can be tested.[Prompers, et al. 2006] Thereby, the dynamics, and not only the statics[Demer 2008a] or kinematics, of biomechanical systems have to be modeled, to understand the orbital biomechanics and to adequately treat disorders. Nevertheless, the precise function of the orbital tissues is still subject to controversy,[Demer 2008b] mostly because of the absence of dynamical data of the orbital tissues on which models could be tested upon their performance,[Abramoff, et al. 2000] and the resulting lack of motivation in creating usable models of its dynamic physiology and surgery simulations with realistic anatomy and (dynamical) functionality.[Schutte, et al. 2006]

1.1.2 Imaging Motion

To answer the need to test biomechanical models with data, and to quantify biological movements, several methods have been developed in the last few centuries. Thereby, the improvement of the spatial and temporal resolution, as well as the minimization of the disturbance of the observed system by the imaging methodology, has been a continuous concern. Noteworthy is that these physiology-research driven technological developments gave rise to new type of arts, the photography (from the Greek fotografia - φωτογραφία, with the roots: phos - "light" and graphi "write" or "drawing") and the "Cinematography" (from the Greek: kinema - κίνημα "movement" and graphein - γράφειν "to record"). With the development of methodologies able to measure non-invasively movements inside the body, this field of research reached clinical relevance. To better understand the motivation for movement imaging techniques, I will briefly summarize the prior situation.

1.1.2.1 Before the Development of Imaging Techniques

The study of biological movements - in a broader understanding - was already a concern at the time of Galen (* ~129 in Pergamum; † ~216 in Rom), a Greek medical doctor and anatomist. Galen was able to expose a human beating heart during the operation of a patient suffering from chronic osteomyelitis of the sternum, and revealed the movement of the heart.[Keele 1961] Nevertheless, no graphical report of this movement was reported by Galen. Galen used words to describe his observations.

In his article of 1961, Keele states that:

> *"For some mysterious reason the fashion for experiment amongst the intelligentsia of Rome died with Galen. And until the Renaissance the quest for experimental knowledge, apart from isolated examples from men like Roger Bacon, seems to have been quenched by the Christian and Moslem faiths. One of the first to break through this barrier into experiment was Leonardo da Vinci, whose methods, like so many of his other activities, were unique."[Keele 1961]*

Leonardo da Vinci was imbedded in the artistic culture of his time, and he therefore reported his experiments and observations mostly graphically. This is a great step for the objectification of scientific data report. This is also the beginning of the graphical representation of movement. This artistic approach of anatomy and physiology gave a new and different impulse than the one given by the medical profession. Keele recount the episode where Leonardo da Vinci inserted a dagger into the chest of a pig to depict the heart movement:

> *"Apart from the pithing of a frog, not one of his experiments in physiology was performed on living animals. An apparent exception, the well-known observations of the movements of the knife or 'spillo' in the hearts of dying pigs, were made by him as he watched the routine slaughtering of these animals in the abattoir."[Keele 1961]*
>
> *"... he noted the movement of the handle corresponding to systole and diastole of the pig's heart. Though he observed correctly from these movements that the heart shortens in systole he failed to follow up these observations and still continued to believe that the cardiac impulse was produced by narrowing and lengthening of the heart as was the Galenic tradition."[Keele 1951]*

The graphical description of the movement of this dagger lays the basis of the representation of biological movement. Leonardo's preoccupation was the mechanical significance of what he dissected. The geometrical description of the action of the forces was therefore inevitable. Drawing will remain a tool of biology - and of most scientific disciplines - for centuries. This tracing of the biological movement will be continued and objectified at the beginning of the 19th century.

Another tremendous input from Leonardo for the imaging of motion resulted from its investigation of the optical characterization of the eye, as stated by Keele:

> *"... the study of the eye in relation to light (Fig 2), making models of the cornea and lens, and placing his own eye in the position of the optic nerve, where he considered the sensitive part of the retina should lie. It was during these experiments that he discovered the camera obscura, which was constructed merely incidentally as part of his model of the human eye."[Keele 1961]*

The camera obscura laid the basis for the development of the photographic camera. However, it is not clear if Leonardo was the first to discover the principle of the camera obscura.

Finally, a third input of Leonardo was the tagging of a material to reveal its (internal) movement. Leonardo made *in vitro* - in glass - models of the aorta to conduct cardiac flow experiments. He tagged the water used for simulating the blood with grains of panic grass *"because by the movement of these grains you can quickly know the movement of the water that carries them with it."* p.80 of [Keele 1952]. The idea of tagging will be rediscovered for each method used to depict biological movement presented below.

To conclude this section, the work of the Weber Brothers published in 1836 gives a snapshot of the situation just before the development of imaging methods. These two brothers worked in an interdisciplinary team: Wilhelm Eduard Weber (*1804; †1891) was a well-known German physicist, friend of Carl F. Gauss, and his brother Eduard Friedrich Weber (*1806; †1871) was a physiologist und anatomist. The report of their work, titled *Mechanik der menschlichen Gehwerkzeuge* - recently translated,[Weber and Weber 1992] gives a good review of the artistic, social, scientific and medical implications of motion imaging. Especially, the psychological background of "living automates" at that time is interesting; see e.g. *Der Sandmann* of E.T.A. Hoffmann.

In contrast to the work of Leonardo, the Webers made numerous quantitative measurements. They also derived rules for gait, like the relationship of the size and height of steps to the speed and frequency of the movement. They also tried to determine the relevant parameters of the difference between walking and running. While their results are quite interesting, the methodology used to obtain them is poorly explained. The drawings made of a walking man, are astonishingly similar to the photographs that Marey will make half a century later. Even the idea of tagging, or at least of diminishing irrelevant information to better disclose relevant particulars, was presented in almost the same way as Marey and Demeny will present their results. Nevertheless, the slight but important difference in the gait between the data of the Webers and the photograph from Marey, show the importance of observer-free imaging of biological movement.

1.1.2.2 The Development of Imaging Techniques of the Motion

The French physiologist Etienne-Jules Marey (*1830;†1904) was a "medical engineer" who developed many technical innovations and applied new scientific methods to the experimental study of biological motion. Before using light to image motion, he developed several mechanical tools to draw the movement of biological tissues. He was able to replace the artistic talent of Leonardo da Vinci with the objectivity of a mechanical tool. His work best explain the evolution on motion imaging in the 19th century. Of course, several other researchers did similar developments, e.g. Carl Ludwig in Leipzig and Angelo Mosso in Turin, with who Marey interacted.

In 1860, Marey presented the sphygmograph, able to measure the blood pulse pressure on the vessel walls and to represent the results graphically (see Figure 1.1). From the curves, he tried to recognize pathologies. His work is based on the sphygmograph presented in 1854 of the physiologist Karl von Vierordt (*1818;†1884).[Marey 1876] Since 1877 the pulse-watch of Waldenberg (†1881) supplanted the sphygmograph.[Waldenburg 1878; Jaffe 1882]

Five years later, in 1865, he applied a similar technique to the measurements of the heart pulsations. To minimize the inertia added by the measuring tool, he used pneumatic transmission of the force (see Figure 1.2).

Some months later, he was able to report measurements of the skeletal muscles contraction (see Figure 1.3). In the 1870's, Angelo Mosso used similar setups to measure the cerebral blood perfusion.[Ladecola 2004]

The time evolution is omnipresent in these graphical representations, this is maybe the reason why Marey called his photographic imaging technique "*chronophotograpy*".

Similar setups were also used at the end of the 19th century to record eye movements. Fixating a lever to the eye ball, Ahrens,[Ahrens 1891] Delabarre,[Delabarr 1898] and Huey[Huey 1898, 1900] obtained traces of the saccades occurring during reading and writing. But, soon after, non-invasive optical methods were developed. Other methods, based on electromagnetic technologies, were later developed and have some advantages (better spatiotemporal resolution and accuracy) over optical methods.[Robinson 1963]

The Use of Visible light to Image Object in Motion - from the First Image of Motion to the Cinematography

A new idea that emerged during the 19th century was to minimize the perturbation of the investigated motion by sensing it with light. Light will have none of the force transduction and inertia problems of the hardware setup illustrate above. Nevertheless, the ensuing technical issues needed almost all the 19th century to be solved.

As stated before, the development of photography is based on the camera obscura principle. The issue was to be able to fix the image chemically and later also automatically, without human intervention.

Thomas Wedgewood, in 1802, used silver-nitrates to fix the image on a hard support. This print lasted only a couple of hours if observed with candle light. Nicéphore Niepce is awarded the title of the first photographer: in 1826 he used a zinc-asphalt technology to obtain a photograph, after an exposure time of eight hours. With such long imaging times, only very slow or repetitive movements can be imaged. Using this "segmented acquisition principle", in 1865, Onimus und Martin made the first photographic image of a beating heart.[Weiss 1906] On the obtained pictures, only the extreme positions - systole and diastole - can be delimited. The intermediate positions are blurred (see Figure 1.4).

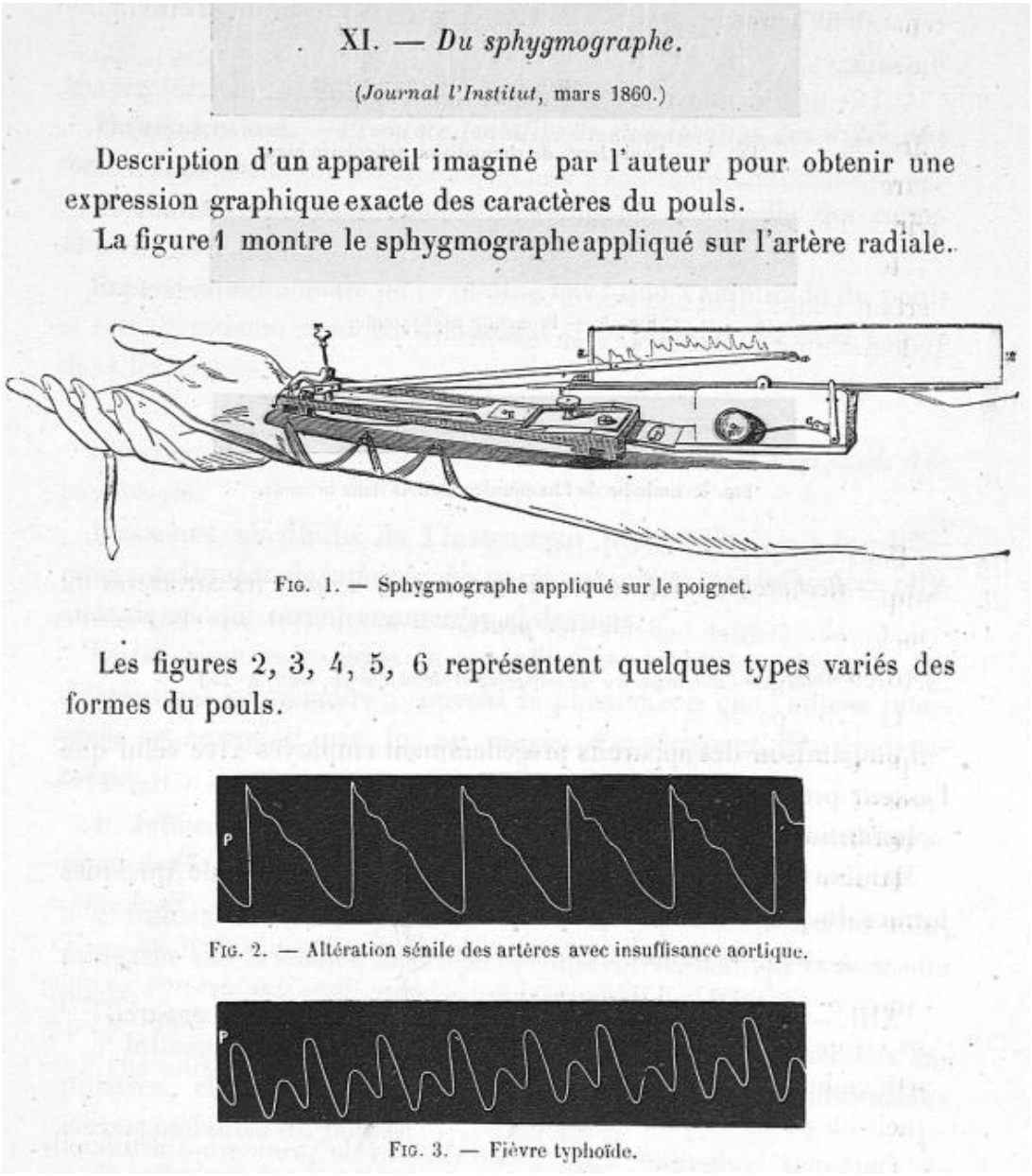

XI. — *Du sphygmographe.*

(*Journal l'Institut*, mars 1860.)

Description d'un appareil imaginé par l'auteur pour obtenir une expression graphique exacte des caractères du pouls.

La figure 1 montre le sphygmographe appliqué sur l'artère radiale.

FIG. 1. — Sphygmographe appliqué sur le poignet.

Les figures 2, 3, 4, 5, 6 représentent quelques types variés des formes du pouls.

FIG. 2. — Altération sénile des artères avec insuffisance aortique.

FIG. 3. — Fièvre typhoïde.

Figure 1.1: Drawing of Marey's sphygmograph and obtained vessel pulsations traces. Reproduced from [Marey 1876].

Chemical developments, such as the use of silver bromide-gel, by Ottomar Anschütz, enabled a drastic reduction of the acquisition time to below one second. This enabled Eadweard James Muybridge, in 1873, with the use of a large number of cameras to acquire the world known running horse images (see Figure 1.5). Nevertheless, the horse gait is acquired over several steps and the time delay between the acquisitions is not controlled.

A first step in towards dynamical images was the use of a stroboscopic or an on/off shutter by Joseph Plateau in 1833. At this point dynamic imaging use on photographic plate illuminated several times (see Figure 1.6).

In 1873 Janssen used this principle to control the timing of photographs of the planet Venus as it passed in front of the sun.[Janssen 1876] Later, Janssen used its "astronomical gun" for the study of animal motion.

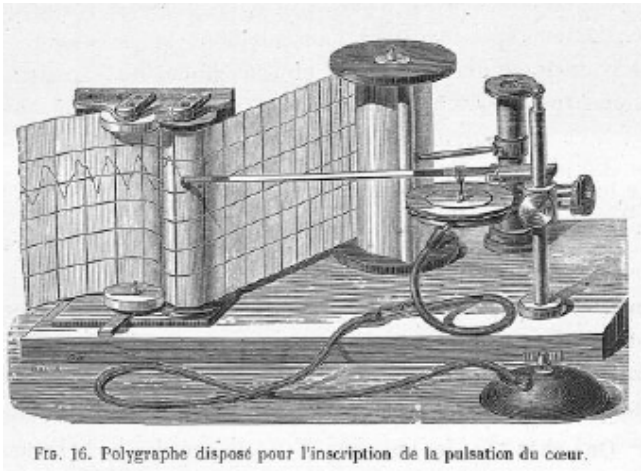

Fig. 16. Polygraphe disposé pour l'inscription de la pulsation du cœur.

Figure 1.2: Drawing of a device used to trace the heart pulsation. Note the pneumatic transmission of the pulse reduces the inertia of the system. Reproduced from [Marey 1865].

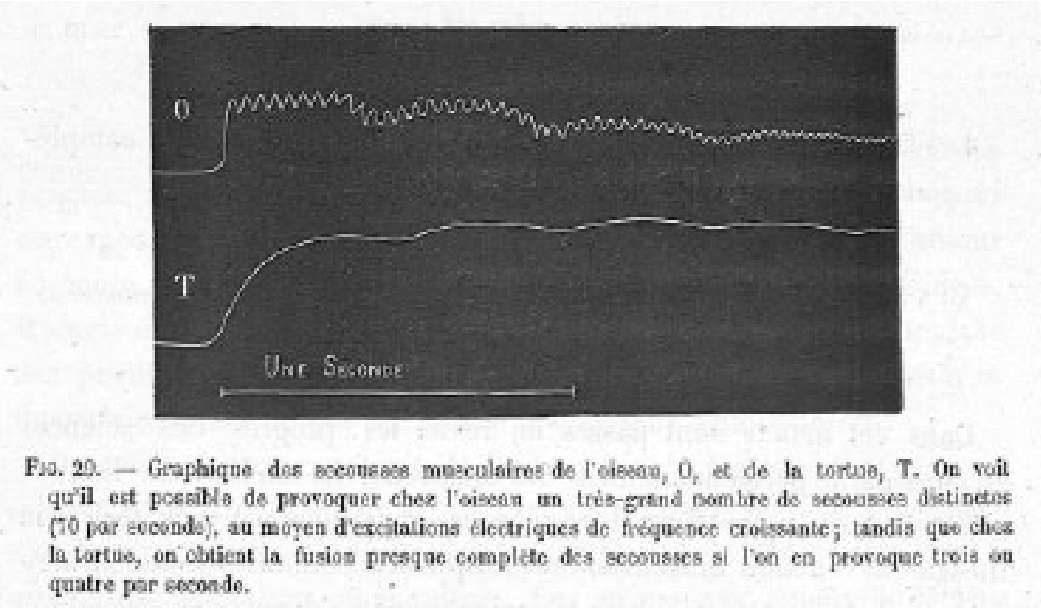

Fig. 20. — Graphique des secousses musculaires de l'oiseau, O, et de la tortue, T. On voit qu'il est possible de provoquer chez l'oiseau un très-grand nombre de secousses distinctes (70 par seconde), au moyen d'excitations électriques de fréquence croissante; tandis que chez la tortue, on obtient la fusion presque complète des secousses si l'on en provoque trois ou quatre par seconde.

Figure 1.3: Traces of the muscular contraction waves of electrically excited skeletal muscles. Here, the different contraction frequencies of bird and turtle muscles are compared. Reproduced from [Marey 1866].

In 1882, Etienne-Jules Marey improved this setup and made it portable. His chronophotograph looked pretty much like a gun and was called a "fusil-photographique". It used a single photographic plate partially illuminated several times, so that the images were not overlapping. A clockwork rotated the photographic plate, and several images per second were obtained. Each snapshot acquisition last one millisecond. Marey studied flying birds, motivated by the French State goal to construct flying machines. In his Institute for physiology he also studied the human locomotor system. Georges Demeny aimed the application of this physiological studies to the physical education in schools and in the army.[Marey 1890] Marey imaged white objects in front of a dark background, too.

Like the tagging of water by Leonardo da Vinci, here too, tagging was used to diminish the quantity of irrelevant data, and ease the quantification of the motion parameters (see Figure 1.7).

Figure 1.4: The first photographic images of beating hearts. On the left a turtle heart and on the right a rabbit heart are depicted. From these images, the error made by Leonardo da Vinci is obvious: the heart shortens during its contraction. Reproduced from [Weiss 1906].

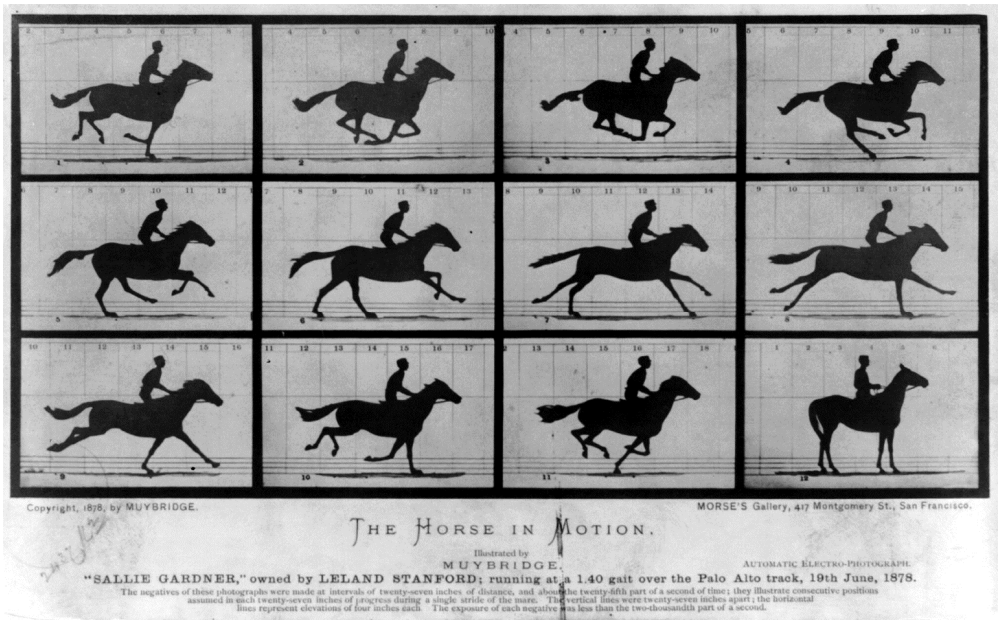

Figure 1.5: The Horse in Motion by Muybridge is still an object of fascination: the Tate Britain exhibited a retrospective of Muybridge's work, from 8.9.2010 to 16.1.2011.[Brookman 2010] Muybridge work is a good example of the coupling of science and art. Note that the horse gait is acquired over several steps and the time delay between the acquisitions is not controlled.

Parallel imaging to unfold images as well as to accelerate the image acquisition, by up to a factor of 16, was developed by Marey, too (see Figure 1.8).

Even 3D reconstruction with a stroboscopic illumination and several cameras around the subject in motion was possible. 3D reconstruction of chronophotographic data of a running man with a tagged suit were build.[Weiss 1906]

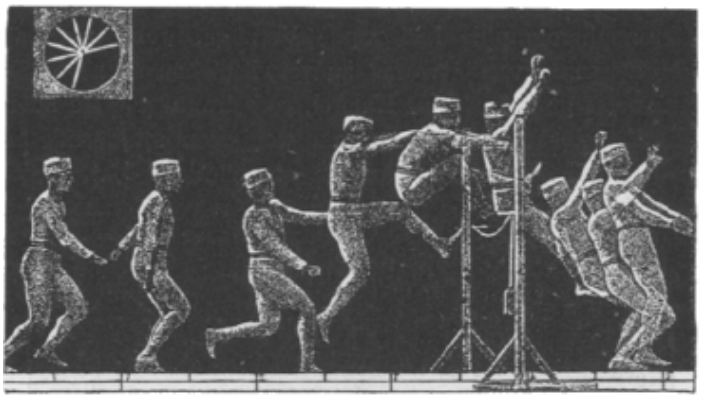

Figure 1.6: Chronophotographic images of a jumping man. The difference between the static and the dynamic conditions is here obvious. At the slower part of the movement, several postures are overlapping. Note the clock on the upper left corner of the image. Reproduced from [Weiss 1906].

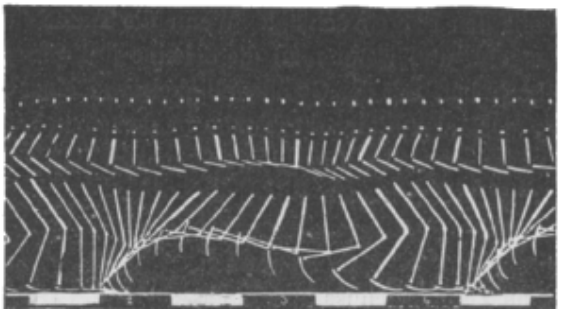

Figure 1.7: Chronophotographic images of a running man. To avoid the overlapping of posture and to facilitate the tracking and quantification of the movement, the photographed subject wore a black suit with white lines on it. Notice that only the right limbs were tagged. Reproduced from [Weiss 1906].

These works found also their applications, where human or animal physical work was analyzed.[Spielberg 1934; Schmitt, et al. 2010]

The following developments of an automatically exchange of the photographic plates was based on the celluloid support developed by John W. Hyatt in 1869. 18 years later Hannibal Goodwin used nitrate on celluloid to produce a soft image support called "film". These industrial developments were used in 1887 by E. J. Marey to invent the pellicle chronophotograph. In 1889, G. Eastman improved this soft support technology which he delivered to Thomas Edison and William K.L. Dickson, which had the idea of perforating it to ease its feed into the camera.

Optical imaging of the eye movements, avoiding mechanical contact with the eye, was developed by R. Dodge and T.S. Cline. They used the corneal reflection of a bright line on a moving photographic plate.[Dodge and Cline 1901] Pioneering work on photographic imaging of the eye movements were made by G.A. Brecher.[Brecher 1934] Optical methods for eye movement recordings are now quite easy to perform with sub-milliseconds time resolution and less than one degree uncertainty on the gaze angle determination. Optical recordings of eye movements are widely used in many field of research. Psychologist and behavioral scientists use eye movement recordings to infer about attention and expectation. Biomechanical modelers and neurologists use the same technique to understand eye movement control. The limitations of optical measurements lay in the problematical determination of the third degree of freedom of the eye movements: the torsional angle - primarily generated by the oblique eye muscles. To determine the torsional angle scleral search coils are used.[Robinson 1963; Bergamin, et al. 2001; Pfenninger, et al. 2006] An overview about eye movements recordings methods is given in [Eggert 2007].

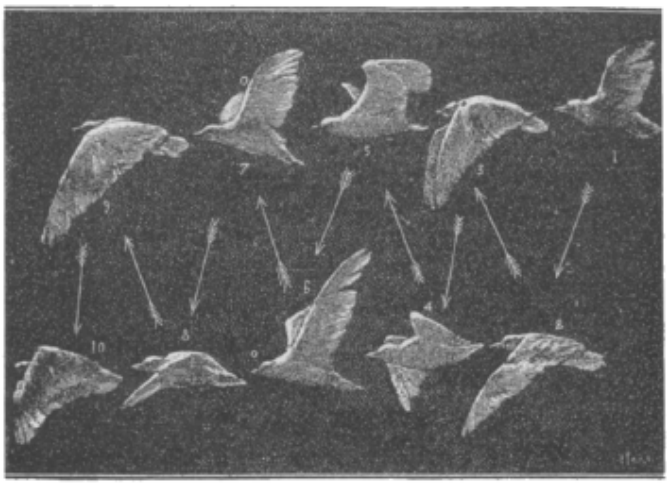

Figure 1.8: To avoid the overlap of images a parallel photographic technique was developed and allowed a twofold increase of image acquisition speed. Reproduced from [Marey 1890; Weiss 1906].

The Dynamic Representation of Images and the Illusion of Movement

To be able to obtain a good insight on the mechanical systems studied with the chronophotograph, Marey affirmed the need of a dynamic visualization of the image series. The development of such visualization tools lasted several centuries and had a tremendous impact on our society. Already in 1671, the Jesuit Athanasius Kircher described the magic lantern (the first image projection device) in its *Ars magna Lucis & Umbrae*. Kircher used it to impress Christians and bring them back on the "right road". After the mysticism of these images' representations had disappeared the British mathematician William George Horner invented the zoetrope in 1834, to give the illusion of movement. In 1881 E.J. Muybridge animated his images using the projection praxinoscope - device similar to a projector with a turning wheel on which the photos are placed - developed one year before by E. Reynaud. This enabled the better understanding of the biomechanical systems such as the running horse.

The show business around dynamical imaging gave a great motivation in the development of new photographic techniques. The diversity and parallelism of inventions and related patents, as well as the industrial espionage and plagiarism are the testimony of this intense activity. Even within scientific laboratories developing such dynamical imaging, the claim of invention was the source of confrontations. An example of this monetary interest is given by Jacques M. Daguerre, who used in his theater images obtained with a cupper-silver technique in 1837. Two years later, the French State representatives were so impressed about this imaging technique, that Daguerre received a lifelong pension for the public domain licensing of the Daguerreotype. At the end of the 19th century, the last "home stretch" of this long-lasting competition opposed on one side T. Edison and W.K.L. Dickson, who developed a one-man theater in 1891, and on the other side the Brothers Lumière who developed a new pellicle automation system and, with E. Moisson, a prototype able to register, develop, and project films. In 1895, The Brothers Lumière patented the cinematograph (February), and made the first public and charged cinematographic projection in Paris (28 December). They preceded Edison by a couple of months. The imaging of motion with light was mature enough to let the artistic productions begin. Georges Méliès's Voyage dans la Lune, in 1902, is a famous example, where the moon would need an ophthalmologist.

The Discovery of X-rays and the Clinical Use of Imaging

Due to the interest in photography, and the corresponding industrialization of its production, the use of photographic plates was widespread. Heinrich Hertz and Philipp Lenard in 1892 noticed the darkening of a photographic plate in the vicinity of a cathode-ray tube, but without giving a great concern to it.

In 1895, the physicist Wilhelm Conrad Roentgen independently from Hertz and Lenard, was the first to scientifically investigate this phenomenon.[Rontgen 1895] The century long scientific interest on biomechanical imaging preceding the discovery of Roentgen prepared the technical and intellectual background for the rapid application of the X-rays to medicine within less than a month after his seminal paper. Due to the good contrast of bone relative to soft tissue, the bones biomechanics could be investigated, extending the work begun by Leonardo da Vinci.

3D image reconstruction developed for the chronophotograph and further developed to solve the nuclear decay localization problem,[Moore 1948; Wrenn, et al. 1951] was further improved for tomographic image acquisition and reconstruction using X-rays.[Cormack 1963; Hounsfield 1973] This enabled the better localization and volumetric depiction of tissues, e.g. in the orbit.[Ambrose, et al. 1974; Gawler, et al. 1974; Forbes, et al. 1982]

For the first time, the imaging of the beating heart was possible non-invasively.[Lipton, et al. 1984] In 1985, H. Simonsz, et al., revealed with X-rays computer tomography (CT) the sideways displacement and the curved path of rectus eye muscles in ab- or adduction.[Simonsz, et al. 1985] This discovery set the beginning of multipositional or "*cine*" imaging of the orbit. Tagging is also possible within the X-rays technology, but only with exogenous contrast agents - e.g. for quantitative perfusion measurements - or metal markers. Recently, Joel Miller et al. used gold beads implanted into monkeys orbits as displacement markers, and the same multiframe technique as for 3D optical imaging was used to reconstruct the 3D location of the gold beads.[Miller, et al. 2006]

Clinically, CT is more appropriated than MRI to assess orbital fractures or metallic intra-orbital foreign bodies, bone involvement and calcification in intra-orbital tumors. Further, the use of ionizing radiation in non-clinical setup is unethical, especially for orbital imaging, considering the high sensitivity of the eye lens to ionizing radiation and the potential cataract risk.[Lund and Halaburt 1982] Making it even more inappropriate, motion imaging needs a multitude of images to be able to adequately capture movements, further increasing the radiation dose. For motion imaging MRI is more commonly used, not least because of the possibility of encoding motion, speed (e.g. blood flow), and acceleration without exogenous agents. A further advantage of MRI in comparison to CT is the direct multiplanar facility and the better soft tissues (functional) contrast. The possibility that gave X-rays of seeing inside the body impacted on the development of MRI that was commercially available only a couple of years after CT.

1.1.3 Imaging of Macroscopic Motion with MR

The development from understanding the basic physics of MRI to clinically relevant images was the joint achievement of many. Since the 1920s basic physics researchers studied the interaction of radiofrequency waves with gas and solid mater.[Pauli 1924; Rabi, et al. 1938; Bloch 1946; Purcell, et al. 1946] To obtain images, as the wavelength is bigger than the objects, spectroscopic encoding of the image was developed and improved for faster image acquisition.[Carr 1952; Lauterbur 1973; Kumar, et al. 1975; Mansfield and Maudsley 1976] The possibility for clinical application was here, too, rapidly understood.[Damadian 1971; Mansfield and Maudsley 1977] The first image of a human thorax was obtained with an acquisition duration of 4 hours, only 3 decades ago.[Damadian, et al. 1977] Since this first images, the improvement of the imaging capabilities as been maintain at a sustained rhythm, see Table 1 in Blamire's review.[Blamire 2008]

1.1.3.1 Cine MR Imaging

In the eighties, imaging of cine anatomically resolved MRI begun with the beating heart, as it did for visual, photographic, and CT. The term "*cine*" imaging was used ab initio for imaging a dynamical process with several times frames.[Sechtem, et al. 1987a] The acquisition of multiphase images allowed for the determination of functional parameters such as the myocardial wall thickness, ventricular and atrial volumes, valvular function, and blood flow.[Smolorz, et al. 1988; Underwood 1989] The development of gradient echo sequences gave the possibility of acquiring many images in a reasonable time.[Frahm, et al. 1986; Haase, et al. 1986; Van Dijk, et al. 1986] Additionally, echo planar imaging (EPI)[Mansfield and Maudsley 1976] further reduce the scantime.[Worthington, et al. 1986a; Rzedzian and Pykett 1987] To avoid image blurring due to tissue movement, two possible acquisition strategies are possible: The first is to acquire real time images in a scantime as short as possible.[Worthington, et al. 1986a; Sechtem, et al. 1987b; Pan, et al. 2006] The other acquisition strategy is to gate the acquisition with the cardiac cycle, or more generally the periodic movement, and segment the acquisition of one time frame over several periods of the movement.[Fisher, et al. 1985]

1.1.3.2 Motion-Encoding with Tagging Methods: SPAMM, DENSE

Shortly thereafter, the limitations of such „anatomical“ imaging were recognized, especially for the quantification of tissue deformation. For example, the rotation of the myocardium during the contraction could not be reliably observed, nor the inhomogeneous deformations within tissues with a homogeneous MR signal. It has been known that the MR signal is sensitive to motion since the fifties.[Hahn 1950; Suryan 1951; Carr and Purcell 1954] So, new imaging sequences were sought after to reliably track the movement of a tissue.[Battocletti, et al. 1981] A possible technique consists in purposefully inducing an inhomogeneous MR signal, or, in other words, in modulating the tissue MR signal. The first trials of the development of a MR technology able to measure (blood) movement are - in principle - the electromagnetic equivalent of the sphygmograph of Marey, except that the flow and not the pressure wave was measured.[Bowman and Kudravcev 1959; Singer 1959; Morse and Singer 1970] Several reviews of these non-imaging methods are published.[Singer 1978; Axel 1984]

First applied to time-of-flight measurements of blood flow in healthy subjects,[Moran 1982; Singer and Crooks 1983; Bradley, et al. 1984; Bradley and Waluch 1985] the tagging (i.e. spatial modulation) of tissue magnetization was introduced in 1988 to depict the heart deformation within an image plane.[Zerhouni, et al. 1988] Further improved,[Axel and Dougherty 1989; Fischer, et al. 1993; Stuber, et al. 1999a; Ryf, et al. 2004a; Abd-Elmoniem, et al. 2005; Rutz 2008] this method - called spatial modulation of magnetization (SPAMM) - was adapted to other tissues, e.g., the tongue,[Niitsu, et al. 1992; Napadow, et al. 1999; Stone, et al. 2001] the lower leg muscles,[Niitsu, et al. 1992; Sinha, et al. 2004] the pelvis,[Niitsu, et al. 1992] and the brain.[Soellinger, et al. 2007] The deformation of this inhomogeneous signal pattern can then be followed on images acquired subsequently, which eases the quantification of the tissue motion or deformation,[Stuber, et al. 1998] and therefore makes biomechanical modeling more accurate.[Schmid, et al. 1995] With this methodology, tissue functionality may be determined.[Stuber, et al. 1999c; Paetsch, et al. 2005] For increasing the reliability of such deformation quantification, several acquisition parameters can be optimized depending on the application and organ investigated.

Hereunder, a brief overview of relevant parameters for the following applications is given. Further details can be found in the relative chapters. For line tagging, the magnetization is modulated in one direction, creating a line pattern on the image. The distance between these lines, the *tagline distance*, needs to be as small as possible to increase the sensitivity to motion.[Stuber, et al. 1999b] Nevertheless, a small tagline distance will impose the acquisition of a high resolution image - with associated SNR decrease, to be able to visualize the tagging pattern, and avoid an

SNR penalty due to intra-voxel dephasing. Formulated in the Fourier domain of the MR image, this will impose large and fast amplitude changes of the magnetic field gradients.

In dependence of the implementation of the tagline tracking, different tagging strategies were developed. For magnitude tracking algorithm, taglines with a sharp thin dark line are preferred. On the other hand, for phase tracking[Osman, et al. 1999] a sinusoidal modulation of the signal is preferred.[Axel and Dougherty 1989; McVeigh 1996; Ryf, et al. 2004b]

To avoid overriding the gradient capabilities, a variation of the tagging methodology, called displacement encoding with stimulated echoes (DENSE), has been introduced[Aletras, et al. 1999] and further improved.[Sampath, et al. 2003; Gilson, et al. 2004] DENSE, and similarly FastHARP,[Abd-Elmoniem, et al. 2007] consists in applying an additional gradient in the same direction as the magnetization modulation, to shift, in the Fourier space, one of the intensity peaks of the signal modulation in the middle of the Fourier space, i.e. to readout only one peak of the conjugate pair of harmonic peaks. This translation in the Fourier space corresponds to a phase demodulation of the MR signal, which causes the tagline pattern disappear. Nevertheless, under this condition the phase of the MR signal best encodes the displacement. Transverse magnetization is initially position encoded by an encoding gradient pulse, stored temporarily as longitudinal magnetization during the displacement duration and then refocused just prior to data acquisition by a gradient pulse. If a particle moved, the refocalization won't be complete and the residual phase would be proportional to the particle movement along the gradients' direction.

To further increase the sensitivity to the displacement of DENSE, a shorter modulation frequency of the MR signal can be chosen. In this case, the unwrapping of the phase may become necessary to avoid error in the tracking of the displacement. These methods are more suited for spiral imaging, but the acquisition of two datasets are needed to use peak-combination.[Ryf, et al. 2004b] This method was first developed for cardiac imaging, but is also applicable to skeletal muscles.[Zhong, et al. 2008] Being a stimulated echo sequence, DENSE has also the related limitations, such as signal loss.[Fischer, et al. 1995]

In addition to the frequency of the MR signal modulation and the image resolution, the flip angle used for the different time frames is relevant for the T1 fading of the tagline. If ramped appropriately, the contrast of the tagline can decrease, remain constant, or even increase over time.[Fischer, et al. 1993] Also presented by Fischer, et al., the acquisition and subtraction of complementary tagging data, with first a positive and then a negative tagging grid to separate the magnetization component with the tagging information from the relaxed component, was used.[Fischer, et al. 1993] This technique is also applicable to DENSE data.[Gilson, et al. 2004] This method, combined with a slice-following technique where the imaged slice follows the tissue slice, allows for a more reliable tracking of the cardiac tissue in case of through-plane motion.[Fischer, et al. 1994; Stuber, et al. 1999a] For further information about tagging, a good introduction is given in these two PhD thesis: [Kuijer 2000; Rutz 2008].

1.1.3.3 Velocity-Encoding using the Phase of the MR Signal

Tagging encodes the position of a piece of tissue at the beginning of the movement and then acquires the modulated image several times. The limitations of tagging appear when the investigated movements have a complex geometrical structure and whirl displacements induce signal void, or when the displacement between two time frames is bigger than one half the tagline distance.

A method to avoid such problems is to encode the displacement of each time frame separately. Due to the relatively long T1 (> second) - compared to the period of interesting movements (< second) - such encoding cannot be effectuated over the magnitude of the MR signal (due to the crosstalk of subsequent measurements). However, the phase of the MR signal varies and can be modulated must faster, but is still able to maintain coherent information for several tens of milliseconds, on the order of T2. This makes the phase appropriate for such encoding. Another advantage of the phase encoding compared to the image magnitude is the (lesser) dependence of

the underlying tissue properties like T1, T2, and the proton density. These rationales motivated the development of "instantaneous" displacement encoding i.e. flow encoding based on the phase of the MR signal.

The phase encoding of displacement was developed and improved concurrently with signal magnitude encoding.[Bryant, et al. 1984; van Dijk 1984; Feinberg, et al. 1985; Cho, et al. 1986; Katz, et al. 1987] Pioneer work aiming an application to the measurement of ocean flows set the theoretical framework for the phase encoding of the displacement in the direction of a magnetic field gradient.[Hahn 1960] Velocity distribution of fluid flow[Garroway 1974] and of in vivo blood flow[Grover and Singer 1971] can be obtained by Fourier transforming the phase-encoded signals. Bipolar gradients phase encode the velocity component along the magnetic field gradient.[Moran 1982; Redpath, et al. 1984] Strong magnetic gradients are needed to avoid image degradation through T2 decay effects.[Redpath, et al. 1984] Separate measurements of all three vector components of the flow velocity within a gradient echo sequence is possible.[Meier, et al. 1988] Fractional-echo acquisition, like the FAcE technique, reduces the minimal echo time and therefore minimizes background phase noise.[Scheidegger, et al. 1991; Boesiger, et al. 1992; Maier, et al. 1996] Much has been achieved since the in vitro measurements of Leonardo da Vinci, and the in vitro measurements can now be compared to in vivo data.[Moore, et al. 1994] More recently, real-time blood flow measurement were obtained.[Oelhafen, et al. 2006] A detailed review is given in [Axel 1984], and a detailed introduction about phase encoding of tissue displacement can be found in [Bernstein, et al. 2004].

Since the displacement is encoded for each timeframe over a constant duration, it is clearer to report the obtain information as momentary speed or flow map. If phase wrapping and the following unwrapping needs to be avoided, than the dynamic range of the velocity encoding is limited to 360°. The maximal speed (in one direction) corresponds to a phase shift of 180°. A speed in the opposite direction induces a negative phase shift. In the case of a not too fast maximal speed, the speed encoding gradients have to be increased to enable the use of the whole dynamic range of the phase encoding. Strong and rapidly changing magnetic field gradients are disturbed by eddy currents that disrupt the phase encoding accuracy.[Kozerke, et al. 2001]

1.1.3.4 Strain-Encoding

Tissue displacement is important for the characterization of a biomechanical system, but also other (more synthetic) parameters are important. Especially for muscles, tissue deformation (elongation or contraction) is relevant for a functional description. The strain is defined as the length difference between two time frames relative to the length at the reference time frame. As a length is always positive, the strain is included in $]-1;\infty[$ and is zero for no length change. For averaging strains, this asymmetry needs to be accounted for by averaging the logarithm values of the relative lengths (=strain+1). To avoid noise amplification due to the length subtractions, a method to directly obtain strain maps, called SENC, has also been proposed.[Osman, et al. 2001] For this two dimensional (2D) method, the tagging preparation is applied in through slice direction and two data sets with different demodulation frequencies are acquired. Over the intra-voxel signal dephasing an intensity image proportional to the through-slice strain is obtained. The major drawbacks of this method are the impracticability of a 3D acquisition scheme as knowledge about the excitation slice profile is needed for strain calculation, and the impossibility to track tissue point motion.

1.1.3.5 Reducing Acquisition Time

A recurrent issue for all types of dynamic acquisition is the need to shorten the acquisition time. The acquisition of several time frames of a motion is particularly long, as a lot of data needs to be acquired. A further reason to decrease the image acquisition time is to increase the time

resolution, i.e. to increase the number of time frames and to diminish their duration. For this, several methods could be used. Gradient echo sequences with EPI readout have already been mentioned. Additionally, to be able to increase the EPI train length - despite a short T2* - several gradient echo shots can be acquired for each time frame. Nevertheless, unlike turbo spin echo, for turbo field echo an excitation pulse - to bring the magnetization into the xy plane - is needed for each shot. A further drawback is the reduced temporal resolution due to longer time frames.[Ryf, et al. 2005]

In the case of the acquisition with a coil array, parallel imaging [Pruessmann, et al. 1999; Pruessmann, et al. 2001a; Weiger, et al. 2002] decreases the scantime, as has been shown for cine cardiac imaging.[Weiger, et al. 2000; Pruessmann, et al. 2001b] More specifically dedicated to decrease the acquisition time of cine images, k-t BLAST uses the similarity between time frames to optimize the data acquisition in Fourier space.[Tsao, et al. 2003] This method was applied to cardiac cine imaging, too.[Kozerke, et al. 2004] For sufficiently sparse data[Gamper, et al. 2008] or data sufficiently sparse after projection on some temporal basis functions[Pedersen, et al. 2009] compressive sampling methods can be used. Further refinements on the same principles have been proposed.[Tsao, et al. 2006; Vitanis, et al. 2009] These methods were used to accelerate cine cardiac imaging[Weber, et al. 1999; Tsao, et al. 2005; Jahnke, et al. 2007; Greil, et al. 2008] and phase-contrast flow measurements.[Hansen, et al. 2004; Baltes, et al. 2005; Hansen, et al. 2006; Baltes, et al. 2008]

The quality of 3D tagging images suffers from its long scan duration.[Ryf, et al. 2002] Specially tailored for tagging acquisition, several methods for faster scanning have recently been proposed.[Ryf, et al. 2005; Rutz, et al. 2008] Through a reduced field of view (FOV), the number of lines acquired in Fourier space diminishes.[Hu and Parrish 1994] The use of line tagging, instead of grid tagging, allows the concentration of the signal power in a smaller region of the Fourier space, reducing the needed Fourier space coverage. These allowed the acquisition of 3D tagging cardiac data, in only 3 heartbeats.[Rutz, et al. 2008]

1.1.4 The Diagnostic Value of Abnormal Eye Movements

Of the numerous orbital pathologies,[Müller-Forell and Pitz 2004] those affecting eye movements are here of interest. The different types of eye movements are saccades, vestibulo-ocular reflex, smooth pursuit, optokinetic nystagmus, vergence, and gaze holding eye movements. [Oyster 1999a] For an overview of the neuronal control of the different movement types see [Straube and Büttner 2007] and [Leigh and Zee 2006]. The correct motor function of both eyes is necessary for a good quality of vision, high quality of life,[van de Graaf, et al. 2009] and the ability to obtain employment.[Coats, et al. 2000b] Ocular misalignment affects nearly 3% of the world population.[Webber and Wood 2005] Eye movement impairments may have a multitude of causes, ranging from tumors, metabolic, inflammatory, vascular, neuronal, muscular, or traumatic diseases; and can involve one or several neurological structures or orbital compartments like the sinus and bone, the globe, the extraconal masses, the EOMs and the intermuscular connective tissues, the intraconal masses (fatty tissues, vessels and nerves), or the optic nerve (ON).[Goh, et al. 2008]

The impact of each eye movement pathology on the orbital biomechanical and control systems needs to be understood, as this insight is important to avoid or to correct eye gaze misalignments arising from it. This is true even in the case of foreign bodies impairing correct eye movements. These foreign bodies can be big enough to be visible on radiographic images, or, in the case of subtle facial bone ruptures, so small that their presence or effect can only be asserted during eye movements. In this case, MR imaging of the orbit during eye movement is needed to understand how the foreign bodies disturb eye movements. This is also true for orbital oncologic, inflammatory, metabolic, or vascular pathologies that are at the origin of an eye movement disorder.

Clearly, the most relevant pathologies are the ones directly affecting the neuronal control or the biomechanical plant of the eye, such as Duane's syndrome, where a cranial nerve innervation of the EOMs is missing or aberrant. The most common disorders affecting the EOMs are: Grave's disease or thyroid ophthalmopathy – an autoimmune disorder associated with excess thyroid gland secretion, orbital myositis, and orbital pseudotumor - inflammatory diseases. Grave's disease can also affect the orbital fat. For diseases that affect the oculomotor system at the orbital level, surgery can be appropriated. To avoid reoperation or improve the results of surgery, a better understanding of the effect of pathologies and of their therapies on eye movements is necessary. In the last two decades, there has been a shift in the oculomotor understanding from a rudimentary orbital biomechanics with a complex neurological control to a more elaborated biomechanical implementation of the eye movement characteristics, which simplifies the neuronal commands.[Demer 2007] This gives hope of a possible surgical treatment of diseases that were wrongly supposed to have a neurological origin, for example in myopia strabismus fixus,[Wong, et al. 2005] or pulley instability.[Oh, et al. 2002] Therefore, a better understanding of the orbital biomechanics in clinical practice is needed, to make surgery safer and more effective.[Miller and Robins 1987; Clark and Demer 2002; Clark, et al. 2004]

An example of this ongoing shift of attention is the conceptualization of a biomechanical implementation of Listing's Law, reducing the complexity of the neuronal control by reducing the controller's degrees of freedom.[Tweed and Vilis 1990; Wong, et al. 2002; Quaia and Optican 2003] Further, the unclear role of the orbital connective tissues[van den Bedem, et al. 2005; Demer 2007] shows that new data of the orbital conformations during eye movement are needed to put light onto the dynamical processes of the orbital biomechanics.

Information about the dynamical properties of the orbit are important for its biomechanical modeling, as the eyes are constantly moving, and pathologies may be disturbing if they impair movements, even if the temporary static conditions are not perturbed. As an early marker for pathologies, orbital biomechanics may adapt before serious ocular motion impairments are noticeable by the ophthalmologist. This is also relevant for pediatric orbital diseases.[Davis and Hopkins 1999; Gorospe, et al. 2003]

Investigations of the oculomotor system contributed significantly to the understanding of the sensory-to-motor transformation, sensorimotor processing, and motor control in general. The models created for each eye movement type comprise a map of (partially) specific and different cortical and subcortical areas.[Leigh and Zee 2006]

1.1.5 Obtaining Knowledge about the Oculomotor System

In the cases of foreign bodies, tumor or vascular problems impairing eye movements, conventional medical imaging techniques are in most cases sufficient to plan surgical interventions. For MRI, this includes axial and coronal fat saturated T2 weighted TSE scans, axial T1 weighted TSE images, and contrast-enhanced axial and coronal fat saturated T1 weighted TSE scans. In some cases, T2W TSE images without fat saturation, MR dacryocystography, diffusion weighted imaging (DWI), and diffusion tensor imaging (DTI) for the ON are added.[Conneely, et al. 2008]

The first papers on the diagnose of orbital pathologies with MRI report T1 and T2 maps, T1 and inversion recovery weighted images[Moseley, et al. 1983] and flow-dependent spin sequences to diagnose pathological vessels.[Hawkes, et al. 1983] Nevertheless, the long scan duration needed to achieve a useful resolution with the spin echo technique was long enough to cause globe movements artifacts.[Worthington, et al. 1986b] The use of surface coils (array) improves the image SNR.[Bilaniuk, et al. 1985; Schenck, et al. 1985; Zimmerman, et al. 1985; Breslau, et al. 1995] In the first studies, the goals were pathological perfusion and tumor type differentiation.[Li, et al. 1984; Sobel, et al. 1984; Char, et al. 1985; Edwards, et al. 1985; Sobel, et al. 1985] Vitreous liquefaction was also studied.[Gonzalez, et al. 1984; Aguayo, et al. 1985] Reviews of conventional (MR) orbit imaging have been recently published.[Conneely, et al. 2008; Goh, et al.

2008] For diseases of the EOMs, connective tissues, or neuronal systems, a more detailed examination and more advanced imaging techniques are required.

To study the central neuronal components of the system, (functional) MRI,[Sweeney, et al. 2007] PET,[Petit, et al. 1993] electroencephalography,[Jagla, et al. 2007] and electrocorticography[Johnson, et al. 1999] can be used. Peripheral neuronal components can be investigated by electromyography,[Breinin 1957; Huber 1962; Pattichis, et al. 1999] and electroneurography.[Barboi and Barkhaus 2004] The cranial nerves - linking the two components - can be imaged by MRI.[Demer, et al. 2006] Finally, the effect of these neuronal components is revealed by the eye movements itself.[Robinson 1975]

Nevertheless, the knowledge obtained by these methods fails to determine the etiology of ocular misalignment in some cases. The anatomy and function of the oculomotor system is also relevant.[Horton, et al. 1990] After the discovery of curved EOM paths by Simonsz et al.[Simonsz, et al. 1985], the EOM paths were studied in details with MRI.[Worthington, et al. 1986b; Miller and Robins 1987]Using gradient echo sequences, the imaging at different gaze directions has given insight into the EOMs conformation and the role of connective tissues in determining EOM location.[Demer, et al. 2002] This new insight has also challenged the existing understanding of the orbital mechanics,[Demer 2001] and, by extension, existing oculomotor models.[Demer 2002] Nevertheless, these static data were not sufficient to give a clear understanding of orbital tissue function, so that histological data including 3D cuts were necessary.[Demer 2002]

These studies mostly used coronal MR images. One should be aware that motion of EOMs through space-fixed coronal planes can result in an apparent thickening of EOM segments simply due to the angulation of the EOMs through the image plane.

Up to this work, static or low resolution anatomical dynamic MRI were used to explain misalignment etiologies, by giving insight into the structure or mechanics of components of the orbit. Abramoff postprocessed a series of static images to gain insight into the deformation of orbital tissue as a function of gaze direction.[Abramoff, et al. 2000] In the attempt to gain insight into orbital dynamic processes, movies of static images and tissues borders as markers of the deformation were used.[Abramoff, et al. 2000; Botha, et al. 2005] Abramoff motivated his work as follow:

> *"The introduction and refinement of noninvasive imaging techniques such as computed tomographic scans and magnetic resonance imaging have been revolutionary in the differentiation of orbital diseases. However, these techniques are static and in a number of cases leave unanswered questions about the origin of lesions and the relationship between tissues during motion. This relationship, the kinetics of the eye and orbital tissue due to gaze, is highly complex and incompletely understood.[Gentry 1998] Cinematic* [i.e. multiple static positions] *MRI, and also dynamic CT and dynamic ultrasound, were developed to surmount these limitations and to evaluate the motion of tissues in the orbit in relation to gaze changes.[Bailey, et al. 1993; Demer and Miller 1995] However, cinematic MRI scans and the other two modalities are evaluated by inspection of videos and consequently allow only qualitative judgments that are subject to a large intra- and interobserver variability. By measuring motion quantitatively, this may be avoided. In addition, data reduction can be achieved. [...] We have developed a new technique, MRI-dynamic color mapping to quantitatively measure the motion of orbital tissues, using cinematic MRI with short acquisition times (5 seconds/image), combined with powerful image-processing techniques.[Amartur and Vesselle 1993; Bailey, et al. 1993; Demer and Miller 1995] The purpose is to express the motion of orbital soft tissues in millimeters per degree of change in gaze and display these in a color-coded image [...]. This technique allows the study of motion in relation to gaze changes, but not yet of saccades and pursuit movements, because the temporal resolution of orbital cinematic MRI currently does not allow it."[Abramoff, et al. 2000]*

Tracking tissue borders means to discard a lot of the imaged information, and to be sensitive to image noise and artifacts (as high resolution images are needed). Such a method is not valid for describing contractility within tissues, since heterogeneous deformation inside homogeneously contrasted tissues cannot be determined due to the absence of landmarks for the deformation recognition. Recognizing the necessity of such landmarks, Miller et al. implanted gold beads inside monkey orbits, that served to successfully demonstrate orbital soft tissue deformation in static CT acquisitions.[Miller, et al. 2006] However, static images were used, so no input into dynamical processes could be expected.

To investigate orbital and muscular tissues during eye movement, invasive EOMs' force measurements[Miller, et al. 2002] were performed, but are difficult to obtained in patients.[Collins, et al. 1975]

Non-invasive eye movement recordings (for an overview see [Eggert 2007]) do not show what happens inside the orbit or at the muscular level. For example, to understand Listing's Law at a motor level, MR images of the orbit were needed to show the extorted EOMs pulleys.[Demer, et al. 2003]

1.2 A Missing Piece of Understanding in the Eye Movement Control Chain

A missing piece of understanding in the eye movement control chain is the mechanism underlying the transformation of the neuronal command into the actual eye movement.[Glasauer 2007] Models of the eye plant describe the transformation of the neuronal signal of the motor nuclei located in the brainstem into the eye movements. These models can be static or dynamic. The dynamic models allow the determination of the time constants of the modeled eye plant. The lack of dynamic data of the orbit added to the complexity of the described processes - numerous time constants[Sklavos, et al. 2005], geometry dependent force of the EOMs - inhibited the implementation of a more adequate eye plant models, and to fully understand the neuronal and biomechanical elements of the eye movement plant.

Simple quasi agonist-antagonist models of the EOMs are not sufficient to perform efficient surgery in complex strabismus cases, e.g. for patient where the superior oblique muscle is atrophied, since the inferior oblique muscle (IOM) size and contractibility do not correlate with clinical motility.[Kono and Demer 2003] In case of deformation of the orbital bone due to craniosynostosis,[Lajeunie, et al. 1999] too, an increased knowledge about orbital biomechanics seams necessary considering the poor response to surgery.[Coats, et al. 2000a] Also in other eye movement diseases, a postoperative drift of the eye gaze correction is observed. A better understanding of the oculomotor system makes orbital surgery safer and more effective.[Clark, et al. 2004]

No appropriate dynamic data of the orbital tissue deformation are available, even if dynamic equilibrium exists, like the dynamic violation of the Listing's Law during saccades in superior oblique muscle (SOM) palsy.[Wong, et al. 2002] The controversy concerning the active or passive role of the orbital connective tissues[van den Bedem, et al. 2005; Demer 2007] shows that new data are still needed to elucidated the orbital biomechanics.

Data of orbital tissue deformation during eye movement would help to give insight into the transformation of the neuronal signal into mechanical action. Such data should have a high spatial and temporal resolution to resolve different tissue kinetics. High precision is required to compare the accuracy of orbital biomechanics and oculomotor neuronal control models, and to determine tissue properties.

Moreover, data are needed that give the possibility to differentiate etiologies of diseases, and therefore impact on surgery planning, by determining which segments of the EOMs are functional and which are not. This may give insight into the pathophysiological processes of loss and regain of muscular function due to metabolic or neuronal diseases. Helpful would be to see the

differential contraction dynamic along the EOMs to reveal - maybe with the use of physiologic or pathologic models - the functional importance of the different muscle layers, muscle fibers (SIF and MIF), and proprioreceptors (in particular of the palisade on the myotendinious junction). The muscle layers may have different contraction patterns as the orbital layer might mostly oppose elastic forces, whereas the global layer might oppose principally viscose forces.[Büttner-Ennever 2007]

For obtaining high resolution data, without motion blurring, a segmented MR acquisition will be needed with the actual scanner technical limitations. For this, repetitive eye movements during the MR image acquisition will be necessary. Further, the eye movements will have to be synchronized with the MR acquisition. To the best of the author's knowledge, these issues have not yet been solved or, at least, such methods have not been reported.

1.3 Objectives

The goal sought by performing dynamical imaging of the orbit is to give new observables for models of the orbital mechanics and eye movement control, to provide data for computational models of the orbit, thus improving the insight on the orbital mechanics and to further test hypotheses about ocular rotation and the origins of eye misalignment. To test the feasibility of this approach, a proof of principle should be made by differentiating pathological tissues (e.g. of patient suffering from Duane's syndrome) from healthy ones, and obtaining biomechanically relevant parameters of orbital tissues, e.g. the vitreous and the EOMs.

To make dynamical imaging possible, the objectives of this work are therefore to obtain repetitive eye movements inside the scanner and to perform a segmented acquisition, i.e. to acquire a piece of the image at each repetition of the periodic movement in order to combine them into a single MR image. Dynamic imaging being - especially in the phase encoding direction - prone to motion artifact, methods should be proposed to diminish such artifacts. However, even for dynamic high resolution anatomical images of the orbit during eye movements, a scantime acceptable for a patient should not be exceeded. A further objective is the measurement of the (presumed) inhomogeneous contraction along the EOMs and the ability to differentiate normal from pathologic EOMs deformation, during eye movement.

To increase the relevance of the acquired data and to optimally use the limited scantime, motion and velocity encoded images of the orbit were obtained. To extract the adequate quantitative information out of theses dynamic MR images, appropriated postprocessing tools for the tracking and quantification of the orbital tissues deformation, with minimum user interaction, were developed.

1.4 Outlines

To measure the precision and accuracy of eye movements, scleral search coils experiments are performed with different direction and acceleration patterns of the gaze target. Scleral search coil setups are the gold standard for measuring eye movements along their three degrees of freedom (horizontal, vertical and torsional).

For high resolution anatomical imaging, the image contrast is optimized on an animal model and on healthy human subjects. The first high resolution images of the orbit during eye movement are reported. For the acceleration of the image acquisition several MR methods are evaluated, like EPI and kt-BLAST.

Several displacement encoding techniques (Q-Flow, CDENSE, and CSPAMM) are used to obtain the first motion and velocity encoded images of the orbit during eye movement. These methods are compared and evaluated for their suitability to fulfill the above mentioned objectives.

Image noise resistant postprocessing tools to extract quantitative information from motion encoded data will be presented. These postprocessing tools are model free to avoid a priori conceptions to interfere with the discovery of this new data.

This new imaging and postprocessing technique will be used in a proof of principle study to show that the EOMs deformation pattern of healthy subjects can be obtained and differentiated from the pattern obtained from Duane's syndrome patients.

Finally, parameters relevant for the modeling of the orbit biomechanics will be quantified from our data. The vitreous viscosity and elasticity will be determined by fitting to the vitreous deformation a commonly used viscoelastic model. Through this, it is shown that the obtained data are suitable for model testing and increase the understanding of the orbital biomechanics.

Chapter 2: Methodology for the Acquisition of MR Images of the Orbit during Eye Movement

Some of the work presented in this Chapter is part of the SNF Grant # 3100A0-102197 Annual Reports.

2.1 Visual Stimulus Determination

With the actual limitations of the available scanner systems, segmented acquisition of the MR data is necessary to reach high spatial and temporal resolution. To obtain this high resolution, the eye movements have to be repetitive and synchronized with the MR acquisition. A visual target to gaze at helps the induction of such eye movements. To determine the target motion inducing the most precise and accurate eye movements, scleral search coils experiments measuring the eye displacement over its three degrees of freedom were performed.

The eye movements were measured for target moving circularly, vertically, and horizontally. Constant speed, constant acceleration, or sinusoidal target displacement were confronted. Different (maximal) target velocities were compared: the peak velocity ranged from 20 to 95°/sec. The amplitude was constant and corresponded to ±20°, similar to the maximal gaze angle obtainable inside the scanner. Different target presentation setups were also compared: a red laser dots on a white wall in a dark room and a white square projected on a screen with a digital projector in a dark room.

The results are that not too fast sinusoidal eye movements, with a maximal rotational speed of 62°/s, gave the eye movement with the highest reproducibility, i.e. the lowest standard deviation (StdDev), for a duration of the paradigm of even 10 minutes (see Figure 2.1).

Smooth pursuit eye movements gave more accurate eye movements than saccades, as the amplitude of the saccades was quite variable. For a velocity of 60°/s and amplitude of ±20° the StdDev was of 3.3° (see Figure 2.2).

Leftward and rightward eye movements have similar StdDevs. Nevertheless, horizontal eye movements were more accurate than vertical eye movements (see Figure 2.3).

2.1.1 Stimulus Paradigm and MRI Setup

A horizontal sinusoidally oscillating white square (target size = 0.4°, luminance = 5.1 ± 1 cd/mm^2 on a background of 0.05±0.02 cd/mm^2) with an amplitude of ±20° and a period of 2 s (corresponding to a maximal target velocity of 64°/s) was presented on a black background to induce smooth pursuit eye movements.[Meyer, et al. 1985] Preliminary experiments using scleral search coils confirmed that a maximal target speed of 64°/s induced only few catch-up saccades, see also Figure 3 in [Yee, et al. 1983]. During preparation, all subjects confirmed the target was visible at all times.

Dynamic images of the right orbit were acquired using a small receive-only surface coil (47 mm diameter) on a 1.5 T system (Achieva 1.5 T; Philips Medical Systems, Best, The Netherlands).

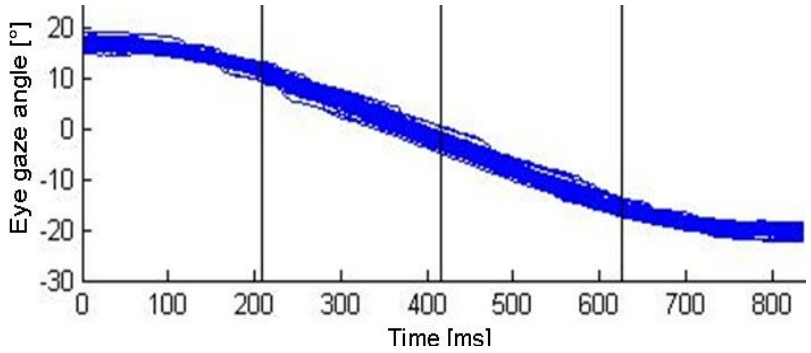

Figure 2.1: Superposition of horizontal eye gaze angle in function of time for leftward eye movements. A sinusoidally moving target (white square on a black background) with a maximal speed of 74°/s was presented during 10 minutes. For each half period of the target movement the eye movements recorded with a scleral search coil are overlaid. Their StdDev was around 1.0°.

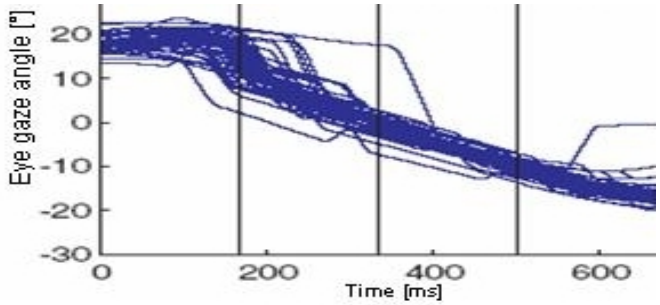

Figure 2.2: Superposition of horizontal eye gaze angle in function of time for leftward eye movements. A moving target (red laser point on a white background) with a constant speed of 60°/s was presented during 10 minutes. For each half period of the movement the eye movement recorded with a scleral search coil are overlaid. Their StdDev was around 3.3°. Saccades can be seen at the change of target moving direction, followed by smooth pursuit eye movement.

Small surface coils have a greater SNR that declines faster with depth than larger coils. Preliminary experiments showed, however, that the microscopy coil used still had a better SNR for the orbit, i.e. for a distance from the coil ranging from 1 cm to 6-8 cm, than the next bigger surface coil at disposal. The microscopy coil was placed like a monocle, so that it was possible to see the target through it. The head of the subject was immobilized with foam pads. A typical functional MRI setup (computer projector, screen, and the software "Presentation"—Neurobehavioral Systems Inc., Albany CA, USA) was used for the presentation of the visual stimulus. A mirror allowed the subjects to gaze out of the bore to the projection screen. The horizontal gaze range was 40°. The room light was turned off to maximize the contrast of the stimulus. The sinusoidal oscillation of the target was repeated during the whole MRI acquisition.

2.2 Anatomical Image Acquisition during Eye Movement

To acquire high spatial and temporal resolution images of the orbit during eye movements in a reasonable time, the MR acquisition sequence has to be accelerated - see section 2.2.2. But even before this, the contrast of the EOMs relative to the orbital fat and connective tissues has to be optimized, as described in the next section.

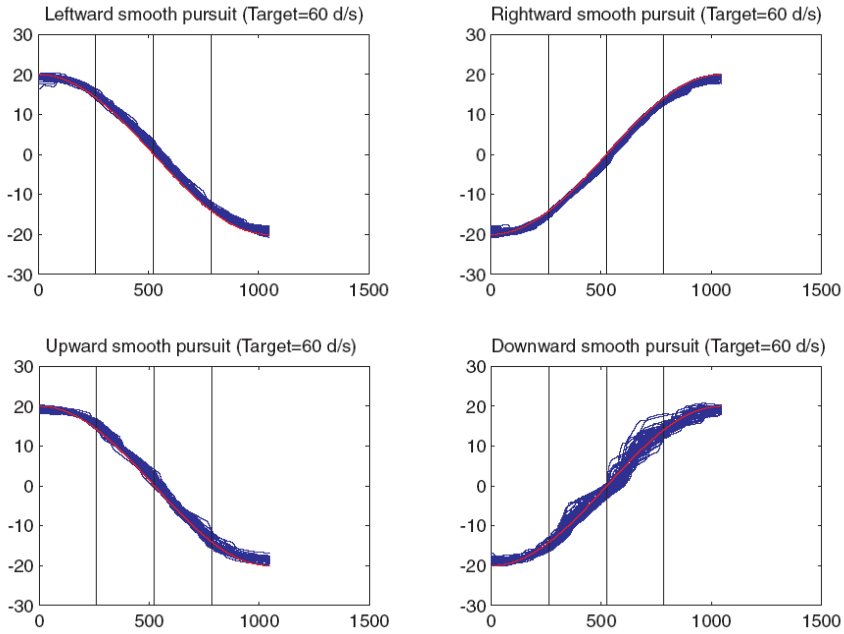

Figure 2.3: Superposition of eye gaze angle in function of time for horizontal and vertical, leftward and rightward eye movements. A sinusoidally moving target (white square on a black background) with a maximal speed of 60°/s was presented during twice 10 minutes once for horizontal and once for vertical movements. For each half period of the movement the eye movement recorded with a scleral search coil are overlaid. For the horizontal sinusoidal pursuit, the position StdDev was around 0.6° and the velocity StdDev around 12.3°. For the vertical sinusoidal pursuit, the position StdDev was around 1.1° and the velocity StdDev around 42.5°/s.

2.2.1 Contrast Optimization

To optimize the image contrast in aiming the possible segmentation of the EOMs from the orbital fat, a pig-head model as well as in vivo human's data were used.

After confronting several sequence types: spin echo versus gradient echo (T1, T2, or balanced), the T1-weighted gradient echo sequence was selected and most of the imaging parameters of this sequence were tested for their effect on the contrast, including: the echo time, the repetition time, the resolution, the scan time, the slice orientation, the number of signal average, the size of the FOV, the flip angle., the turbo field echo factor, and the number of time frames. Further, the use of water selective excitation, fat saturation techniques as spectral presaturation inversion recovery were compared. Finally, the signal homogenizing tool constant level appearance (CLEAR) was taken into consideration as the coil used had an inhomogeneous spatial sensitivity to the MR signal. For CLEAR a short reference scan preceding the dynamic scan is needed.

The best compromise was obtained for an eye movement period of 2 s with a T1 weighted TFE sequence with a TE of 11.3 ms and the shortest TR. Some parameters are listed here:

FOV (ap,rl,fh):	100 x 100 x 21 mm^3
resolution:	0.4 x 0.4 x 1.4 mm^3.
scan matrix:	256 x 205 x 15
scan percentage:	80%
time frames:	18
flip angle:	20°

TR:	22.5 ms
TE:	11.3 ms
Water Fat shift:	2.9 pixels
TFE factor:	3
EPI factor:	1
NSA:	1
Scan Duration:	1613 s = 27 min

WSE being faster, it was preferred to SPIR

For each time frame, the middle slice of the 3D dataset is reported in Figure 2.4. Even on the slice containing the tissues moving at the highest velocity, no motion artifacts are visible within the orbit. At the scleral insertion of the ON, the hyper and hypo contrasted tissues are still sharply pictured, even at the high image resolution used. Figure 2.5 shows all the slices of the 3D dataset acquired during the fastest phase of the eye movement. All slices are free of motion artifacts.

2.2.2 Acceleration of the Image Acquisition

With a TFE factor of 3, the acquisition of 18 times frames lasts 27 minutes. This, for a patient, obviously to long scantime, was further reduced by using k-t BLAST. The higher the k-t BLAST acceleration factor is, the shorter the acquisition time will be, but at the cost of stronger artifacts and lower SNR.

The full dataset - obtained without k-t BLAST - of the dynamic acquisition of Figure 2.4 and Figure 2.5 was used to investigate the effect of k-t BLAST on the image quality. This was done by decimating the data, which correspond to an increase of the k-t BLAST acceleration factor. Nota Bene, for k-t Blast to unfold the sparsely sampled data, low resolution data with the full temporal resolution are still needed, resulting in a lower scan time shortening. With 11 training profiles and for a k-t BLAST acceleration factor up to 3, almost no blurring could be observed for the EOMs, nevertheless, the scantime was reduced from 19min to 9.5min (see Figure 2.6).

With the same setup, dynamic 3D TFE images with a k-t BLAST acceleration factor 3 are acquired in only about 10 minutes. These images were nearly as good as static images. However, for the time frames with the fastest eye movement (with nearly 0° of gaze deviation, when the eye looked straight ahead), the fast moving tissues (e.g. the eye lens and the ON) are slightly blurred. Nevertheless, the effect of this blurring on getting observables meaningful for the clinical characterization of the EOMs or model testing, is to be investigated (see Figure 2.7).

The scan time reduction may also increase the reproducibility of the eye movements, as the fatigue of the subject will be smaller. Therefore the image quality may also be increased, despite the SNR drop due to the sparse sampling. To test the diminution of the artifacts resulting from the imperfect eye movements, with increasing kt-BLAST acceleration factor, dynamic images of the orbit during eye movements were acquired using different k-t BLAST acceleration factors, of 3, 6, and 9 (see Figure 2.8).

Since its publication in 2003 k-t BLAST has given rise to a multitude of sparse-sampling methods. It would be interesting to test some of these methods for the acceleration of the acquisition of dynamic images of the orbit.

A limitation of dynamic T1-weighted images is that it can only show the geometric deformation of tissue borders when these borders separate tissues with different chemical properties. However, T1-weighted MRI does not resolve the inhomogeneous deformation within a specific homogenous tissue in the orbit, e.g. the location of muscle contraction within the muscle, the displacement of the orbital fat, or the shift of the vitreous humor during eye movement. Therefore, more sophisticated MRI methods have been developed and will be presented in the next sections.

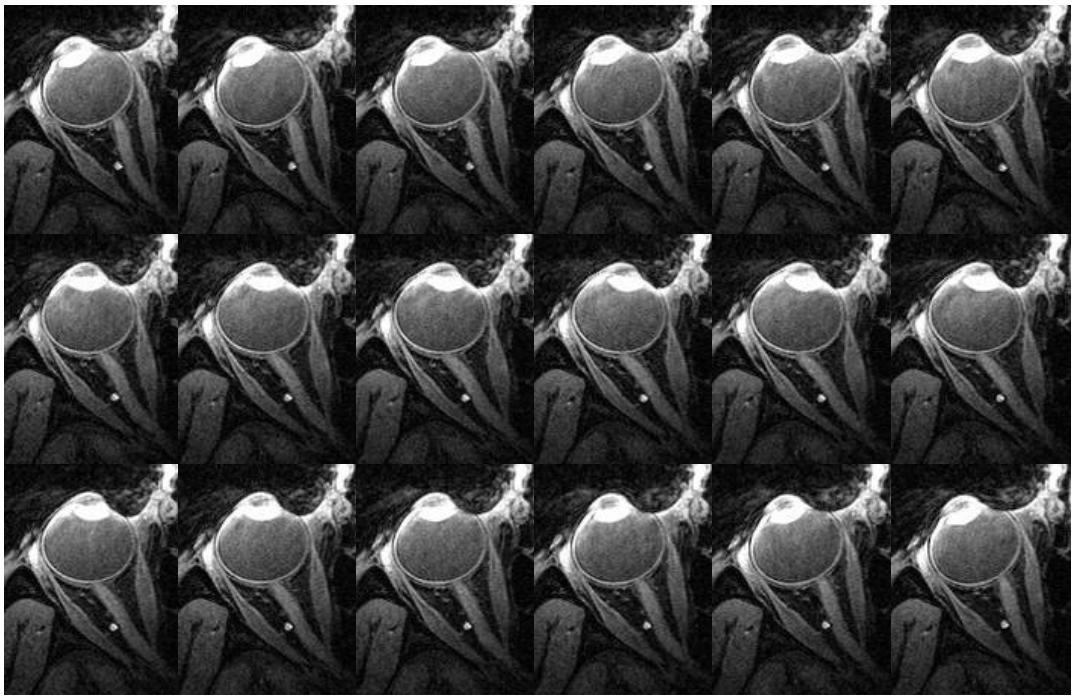

Figure 2.4: Middle slice of a high resolution T1-weighted TFE 3D dataset. The 18 time frames of the sinusoidal eye movements with a period of 2 s are represented here. The synchronization by the triggered gaze target of the eye movements with the MR acquisition enable a segmented acquisition and a quasi vanishing of the motion artifacts. The detailed scan parameters are given in the text.

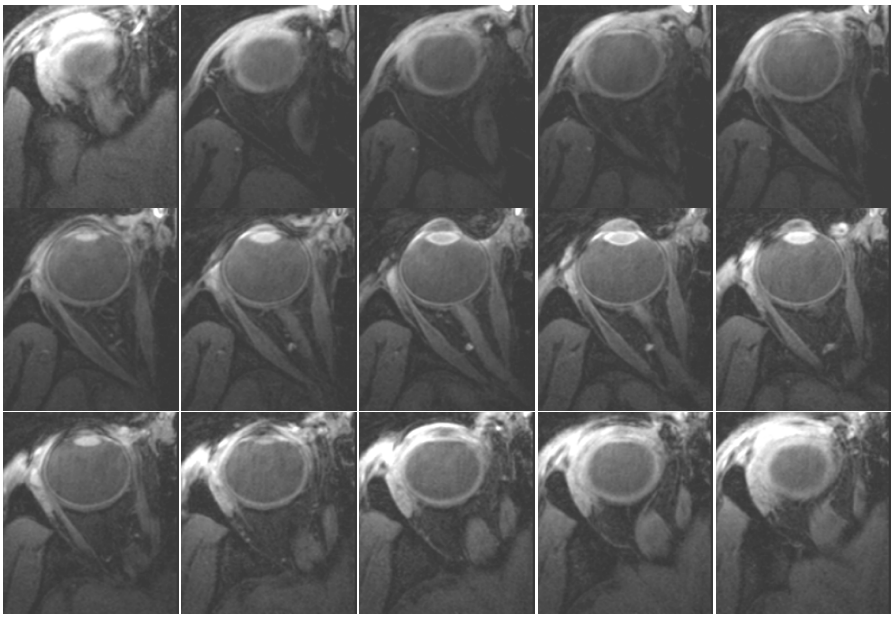

Figure 2.5: Same 3D dataset as the preceding Figure. Here, the 15 slices at the time frame with the fastest eye movement of 64°/s is depicted. All slices are free of motion artifacts.

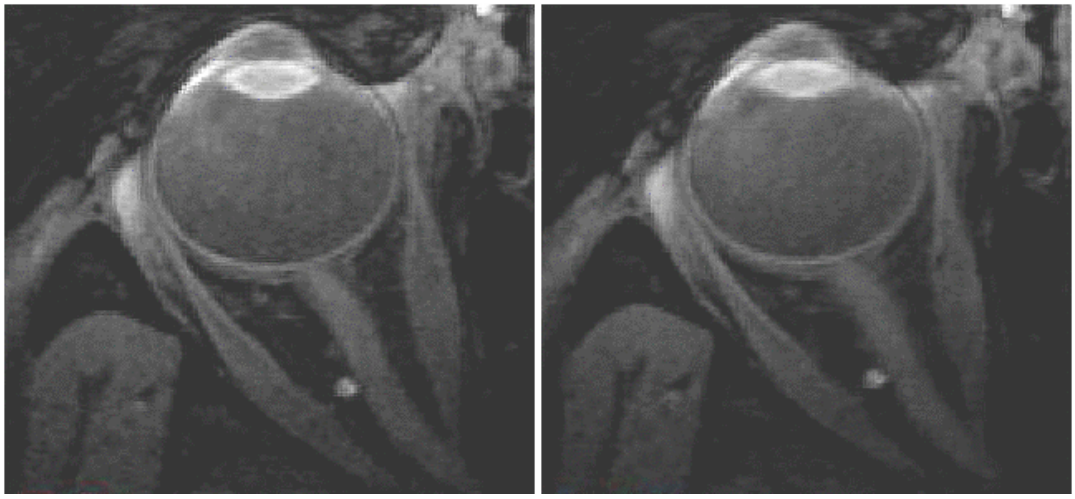

Figure 2.6: (left): slice with the greatest diameter of the globe of a 3D dynamic measurement without k-t BLAST, with 18 time frames, and a scan time of 27 min. (right): same slice of the same 3D dynamic measurement but reconstructed with a k-t BLAST acceleration factor of 3 and 11 training profiles, simulating a scan time of 9.5 minutes. The fast moving tissues (e.g. the eye lens and the ON) are blurred. Nevertheless, the effect of this blurring on getting observables meaningful for the clinical characterization of the EOMs or model testing, is to be investigated.

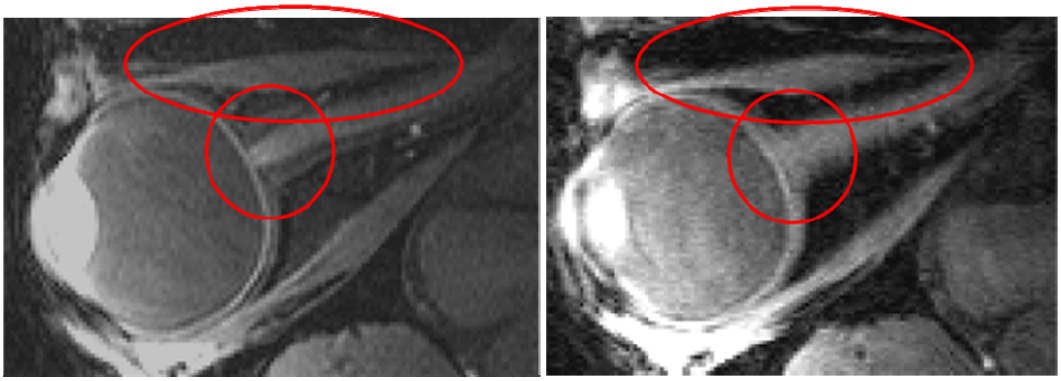

Figure 2.7: (left): central slice of a static experiment (fixed gaze direction 0°, scan time 1.3 min). (right): central slice of dynamic experiment with a k-t BLAST acceleration factor of 3 (max. rotational speed 64°/sec, 17 slices, 18 time frames, scan time 10.5 min, same resolution: 0.4x0.4x1.4 mm^3). At the scleral insertion of the ON (red circle), a slight blurring of the ON tissues is visible. Due to the collinearity of the EOMs' length and the (main) deformation, the blurring of the EOM tissues is less pronounced (red ellipse).

2.3 Velocity- and Motion-Encoded MRI of the Orbit - Introduction

Several prior studies attempted to resolve the deformation of the orbital tissues induced by different eye positions. CT and MRI studies segmented static images to determine the conformation of the orbital tissues. Conventional MR imaging is useful for assessing morphological changes but not for assessing deformations inside homogeneous

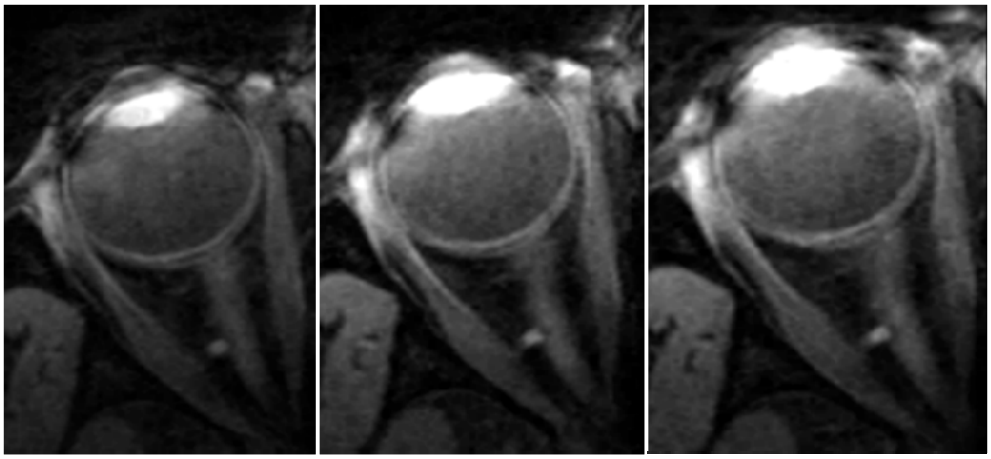

Figure 2.8: Middle slice of high resolution T1-weighted TFE 3D datasets acquired during sinusoidal eye movement with kt BLAST acceleration factors (from left to right) of 3, 6, and 9. The scantimes are respectively 9:09, 4:38, and 3:21. The scantime shortening with an acceleration factor of 9 does not justify the image quality penalty.

structures.[Abramoff, et al. 2000] Sought was a technical solution to resolve movement and deformation inside homogeneous orbital tissues.

The pattern of movement within the EOMs and the surrounding orbital connective tissues is not yet understood.[Miller, et al. 2006] Knowledge about the physiology of the orbital tissues deformation and of the contractility pattern of the EOMs during eye movement is essential to understand the pathology progression in diseases that affect the orbit biomechanics. So far, visualization of the orbital tissues deformation by MRI has been restricted to multi-positional imaging.[Miller and Robins 1987; Shin, et al. 1996; Abramoff, et al. 2000; Demer 2007]

Since no intrinsic contrast can be imaged for distinguishing heterogeneous patterns of deformation within each orbital tissue, morphological changes inside each orbital tissue are not macroscopically detectable. However, an imaging method that is able to directly encode motion could give evidence about the dynamics of such inhomogeneous deformation. Thus, to obtain this type of information, a methodology to generate the first motion- and velocity-encoded MR images of the orbit during eye movements was developed. These images encode the displacement of each image voxel. Therefore, the displacement of each voxel can be tracked over time.

Three methods were tested. The first method named Q-Flow encodes over the MR signal phase the instantaneous velocity of the tissues' voxel motion, as explained in section 1.1.3.3. The second method named CSPAMM (for complementary spatial modulation of magnetization) is a tagging method that encodes the movement over a sinusoidal modulation of the signal intensity. The third method, CDENSE, encodes the displacement in a similar way than CSPAMM, but demodulates the image phase before the acquisition, making the phase proportional to the total displacement since the first time frame.

First, 2D protocols were optimized, to diminish the scan time, and to test the quality of the motion quantification. Once the quantification was asserted for the 2D data, the methodology was adapted to 3D datasets. Here below, the results obtained with each method is presented and discuss their adequacy to fulfill the requirements imposed by the orbital physiology and anatomy.

2.4 Velocity-Encoded MRI of the Orbit

The quantitative cine phase-contrast flow measurement method, Q-Flow,[Moran 1982] is principally used to measure relatively fast convective motions. The displacement during one particular time frame is encoded by bipolar gradient in one particular direction, so that the

resulting phase shift (relative to baseline data) of the MR signal is proportional to the instantaneous speed of the tissue in that direction.[Kouwenhoven, et al. 1995] Therefore, for 3D images the acquisition of four (resp. three for 2D) data sets is needed: one for each of the three (resp. two, for 2D) space coordinate directions and one baseline data. This imposes a four time longer scantime than anatomical images with the same resolution.

In a similar way as for the high-resolution anatomical dynamical imaging of the orbit, the Q-Flow image acquisition was synchronized with the sinusoidal eye movements. A 2D Q-Flow axial slice including the horizontal EOMs was acquired during sinusoidal eye movements with a period of 2 s. Two signal averages were performed to improve the SNR, with the consequence of doubling the acquisition time (see Figure 2.9).

The following acquisition parameters were used:

phase encoding velocity:	5.00 cm/sec in each direction
FOV (ap,rl):	150.0 x 150.0 mm^2
slice thickness:	4.0 mm
scan resolution (x, y):	100 x 110
scan percentage:	110
number of time frames:	30
phase encoding direction:	AP
water fat shift:	1.41 pixels
scan technique:	FEEPI (GE with EPI)
EPI factor:	5
repetition time:	66.60 ms (time frame spacing)
echo time:	10.6 ms
image flip angle:	20.0°
number of averages:	2
"cardiac" (i.e. motion) frequency:	30 per minute
min. and max. RR. interval (motion period):	1980 and 2081 ms
scan duration:	5:58 min:s

The quantitative determination of the tissue velocities determined maximal speeds of approximately 2 cm/s for the sclera, the EOMs, and the ON anterior segment. This result is in concordance with the geometrically expected values, with a maximal rotation speed of the eye of 64°/s. The rotation of the vitreous is phase shifted compared to the one of the sclera. The vitreous exhibit whirl deformation patterns. The orbital fat is deforming during the eye movements with velocities smaller than the one of the adjacent tissues (globe, EOMs, and ON). The high velocities reported at the posterior part of the orbit are due to susceptibility artifacts and low SNR (see Figure 2.10).

The relatively low velocities of the orbital tissues during smooth pursuit compared to blood flow impose the use of higher flow encoding bipolar gradients. For the eye movement speed used, twice bigger flow encoding gradients might be used. This high demand on the gradient system makes the acquisition more sensitive to gradient imperfections and field inhomogeneities. The use of field monitoring should help to correct such inaccuracies, as well as background phase (i.e. velocities) offsets.[Barmet, et al. 2008] On the other hand phase-contrast MRI is less prone to B1 inhomogeneities than tagging with image-space tracking.

However, the integration of the instantaneous velocities to track the motion of one particular tissue point over the whole eye movement range is prone to errors as the noise accumulates over the time frames.

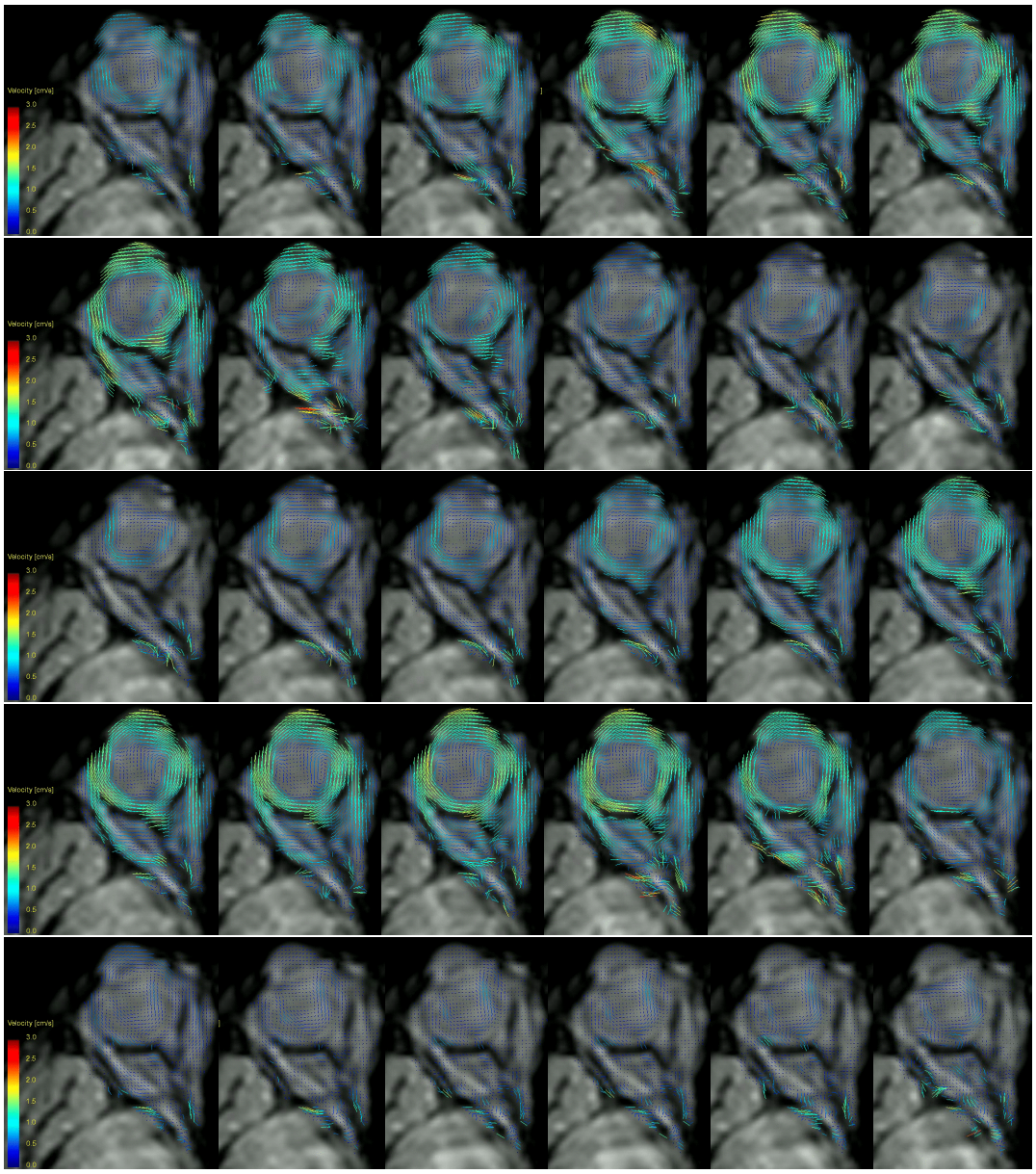

Figure 2.9: the 30 times frames of the quantitative velocity measurements during sinusoidal eye movements with a period of 2 s. The highest velocities can be seen at the globe periphery and the anterior segments of the EOMs and the ON. Noteworthy is the phase shift between the sclera and the vitreous rotations. The big tissues velocities reported at the posterior part of the orbit are due to susceptibility artifacts and low SNR. The orbital fat is deforming during the eye movements with velocities smaller than the one of the adjacent tissues (globe, EOMs, and ON).

2.5 CDENSE Images of the Orbit

The displacement encoding method CDENSE, see section 1.1.3.2, is most suited to track small deformations of small objects, as e.g. mouse hearts.[Gilson, et al. 2004, 2005] As the EOMs scleral insertions are small (~1 mm) and their path relevant for models of the orbital

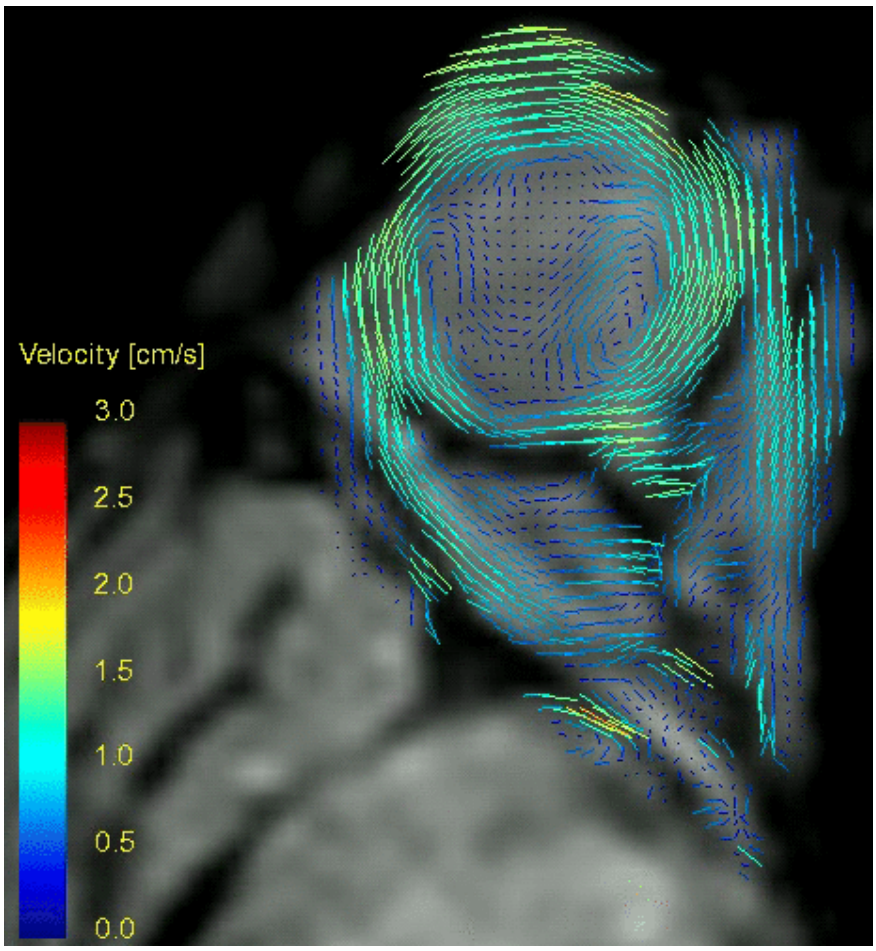

Figure 2.10: Time frame 6 of the preceding Figure. The whirling deformation of the vitreous is clearly visible. At the orbital apex, signal drop at tissues' interfaces impeaches an accurate determination of the local MR signal phase.

biomechanics, the use of CDENSE may be appropriated to depict their deformation. For the CDENSE images acquisition, the visual stimulus was triggered with the motion encoding preparation of the MR acquisition. An advantage of CDENSE compared to CSPAMM is the use of shorter readout gradients, hence diminishing the sensitivity to EPI trajectories imperfect correction and the resulting distortions.

The CDENSE images were acquired only during the first half of the sinusoidal eye movements in order to diminish the T1 fading of the motion-encoding information (i.e. of the tagging pattern). The second half of the eye movement was used for signal recovery (see Figure 2.11).

The following acquisition parameters were used:

encoding strength:	3,6 mm/pi in each direction
FOV (ap,rl):	154 x 154 mm^2
slice thickness:	5.0 mm
scan resolution (x, y):	128 x 111
number of time frames:	14
phase encoding direction:	AP
water fat shift:	1.55 pixels

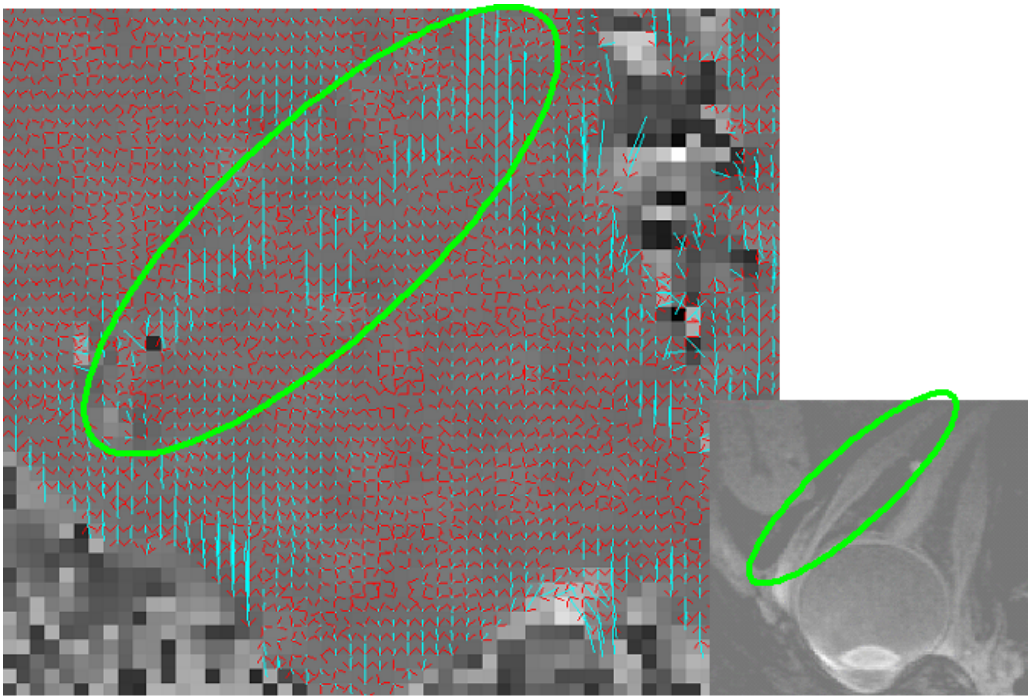

Figure 2.11: Left: CDENSE images of the left eye from one subject, rotation from right 20° gaze to left 20° gaze (counterclockwise rotating in the images; first half of a sinusoidal movement of 2s period). The arrowheads in red indicate the actual position of the tissue voxel. The arrow bodies in blue are 4 times bigger than the real displacement. This image is the first of the 15 time frames of the 2 second period. Therefore, no displacement should be observed here. But, as shown here, the displacements visible at certain locations are the result of distorted phase information due to susceptibility artifacts between the orbital bone and the muscle, and the muscle and the orbital fat, respectively (green oval). Right: Anatomic image with the same FOV.

scan technique:	FEEPI
EPI factor:	5
TR:	70.0 ms (time frame spacing)
TE:	4.8 ms
image flip angle:	25.0°
NSA:	4
cardiac (i.e. motion) frequency:	29 per minute
min. and max. RR. interval (motion period):	2000 and 2101 ms
scan duration:	6:30 min:s

To obtain sensibility of sufficient quality for displacement over the entire range of eye movement of 40°, a strong encoding strength (3,6mm/pi) was used. Unfortunately, this strong encoding strength caused phase wrapping, which was corrected with a phase unwrapping algorithm. This algorithm though, did not correct all the phase wraps for all recorded time frames (see Figure 2.12). Therefore, a satisfactory post processing of the images could not be correctly performed.

This method is sensitive to susceptibility artifacts, as only one peak of the Fourier space is scanned, so that peak-combination could not be performed. This can be solved by acquiring the two peaks separately in two scans. The high resolution aimed with the use of CDENSE conflicts with the movement size that have to be tracked. The high resolution aimed imposes strong encoding gradient strengths i.e. a short encoding strength (corresponding to a short tagline

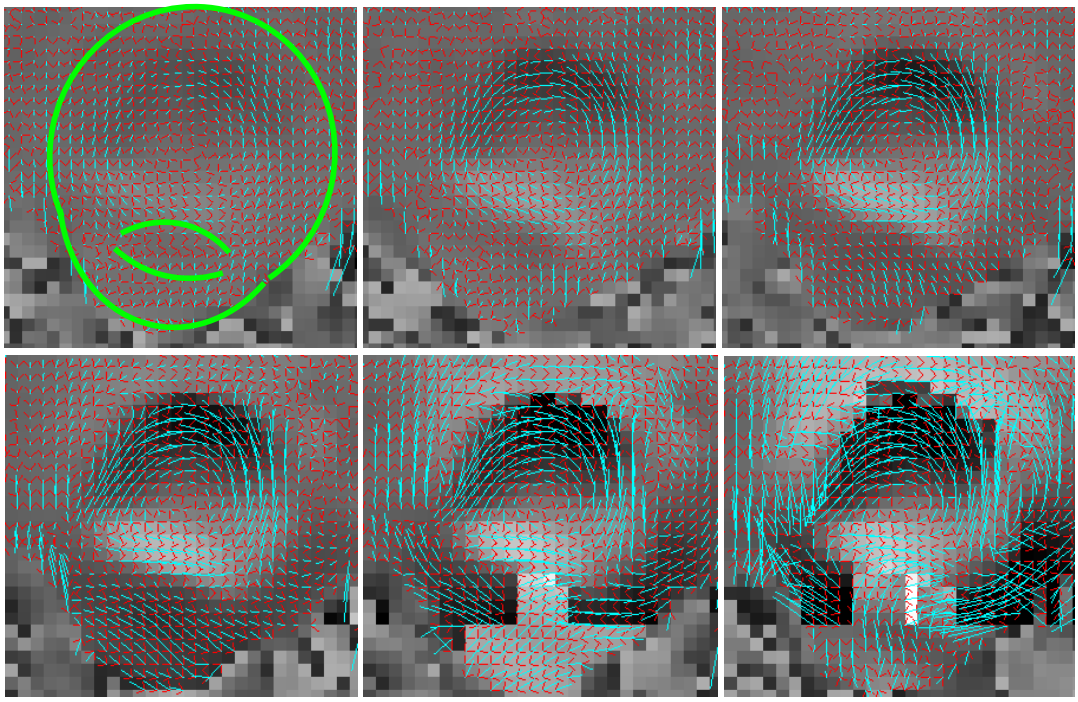

Figure 2.12: Time frames 2 to 7 of the dynamic CDENSE images of the counterclockwise rotating eye. On the top-left: time frame 2, 70 ms after the first time frame. The sclera and the eye lens approximate positions are depicted in green. On the bottom-left: time frame 5 after 350ms, without phase wraps. The phase shift between the rotations of the vitreous and of the sclera is clearly depicted. On the bottom-middle: time frame 6 after 420ms. A phase wrap is visible at the lower image part. The postprocessing algorithm tracking the phase gives an erroneous result. On the bottom-right: Image after 490ms. Multiples phase wraps generate a chaotic displacement.

distance for CSPAMM). This strong encoding gradients result in a multitude of phase wrap that cannot be satisfactorily corrected with the phase unwrap algorithm used.

The inherent (nearly) half SNR pro scantime of CDENSE relative to CSPAMM using Cartesian readout was an additional argument to test CSPAMM capacities for the imaging and quantification of the orbital tissues deformations.

2.6 CSPAMM Images of the Orbit

The MR-tagging sequence CSPAMM[Fischer, et al. 1993] is able to capture the motion of tissues relative to a fixed spatial referential system, see section 1.1.3.2. Before image acquisition, the tissues are tagged using a periodical modulation of their magnetization in two perpendicular directions. The resulting images look like anatomical images modulated by a grid pattern (see Figure 2.13, Panel B at time 0 s). The period of the sinusoidal modulation is termed the tagline distance. Since the modulation is used as marker, equivalent tissue markers are present at every tagline distance. As the magnetization moves with the underlying tissue, the displacement of each tissue point can be followed during the entire recording. The motion of tissue points can even be visually tracked directly from the MR images without postprocessing. This method permits detailed studies of normal EOMs in vivo and depict the deformation of soft orbital tissues during smooth movements of the eye.

2.6.1 2D CSPAMM Images of the Orbit

Subjects with visual acuity sufficient to track the visual stimulus described above were selected. To compare the deformation of the EOMs with the ON, the complete muscles and ON were required to be visible within one image plane of 4 mm thickness.

Images were acquired on all subjects from right to left horizontal gaze. A slight up-gaze position, dependent on the subjects' anatomy, was necessary for imaging the ON in the same plane as the horizontal rectus muscles.

Transversal MR images were acquired with a fast gradient echo sequence. The right-to-left horizontal eye movement of 40° was split into fifteen time frames of 70 ms (1050 ms acquisition period). The remaining 950 ms of the 2 s periodic eye movement served for signal recovery (see Figure 2.13). The relatively short time frame duration of 70 ms was chosen so that the deformation of the orbital tissues between two time frames was small enough to allow tracking. The FOV was selected big enough to avoid fold over artifacts. The scan resolution: $1.2 \times 1.2 \times 4.0$ mm^3 was limited by scan duration and signal to noise ratio (SNR). EPI shortened the acquisition time.

The following acquisition parameters were used:

tagline distance:	2 to 3mm
FOV (ap,rl):	111 x 140 mm^2
slice thickness:	4 mm
scan resolution (x, y):	176 x 88, switched according to tagline direction
number of time frames:	15 to 32
phase encoding direction:	switched according to tagline direction
water fat shift:	2.41 pixels
scan technique:	FEEPI (GE with EPI)
EPI factor:	5
TR:	70.0 ms (timeframe repetition time)
time frame duration:	12 ms (time frame duration)
TE:	7.3 ms
last time frame flip angle:	47°
NSA:	8
cardiac (i.e. motion) frequency:	29 per minute
min. and max. RR. interval (motion period):	2000 and 2101 ms
scan duration:	4:04 min:s (8min for 32 timeframes)

One advantage of the motion encoding technique in comparison to conventional MRI is that tissue deformation can be resolved. Since the magnetic property of the orbital tissues is modulated, it can be used as marker for the tissue deformation. Moreover, this method is noninvasive, i.e., no physical markers are necessary to track the deformation of orbital tissue while the eye is moving. The tagline distance should measure at least twice the maximal tissue displacement between two time frames, as postprocessing software assign the nearest equivalent tissue point of the next time frame to each tissue point and cannot differentiate equivalent markers. Otherwise, a movement in the wrong direction could be assigned to a tissue point. To select the appropriate tagline distance, the expected movement of the orbital tissue was calculated as follows: assuming the ocular globe including the adjacent connective tissues builds a 25- to 35-mm diameter sphere that rotates 64°/s during 70 ms (=4.5°) following the moving stimulus, the surface of such a sphere shifts 1.4 mm at

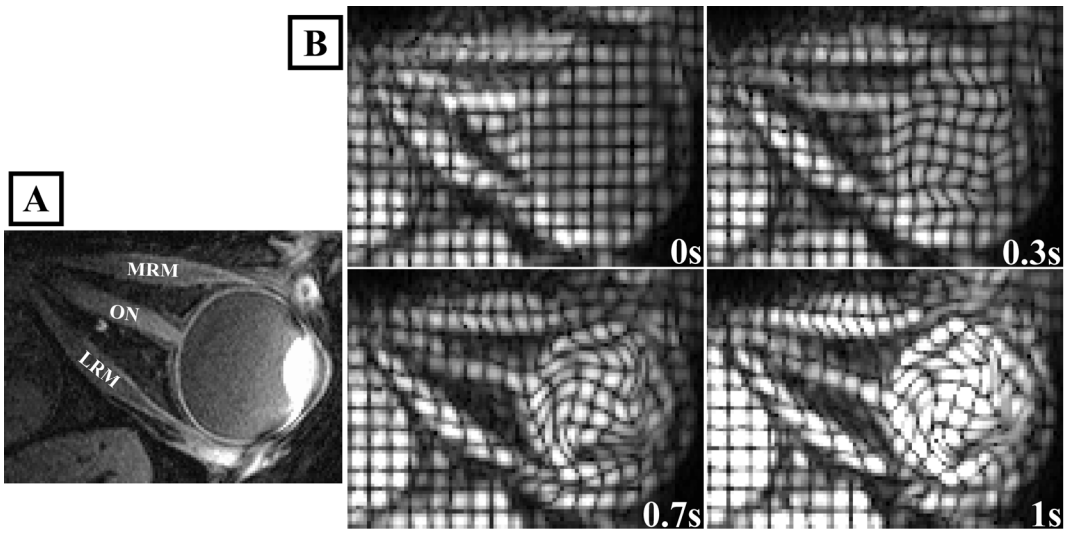

Figure 2.13: (A) Static MR image of the right orbit without tagging. The ON, the LRM, and the MRM are depicted in the image plane. (B) Four CSPAMM MR images of the same slice during eye movement. The magnetization is modulated to create a grid bind with the tissue (see time 0 s). The deformation of this grid (during time) depicts the differential movements within homogeneous tissues, such as in the EOMs. The 1st, 5th, 10th, and 15th time frames are shown. The temporal resolution was 70 ms. These images are from the same subject (Subject 1).

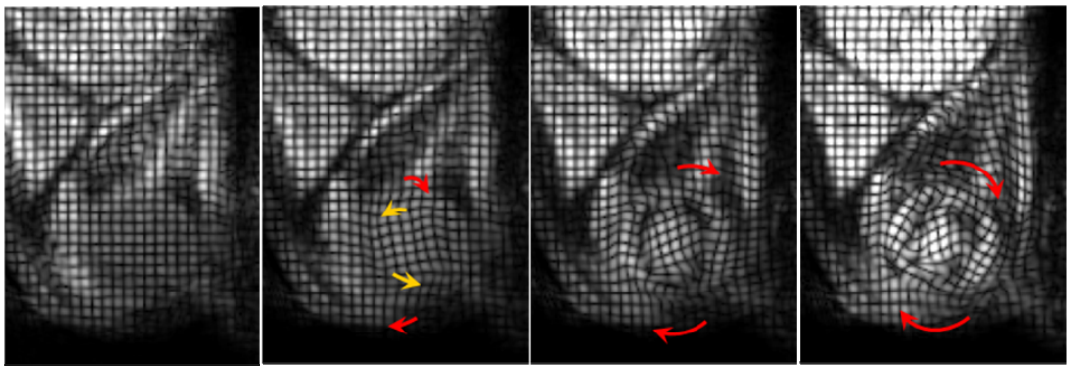

Figure 2.14: Four CSPAMM MR images with a tagline distance of 2 mm. The 1st, 5th, 10th, and 15th time frames are shown. The temporal resolution was 70 ms. Other parameters were: 256x151 scan-matrix, Resolution: 0.6x0.9x4 mm^3, EPI factor 5, 21 time frames, Scan time: 6:10 min. The phase shift of the vitreous rotation relative to the eye movement and the resulting whirling of the tissue are clearly visible.

most (4.5° x diameter x pi/360°). A tagline distance of at least a double sphere shift (3 mm) was needed. A larger tagline distance would increase the sensitivity of the measurement to noise and would consequently need extended scan time for compensation.

A good shimming (homogenization of the static magnetic field) prior to image acquisition is essential to assure a good delineation of the tagline. The gradient echo EPI sequence used for faster acquisition in this study is sensitive to the magnetic susceptibility artifacts,[Chen, et al. 2005] which are prominently present in the orbit.[Herrick, et al. 1997] Further, the MR image deformation due to these magnetic field imperfections is also an issue for reformatting the anatomical data with the tagging data, e.g. to ascertain that tissue landmarks lay on the expected tissue.

Motion-encoded MRI acquires images during several time frames (see Figure 2.14) during a single acquisition. To maintain a reasonable scan time, the scan resolution was ten times lower than the one used for high-resolution conventional MRI.[Kau, et al. 2006] An evident limitation of the low resolution is the inability to resolve diverse structures within EOMs, as, for example, the global and orbital EOM layers. Nevertheless, as about twenty pixels are acquired in the longitudinal direction of the muscles, this method is capable of resolving muscles' longitudinal segments. The limited resolution mainly affects the interface of differently moving tissues. Since the anterior segments of the EOMs are thin, their tracking is more difficult than the middle or posterior segments. To diminish the partial volume effect in the outer layer of the EOMs, the signal was optimized by taking advantage of the specific T1 of muscles. Note that the tagline distance is not important for resolution. The tagline distance gives only the period of the phase information. The resolution of the phase information used for the tracking is limited by the scan resolution and the size of the postprocessing filter.

2.6.2 3D CSPAMM Images of the Orbit

A lack of movement may be due to contraction or relaxation deficits of each of the six EOMs or due to rigid surrounding orbital connective tissue. The orbital tissues deform along all three dimensions even for simple horizontal or vertical eye movements. Due to the anatomical arrangement of the EOMs in the orbit,2D Tagging, presented above, allows to track only two muscles out of six, and requires accurate planning. This study will provide basics for a new fast scanning method that provides 3D CSPAMM[Rutz, et al. 2008] high-resolution MR images of the whole orbit, in a scantime short enough to enable motion reproducibility.

A similar setup as described above has been used to acquire 3D CSPAMM TFEPI-images (see Figure 2.15 to Figure 2.17). Three datasets which were each motion encoded in one spatial dimension were acquired. A reduced field-of-view method with a localized tagging preparation was applied in order to keep acquisition time short. In order to prevent tag fading, an optimized ramped flip angle approach was applied.[Fischer, et al. 1993]

The following acquisition parameters were used:

tagline distance:	3mm
FOV (ap,rl,fh):	45 x 45 x 45 mm^3
scan resolution (x,y,z):	32x15x15, switched according to tagline direction
number of time frames:	15
phase encoding direction:	switched according to tagline direction
water fat shift:	1.06 pixels
scan technique:	3D TFEPI (TFE with EPI)
EPI factor:	3
TFE factor:	3
TR:	70.0 ms (timeframe repetition time)
TE:	4.0 ms
last time frame flip angle:	44°
NSA:	6
cardiac (i.e. motion) frequency:	29 per minute
min. and max. RR. interval (motion period):	1984 and 2085 ms
scan duration:	9:03 min:s

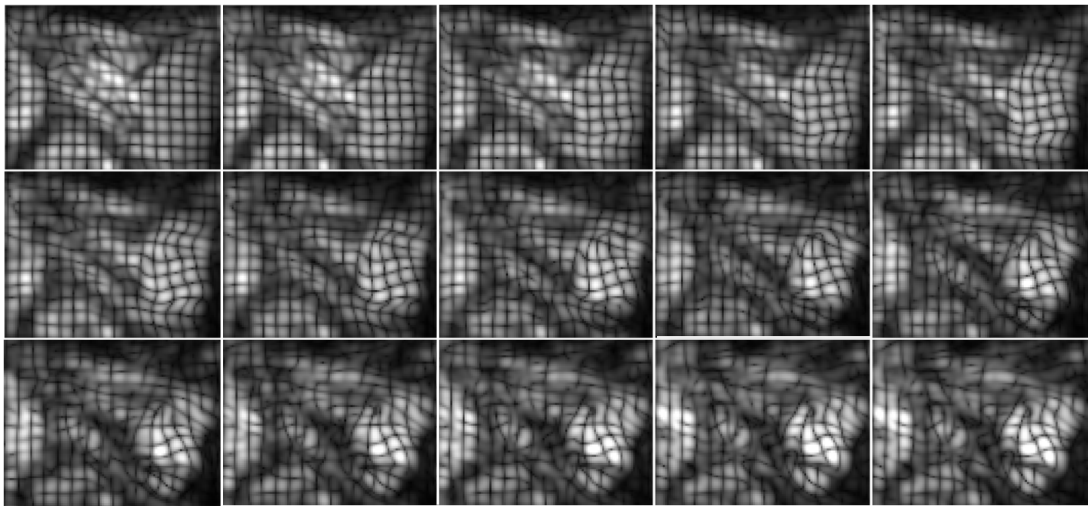

Figure 2.15: The middle slices of 15 time frames of the 3D CSPAMM data of the right orbit during left-to-right eye movement with a temporal resolution of 70 ms.

The accelerated 3D tagging acquisition technique used in this study enabled to track the deformation of EOM, in a tolerable scantime. Further studies plan to investigate the ability of this technique to differentiate pathologic from the physiologic muscle contraction pattern.

2.7 Motion Artifacts Suppression

The sinusoidally moving gaze target used to stimulate repetitive eye movements was sufficient to produce dynamical images with high spatial and temporal resolution. Nevertheless, some motion imperfection of the eye induced image artifacts in the phase encoding direction of the MR data. The sharp signal drop at the cornea-air interface is particularly sensitive to motion imperfections, as a small displacement induces an important local signal change. This effect is even amplified by the high sensitivity of the surface coil in this region, as the coil was placed just anterior to the eye. Due to the properties of the Fourier transformation, this local blurring in the anterior part of the eye propagates in the anterior part of the orbit. This aberrant signal in the posterior part of the orbit overlaps the true signal. For tagging data, this implies a slight deformation of the tagging pattern.

To avoid a small motion imperfection to disrupt the whole image several methods are here proposed, on the example of the tagging data. These methods can also be used for the other imaging techniques presented above.

The FOV and the tagging pattern can be rotated by 45°, so that the phase encoding direction is not parallel to the axis of the orbit. The result so obtained were satisfactory, nevertheless, a small disruption of the signal stability for the anterior part of the EOMs was still present.

To diminish the signal drop in the vicinity of the surface coil, a saturation pulse can also be applied on the anterior part of the eye ball using REST slabs. First, the effect of static REST slabs was investigated. The number of timeframes before which the REST slab needs to be applied to obtain a sufficient suppression of the motion artifacts was indagated. Secondly, the angulation of the REST slab was modified in accordance to the eye rotation induced by the gaze target stimulus. Here, too, the number of timeframes before which the REST slab needs to be applied to obtain a sufficient suppression of the motion artifacts was indagated.

Using REST slabs, motion artifacts were satisfactorily suppressed. AN application of the saturation pulse for the first timeframes did already improve the image quality. Nevertheless, the

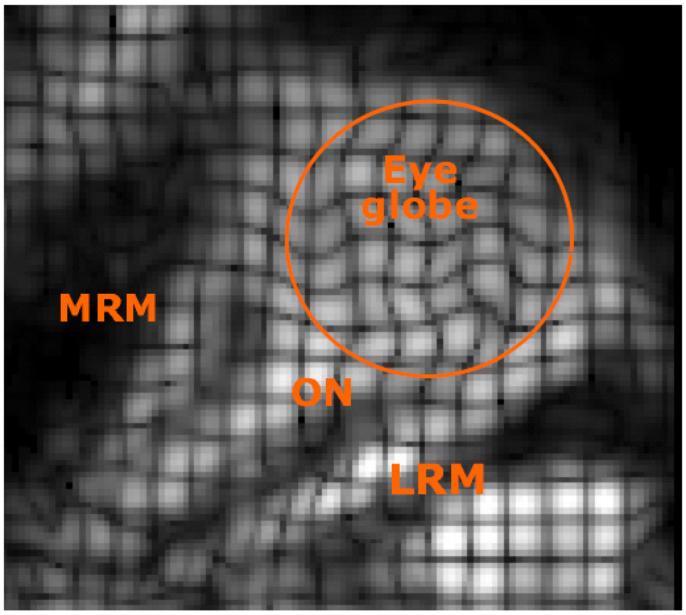

Figure 2.16: Central slice of 3D CSPAMM dataset on the 5th time phase (out of the 15). MRM: medial rectus muscle. ON: optic nerve. LRM: lateral rectus muscle.

best results were obtained when applying the REST slab on each timeframe. For this, the rotating REST slab were more suited, as they saturated a smaller part of the eye ball and allowed a better visualization of the EOMs' scleral insertion.

A total suppression of the motion artifacts was obtained with these methodologies. Nevertheless half plan geometry for the REST slab would enable a smaller portion of the eye ball to be saturated and enable a better visualization of the EOMs insertion. This methodology is primarily useful for investigations of the posterior part of the orbit.

2.8 Conclusion

Motion- and velocity-encoded MRI of the orbit during eye movement are versatile and noninvasive methods which permit detailed studies of normal and pathologic EOMs in vivo with good resolution of the deformation of soft orbital tissues, even in regions where physical markers or devices cannot easily be implanted, such as the orbital apex. This methodology may have a number of potential clinical benefits by identifying specific patterns of deformation in different diseases of the orbital muscles (e.g., thyroid orbitopathy, orbital pseudotumor) or in conditions which alter the innervation to eye muscles (e.g., acquired or congenital aberrant innervation).

An advantage of measuring quasi instantaneous velocities, in comparison to global displacement with CSPAMM and CDENSE, is the ability to diminish signal void due to whirling motion. The flow pattern inside the vitreous can still be depicted despite the presence of several vortices in the vitreous of that subject. Further, even in the case of big deformation of the whole movement range, the accurate determination of the deformation during each time frame is still possible.

Acceleration of the Q-Flow MRI is also possible using kt BLAST and kt SENSE.[Baltes, et al. 2005] The use of the only recently available two element microscopy surface coil at 3T would enable the use of kt SENSE for cine phase-contrast flow measurement of the orbit.

To further enhance the spatial resolution of the images, a specialized coil array will be needed. Due to the 58ms delay between two consecutive timeframes, the temporal resolution could be

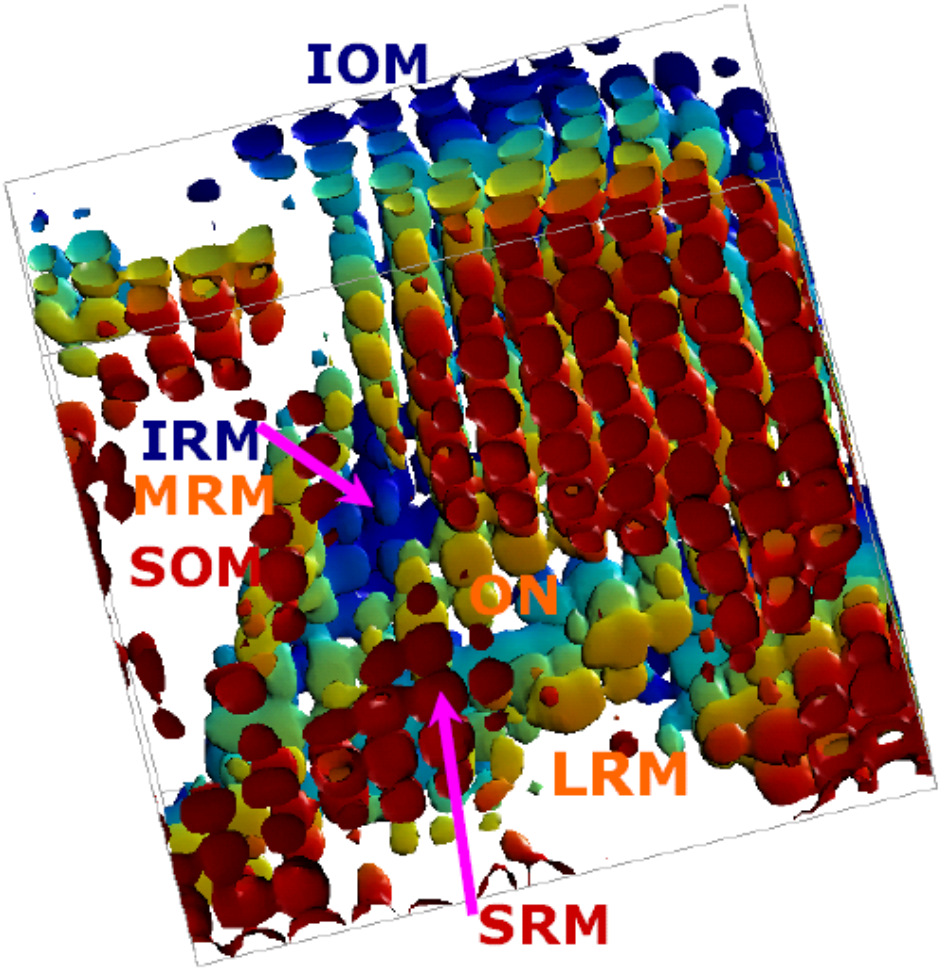

Figure 2.17: 3D isosurfaces representation of the tagging dataset representing the eyeball, the ON and the six EOMs. Color encoding corresponds to the cranio-caudal coordinate as follows: the orange level is approximately the slice of the previous Figure with the MRM, ON and LRM in orange; in red are the lower part of the SRM and the SOM (the top is cut for visualization); in blue: are the IRM and the IOM.

improved without the need to adapt the other scan parameters. With a better temporal resolution, EOMs contraction may be imaged during saccades. To reach this goal, the accuracy of the eye movement needs to be verified with simultaneous eye movement measurements.

After that the SNR was improved to enable automatic tracking of the tissue deformation, CSPAMM showed the greatest potential for the quantification of the orbital deformation. For the eye movement velocity range aimed, CSPAMM showed a greater immunity against magnetic field inhomogeneities than Q-Flow. CSPAMM is also twice more SNR efficient than CDENSE. Therefore, CSPAMM was chosen to conduct the application studies presented below. Nevertheless, to enable a stable quantification of the tissues' deformation depicted using CSPAMM; a dedicated - model free - tracking algorithm had to be developed.

Chapter 3: Methodology for the Postprocessing of CSPAMM Images for the Quantification of the Deformation

In this chapter, the quantification algorithm developed to obtain the orbital tissues' deformation obtained from CSPAMM data is presented. Paragraph 3.2 has been published in [Piccirelli, et al. 2007]. The results presented in Section 3.3.2 were partially obtained in collaboration with Maria del Carmen Fuentes during her Master diploma thesis. The results presented in Section 3.3.3 were partially obtained in collaboration with Leilei Wu during his semester practicum.

3.1 Introduction

For objective quantification of the relative motion of tissue points, an automatic tracking method is necessary.[Maier, et al. 1992a, b; Ryf, et al. 2006] The postprocessing of the tagging data can be effectuated by tracking the (dark) lines within the MR magnitude image with dedicated algorithms.[McVeigh 1996; Botha, et al. 2005] The postprocessing can also use the phase information of the MR data, as introduced in [Osman, et al. 1999]. A further improvement of this postprocessing technique was the use of peak-combination to.[Ryf, et al. 2004b] HARP phase tracking has a bigger independence from the MR signal magnitude.

Most postprocessing tools are originally developed for assessing the deformation of the myocardium. However, because the anatomy of the EOMs are fusiform and hence differs from circular anatomy of the cardiac muscles, the postprocessing tools were modified to better account for the shape of the studied tissues.

Taking advantage of CSPAMM images of the orbit, the heterogeneous deformation along the rectus muscles and the ON in healthy subjects is investigated hereunder. It is useful for strain calculation and tracking error corrections to embed the landmark to be tracked into geometrical structures. First, the ability and reliability of landmark polylines to quantify the deformation of the orbital tissues were tested. A reliability study was performed and the results are presented in section 3.2.

To increase the number of independent segment that could be tracked along the rectus muscles, to enable a more reliable quantification of the orbital tissues' deformations, and to facilitate the drawing of the polylines, the tracking algorithm was modified. Now, the landmarks are linked to each other by embedding them into a 2D (respectively 3D) grid structure called *mesh*. This dedicated tracking algorithm is based on the continuity and smoothness of the deformation within each tissue.

Visualization tools for the mesh algorithm are also presented in section 3.3.

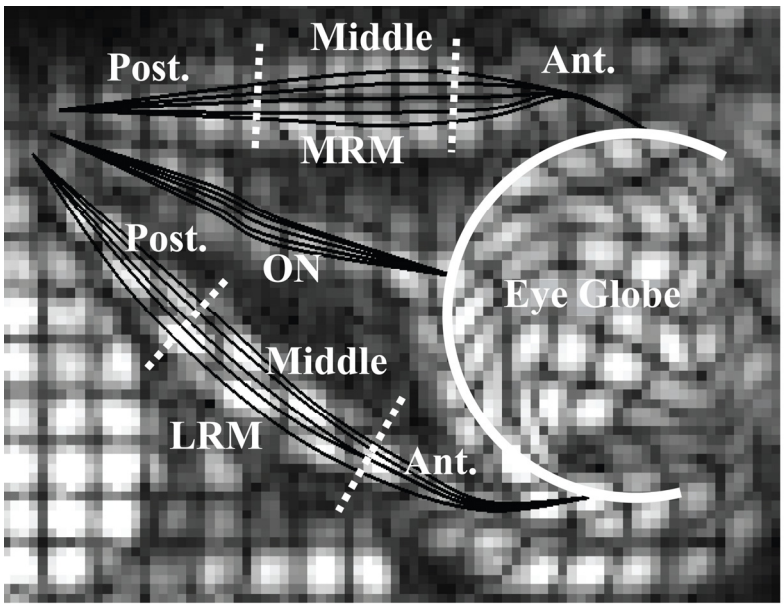

Figure 3.1: CSPAMM image of the 10th time frame (out of 15) including the manually embedded polylines in one subject. Five polylines served to track the whole thickness of the two horizontal muscles and the ON. The muscles and the ON were divided into three portions of equal lengths at gaze straight ahead (Anterior, Middle, and Posterior segments).

3.2 Polylines of Tracked Landmarks

This Section has been published in [Piccirelli, et al. 2007].

3.2.1 The Study Design

Normative data of the EOMs' deformation of healthy subjects were sought and, therefore, quantified using polylines of HARP tracked landmark for the postprocessing of CSPAMM images of the orbit. As the comparison of the local deformation of the horizontal EOMs with the one of the ON was aimed, two subjects with a strongly curved ON were excluded because their ON could not be completely visualized in the same transversal image plane as the horizontal EOMs. Seven healthy volunteers (two women and five men; mean age: 36 years; range: 27 to 62 years of age) were included for further analysis. These seven healthy subjects gazed at a horizontal sinusoidally oscillating target - see preceding Chapters. A small surface coil was placed in front of the right orbit for CSPAMM imaging.

Using a supramillimetric resolution, at first several neighboring tissue points of the EOMs that are expected to have a similar motion are tracked and the variation of the results is investigated, to qualify the tracking reliability. For this, the change of the distance between each marker was calculated. Then, the normative physiological data range that was obtained for healthy subjects is presented. The contracting and relaxing horizontal rectus muscles and the non-contracting ON were reliably tracked. The differential contractility of the EOMs could be distinguished from the third time frame on (=140 ms from the beginning of the right to left eye movement lasting 1 s). The muscle belly of the contracting medial rectus muscle (MRM) could be distinguished from the posterior and the anterior segment from the sixth time frame on (=350 ms).

3.2.2 Postprocessing

An adapted software program based on TagTrack 1.5.6 (GyroTools Ltd.; Zurich; Switzerland) was used to track the marked tissue points automatically. The postprocessing method HARP[Osman, et al. 1999] with peak-combination[Ryf, et al. 2004b] is integrated into this software. HARP enables tracking of all tissue points, not just the tagging lines (dark lines of the grid), because it tracks the phase and not the MRI magnitude information. To understand motion-encoded MRI with HARP evaluation, it is important to distinguish the distance between equivalent markers (the tagline distance) from the acquired pixel size, which is always smaller.

A circular band-pass filter was applied to extract the harmonic peaks in Fourier space and to diminish image noise. A filter diameter that doubles the image pixel size is the theoretical optimum of the HARP method. The size of the filter (which corresponds to a diameter of 2.7 pixels of the image) was selected as a trade-off between tracking stability and movement resolution. The filter was centered on the harmonic peak (of the sinusoidally modulated image) and enabled us to resolve a maximal contraction of 53% of the original tissue length at the first time frame. The maximal resolvable contraction with the optimal theoretic filter is given by the scan resolution (1.2 mm) divided by the tagging line distance (3 mm),[Osman, et al. 1999] i.e., 40% (i.e., 2.5 times shorter). Hence, the degradation due to filtering is reasonable. There is no limitation for the maximal trackable elongation of a tissue.

The horizontal EOM thickness of about 3 mm[Kaufmann and Decker 1995] was covered with at least one pixel that lay completely inside the muscle after filtering. Therefore, landmark chains traced and tracked on these pixels along the muscles were expected to describe similar motion. A good tracking technique should render similar motion for landmarks in the same pixel. To test the quality of the tracking algorithm, five landmark chains (=polylines) for each horizontal rectus muscle and the ON were manually drawn on the 10th time frame (approximately gaze straight ahead) such that the whole tissue broadness could be used for tracking (see Figure 3.1). For each polyline, TagTrack interpolated about 70 equally spaced points, which were tracked through the 15 time frames (see Figure 3.2). The StdDev of the motion pattern of the polylines was calculated for the validation of the tracking algorithm. A small StdDev corresponds to a good tracking quality of the algorithm. To ascertain that the polylines lay on the expected tissue, advantage was taken from anatomical images and realigned the polylines if they were not on the muscles of interest.

The length of each polyline was defined as the sum of the distances between neighboring landmarks along the polyline. As reference length, the average of the length of the first and second time frames (20° right gaze) was selected. This improved the SNR and was justified by the fact that the eye moved less than half a pixel during the first two time frames. The deformation (relative length change) of each polyline was calculated by dividing its length at the actual time frame by its reference length. Furthermore, each polyline was divided into three segments of equal length. The changes of length of the horizontal rectus muscles as well as of the three EOM segments of the seven subjects were statistically analyzed by the Kruskal–Wallis test (ANOVA without Gaussian distribution assumption).

3.2.3 Results

Panels A and B of Figure 3.3 show representative tracking results of the right LRM, MRM, and ON of two different subjects. The LRMs of the right eye elongated +22% in Subject 1 and +19% in Subject 2 during 20° right to 20° left gaze. All five polylines of the LRM showed a consistent elongation as their StdDevs did not exceed 1% during the 15 time frames. Meanwhile, the MRMs of both subjects contracted from baseline to 83% with a length variation between the polylines of less than 2% in Subject 1 and 0.5% in Subject 2. The four times larger StdDev of the MRM

polylines of Subject 1 compared to Subject 2 is explained by the tracking imperfection of the polylines of the MRM of Subject 1: Polyline crossing can be observed on Figure 3.2 at the first

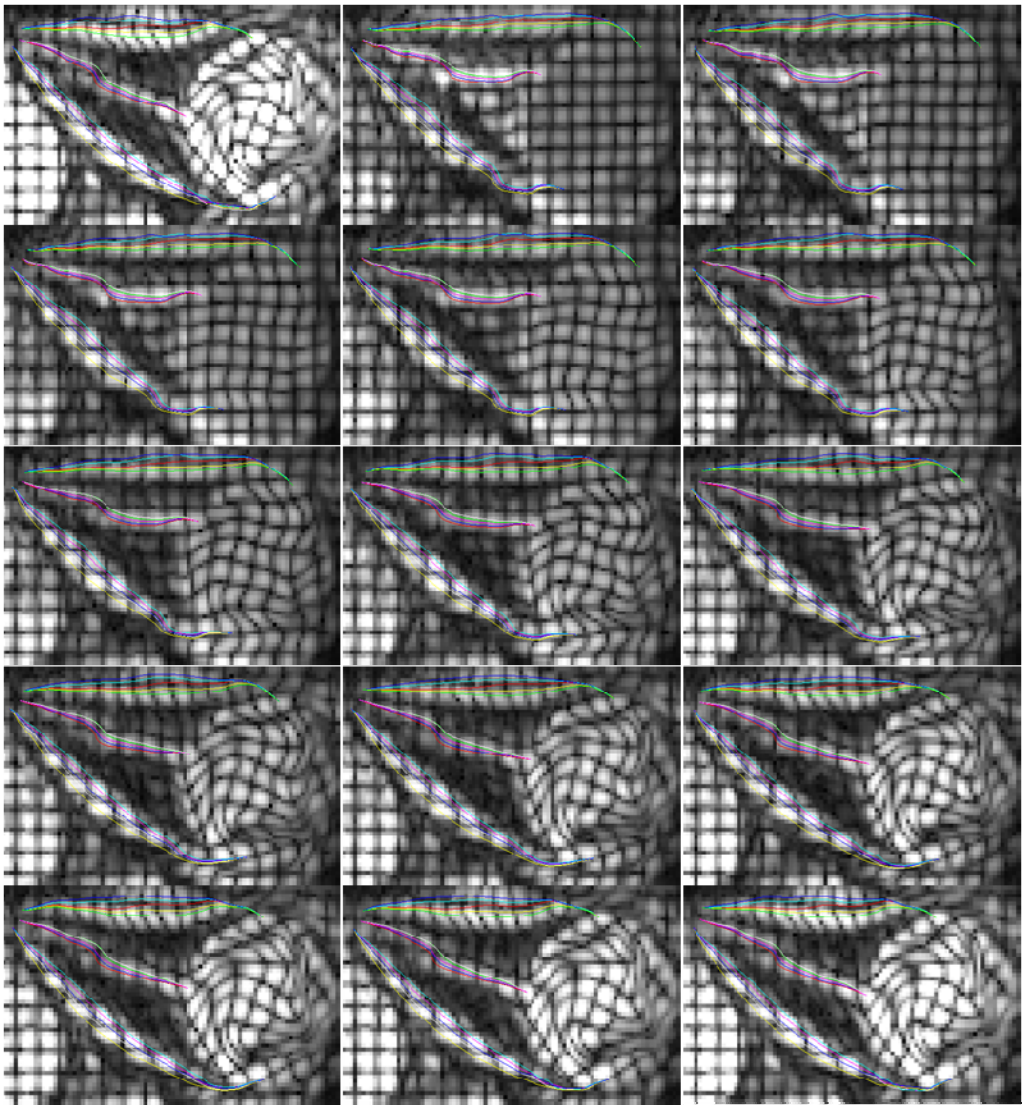

Figure 3.2: CSPAMM images of all 15 time frames including the manually embedded polylines (in color) in one subject (Subject 1) gazing from 20° right to 20° left. Five polylines served to track the two horizontal muscles and the ON of the right eye.

time frame. As expected, the deformation patterns of both muscles were nearly sinusoidal corresponding to the sinusoidally oscillating right eye. The average length of the five polylines of the ON varied between 102% and 98% in Subject 1 and between 100% and 96% in Subject 2. For Subject 2, the StdDev of the five polylines of the ON was slightly greater than in the two rectus muscles but was still smaller than 2%. Subject 1 did not show a greater StdDev of the ON polylines compared to the EOM polylines. The mean of the StdDev of all subjects at each single time frame was smaller than 1% for the three tissues.

The actual lengths of the polylines of the three tissues at the first and last time frames are listed in Panels 3C and 3D. To unambiguously compare the lengths of the different polylines, the average of the lengths at the first and last time frames are considered in this paragraph. For Subject 1, the LRM was slightly longer than the MRM, and the ON was the shortest, as expected. However, the length analysis of the polylines of Subject 2 revealed that the polylines did not represent the

whole length of the labeled tissue, as the LRM polylines were shorter than the MRM polylines. The anterior part of the LRM of Subject 2 was relatively thin so that it was not possible to get

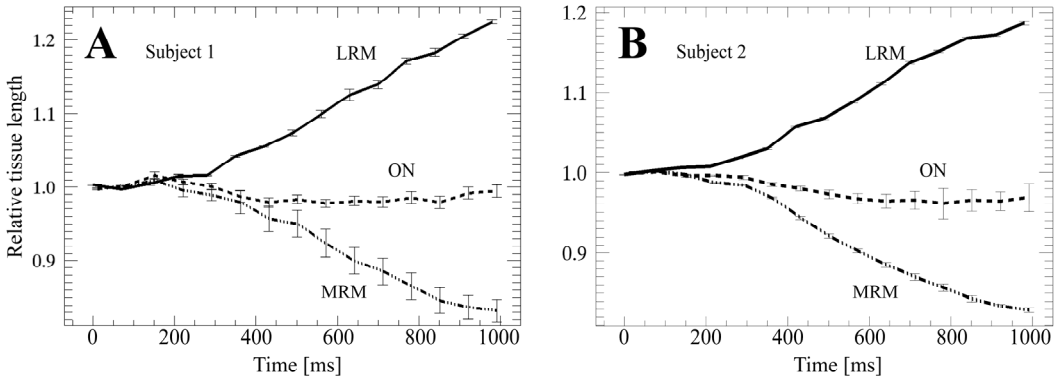

C

Tissue Lengths of Subject 1 [mm]

	20° Right Gaze	20° Left Gaze
LRM	36.1 ± 0.6	44.1 ± 0.7
ON	26.0 ± 0.4	26.0 ± 0.1
MRM	39.7 ± 0.8	33.1 ± 0.1

D

Tissue Lengths of Subject 2 [mm]

	20° Right Gaze	20° Left Gaze
LRM	29.8 ± 0.2	35.4 ± 0.2
ON	23.5 ± 0.2	22.5 ± 0.5
MRM	40.5 ± 0.1	33.6 ± 0.2

Figure 3.3: (A, B) Change of length relative to the tissue length at the first time frame at 20° right gaze. The five polylines of the relaxing LRM, the ON, and the contracting MRM of the right eye are averaged. The tissue deformations of two subjects are depicted during 1 s (from 20° right to 20° left gaze). The movements of the muscles and the ON were distinguishable from each other (error bars: ±one StdDev). (C, D) Length of the polylines of each tissue (of Subjects 1 and 2) averaged for the five polylines at the first and last time frame (errors: ±one StdDev).

reliable tracking of this muscle region.

Both horizontal EOMs and the ON of Subject 2 were further investigated in more details. The top Panel of Figure 3.4 shows the LRM of this subject. This muscle was divided into three segments of equal lengths (at straight-ahead gaze). The middle segment of the muscle (muscle belly) elongated twice as much as the anterior and the posterior segments. This result is expected, since the anterior and the posterior segments of the muscles contain more tendons that cannot stretch as easily as muscle tissue. The larger StdDev of the five polylines at the 15th time frame in the middle and posterior part of the LRM segments was due to partial volume effects that appeared at the interface of tissues with different movements. These effects occurred also in the anterior part of the EOM in other subjects.

Relative to the posterior and anterior part of the muscle, the middle segment of the LRM relaxed earlier and to a larger extent in later time frames. In contrast to the heterogeneously contracting LRM segments, the three ON segments all had a similar degree of longitudinal deformation (see Figure 3.4, central Panel). In this subject, the StdDevs among the five polylines of the ON segments were greater than in the LRM; however, this was not the case for all subjects.

The bottom Panel of Figure 3.4 shows the heterogeneous contraction among the three medial rectus segments. The middle segment contracted ahead of the anterior and posterior segments. This pattern of earlier contraction extended even to the later time frames. The StdDev of the five polylines in each segment was comparable to the segments of the LRM (see Figure 3.4, top Panel). In fact, the average of all subjects' StdDev at each single time frame was smaller than 3% for each segment of the three tissues.

The Figure 3.5 and Figure 3.6 summarize the results in all seven subjects. Figure 3.5 shows a clear separation among the LRM elongation, the ON deformation, and the MRM contraction. The StdDev among the subjects increased over time and was slightly more pronounced in the LRM and the ON than in the MRM. This may be due to the nonlinearity of the deformation scale. Since the StdDev of the subjects was relatively small, there was a statistically significant separation of

the two horizontal EOMs after the third time frame (corresponding to a gaze deviation of 1.9° from the 20° right gaze; see * at 140 ms), and of the three tissues from each other after the fourth

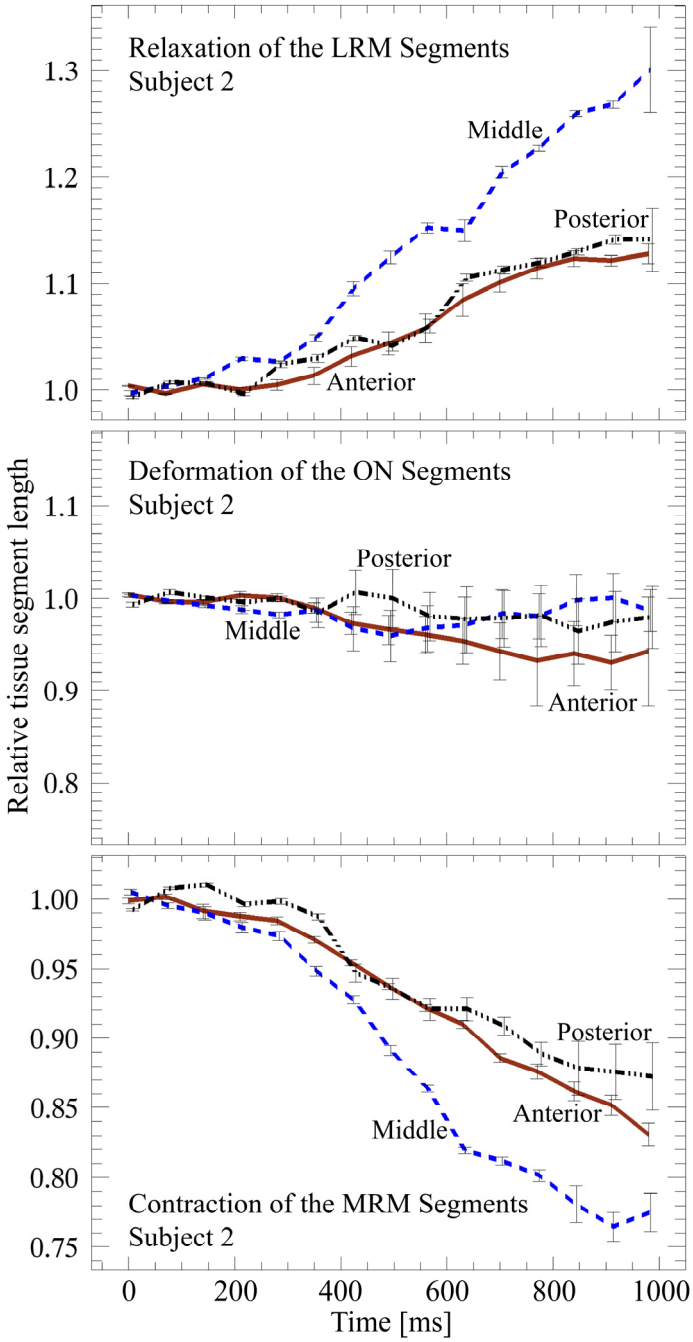

Figure 3.4: Change of relative tissue length of Subject 2 averaged for the five polylines. The LRM (top Panel), the ON (central Panel), and the contracting MRM (bottom Panel) are divided into three segments. The lengths of the segment closest to the eye globe (anterior, brown), the muscle belly or the ON mid portion (middle, blue), and the orbital apex segment (posterior, black) are analyzed. In both horizontal rectus muscles, the middle segments can be distinguished from the anterior and posterior segments. In the ON, however, all segments were similarly distorted (error bars: ±one StdDev).

time frame (corresponding to a gaze deviation of 4.2° from the 20° right gaze; see ** at 210 ms). Figure 3.6 depicts the heterogeneous longitudinal segmental deformation of the LRM (top Panel),

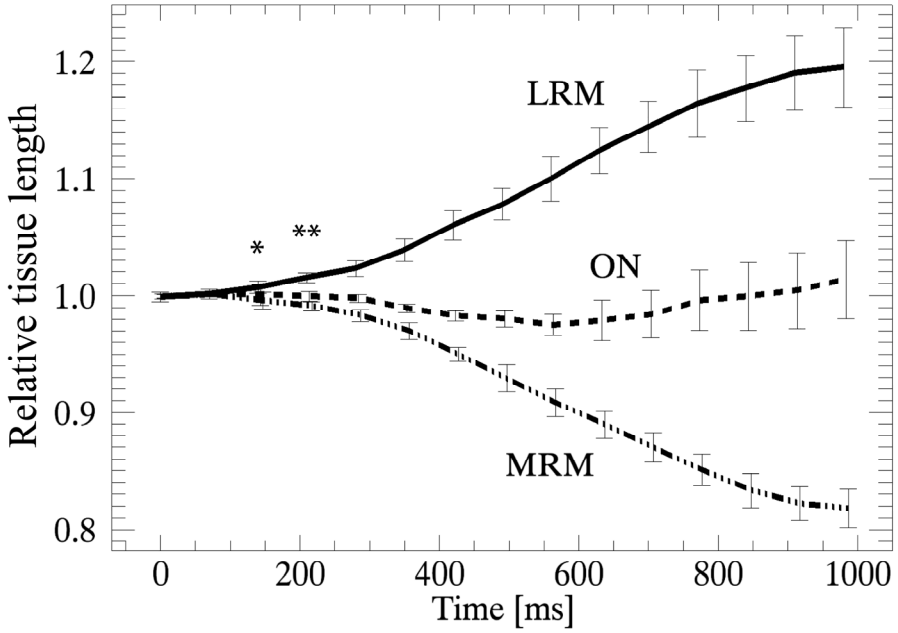

Figure 3.5: Change of length relative to the length at the first time frame for the relaxing LRM, the ON, and the contracting MRM during 1 s of eye movement, averaged over the seven subjects. The StdDev among the subjects was small. A single asterisk (*) indicates that the LRM and MRM were statistically significantly distinguished from the third time frame on corresponding to a gaze deviation of 1.9°. Two asterisks (**) indicate that all three tissues were statistically significantly distinguished from the fourth time frame on corresponding to a gaze deviation of less than 4.2° (error bars: ±one StdDev).

the ON (central Panel), and the MRM (bottom Panel). All length changes were expressed relative to the average length of the first two time frames and averaged for all seven subjects. The greatest relaxation of the LRM was present in the middle segment of the muscle and was greater in the orbital apex than in the anterior segment. The difference between the relaxations of the different muscle segments was statistically significant, so that the muscle segments could be distinguished after just a brief period of eye movement. Examining the LRM (see Figure 3.6, top Panel), the anterior segment was statistically significantly distinguishable from the other two segments from the fourth time frame on (210 ms, see *). From the ninth time frame on (560 ms, see **), all three segments were statistically significantly distinguishable from each other. The separation among the ON segments was not statistically significant in all time frames (see Figure 3.6, central Panel). Considering the MRM (see Figure 3.6, bottom Panel), the middle segment was statistically significantly stronger contracting than the other two segments from the sixth time frame on (350 ms, see *). From the seventh time frame on (420 ms, see **), all three segments were statistically significantly distinguishable from each other. In summary, the posterior and the middle segments of the LRM were the earliest to relax, whereas the middle segment was the earliest to contract in the MRM.

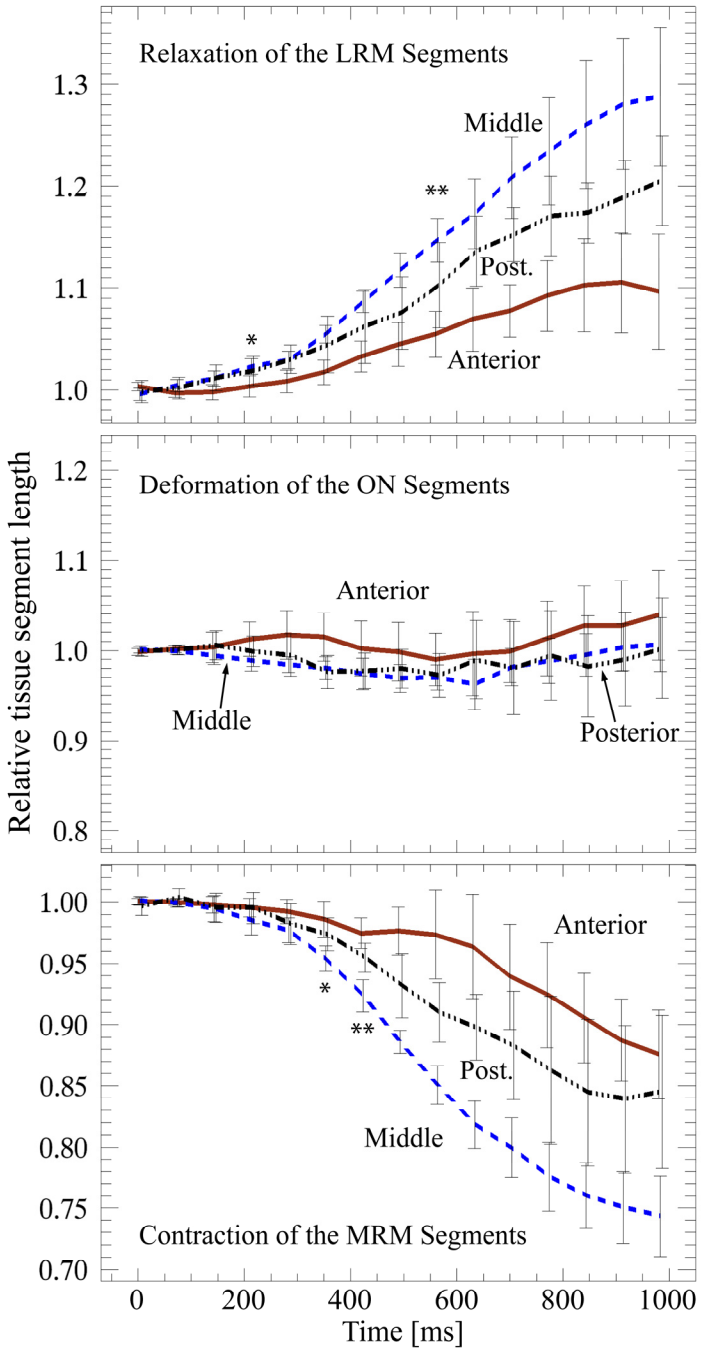

Figure 3.6: Change of relative tissue length averaged for the seven subjects. The LRM (top Panel), the ON (central Panel), and the contracting MRM (bottom Panel) are divided into three segments. The segment closest to the eye globe (anterior, brown), the muscle belly or the ON mid portion (middle, blue), and the orbital apex segment (posterior, black) are depicted. The three segments can be distinguished from each other for both muscles, but are similar for the ON (error bars: ±one StdDev). A single asterisk (*) indicates that, from that time frame on, one segment was statistically significantly distinguishable from the other two. Two asterisks (**) indicate that all three segments were statistically significantly distinguishable from each other.

3.2.4 Discussion

3.2.4.1 Main Findings

Motion-encoded MRI can be successfully used to analyze patterns of EOM contraction during smooth pursuit eye movement. Because the variability among healthy subjects was small, statistically significant differences among the anterior, middle, and posterior segments of the EOMs could be identified. Greater deformation of the muscles was seen nearer to the orbital apex than to the anterior segment of the muscle. As a control, the deformation along the ON was homogeneous.

In both horizontal EOMs, the anterior segment was the last segment that deformed. This may be due to the great percentage of tendon within this segment. Nevertheless, there was a slightly different distribution of the pattern of deformation between the MRM and LRM. The posterior segment of the LRM relaxed before the comparable segment in the MRM contracted. One can speculate about the heterogeneous pattern of deformation between the two muscles. The dynamics of the deformation pattern of a muscle could be different during contraction and relaxation. Future experiments, including the analysis of the eye movement in the other (left-to-right) horizontal direction, may find such a difference.

3.2.4.2 Postprocessing of Motion-Encoded MRI

The StdDevs of the tissue deformation were small in each subject, demonstrating the reproducibility of the automatic tracking of the polylines. The five polylines in each muscle did not constitute independent measures.

The reproducibility of the tissue point tracking worsened in the time frames at the end of the tracking. Due to the drop of SNR with a greater number of time frames, the acquisition was limited only to the right-to-left gaze phase of the horizontal sinusoidal movement.

The polyline tracking software TagTrack works with hand drawn polylines on the motion-encoded image. To ascertain that the polylines lay on the expected tissue, advantage was taken from anatomical images and realigned the polylines if they were not on the muscles of interest or the ON. Drawing polylines on the anatomical image, and a subsequent automatic transfer to the motion-encoded image, would improve the position accuracy of the polylines.

An evident limitation of the low resolution is the inability to resolve diverse structures within EOMs, as, for example, the global and orbital EOM layers. Nevertheless, as about twenty pixels are acquired in the longitudinal direction of the muscles, this method was capable of resolving three muscle segments. The limited resolution mainly affects the interface of differently moving tissues. Since the anterior segments of the EOMs are thin, their tracking was more difficult than the middle or posterior segments. To diminish the partial volume effect in the outer layer of the EOMs, the signal was optimized by taking advantage of the specific T1 of muscles. Note that the tagline distance is not important for resolution. The tagline distance gives only the period of the phase information. The resolution of the phase information used for the tracking is limited by the scan resolution and the size of the postprocessing filter.

Although the SNR dropped at the orbital apex, the tracking of the polylines was still reliable. The whole postprocessing procedure took in average 20 min for each subject.

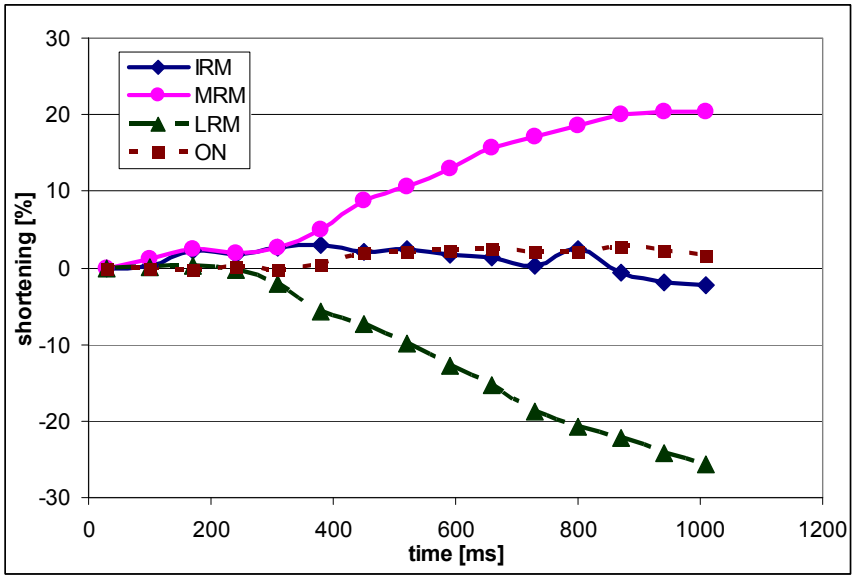

Figure 3.7: 3D CSPAMM polylines averaged strain, in function of time, for the relaxing LRM, the non-contracting ON and IRM, and the contracting MRM.

3.2.5 Limitations

The tracking algorithm of the polylines needs to be upgraded in order to sample more than three EOM segments. A possible solution to enhance the tracking quality would be to track the five polylines as a whole and not as separated entities. This should reduce the noise sensitivity of the tracking and may also reduce the acquisition time and allow a greater number of segments along the muscles to be resolved.

The drawing of each individual polyline is also time consuming and subject to positioning errors.

For 3D CSPAMM datasets, the polyline based tracking algorithm did not allow to reliably resolve the inhomogeneous deformation of the EOMs. Only the total length change cool be reliably reported (see Figure 3.7).

3.3 2D and 3D Meshes of Tracked Landmarks for CSPAMM Data

As 2D CSPAMM provided information about the inhomogeneous deformation of the two horizontal EOMs during eye movement, the quantification of the local strain along all EOMs during eye movement was aimed. However, the number of segments that could be resolved with polyline tracking was insufficient. The aim was that the image resolution would be the limiting factor of the resolution of inhomogeneous strain along the EOMs and of the orbital tissues in general. To achieve this goal, the postprocessing technique had to be improved to obtain local EOMs' strain from 2D and 3D CSPAMM images.

Therefore, the landmarks were not anymore embedded in a one dimensional (1D) structure (polyline) but instead in a 2D grid, called *mesh* (see Figure 3.8). To take into account the smoothness and continuity with which tissues deforms, a regularity constrain was imposed on the mesh on a scale smaller than the image resolution. No other prior information was used to avoid overriding the data by a model, which maybe would not able to describe pathological states.

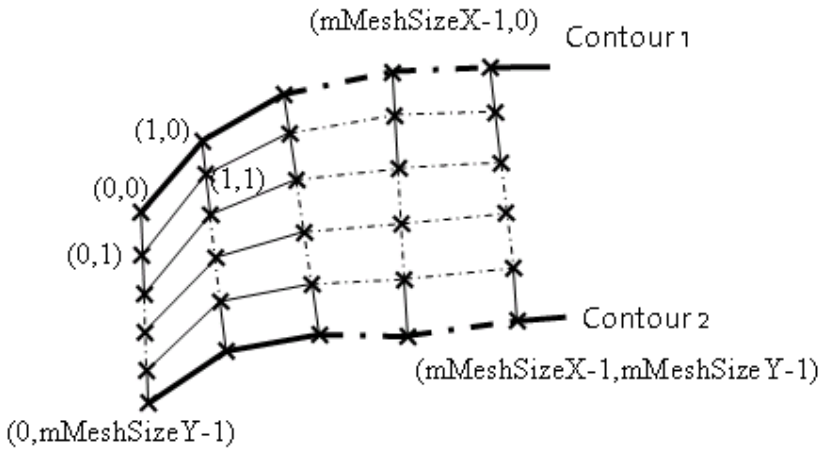

Figure 3.8: 2D mesh defined by two polylines. The coordinates of each landmark are stored in a different pointer ordered by the position of the landmark inside the mesh.

In this section, the mesh structure and implementation is presented, as well as the performance tests effected on the mesh algorithm. Its ability to extract quantitative information from 2D and 3D CSPAMM data sets was tested. The horizontal EOMs and ON deformation patterns obtained from 2D and 3D CSPAMM data were compared. Additionally the local deformations of the other EOMs were determined for 3D CSPAMM data.

3.3.1 The Mesh Concept -

Landmarks are image locations that are tracked over the time frames using the motion-encoded image information. These landmarks can be arranged more or less regularly into a geometrical structure. A mesh is defined as a (tetragonal) grid of landmark.

To be in accordance with the tissues' physiological constrains, the mesh is constrained to remain regular (no crossing of the polylines) for all time frames. So, the tracking of the landmarks can be stabilized locally and its noise sensitivity reduced. Correction algorithms for the regularity of the mesh have been implemented, so that a landmarks remains inside the space defined by its neighbors.

The 2D and 3D meshes can be used to track tissues for all data types that can be read into TagTrack; they are not limited to 3D tagging data. They consist of landmarks as the polylines (see Figure 3.9).

3.3.1.1 Implementation

Similar to polylines, the postprocessing software was based on TagTrack 1.5.6 (GyroTools Ltd., Zurich, Switzerland) integrating peak-combination HARP. It also included the 3D tracking developed by A. Rutz, et al.[Rutz, et al. 2008]

The vertices' coordinates are stored in several pointers (mVerticesX, mVerticesY, mVerticesZ) ordered as a 2D, respectively a 3D array. To define a 2D mesh, two polylines are drawn - they determine the x-direction of the mesh and its localization. The mesh sizes' settings have also to be set. The so determined numbers of mesh landmarks in each direction are interpolated along and between the two polylines.

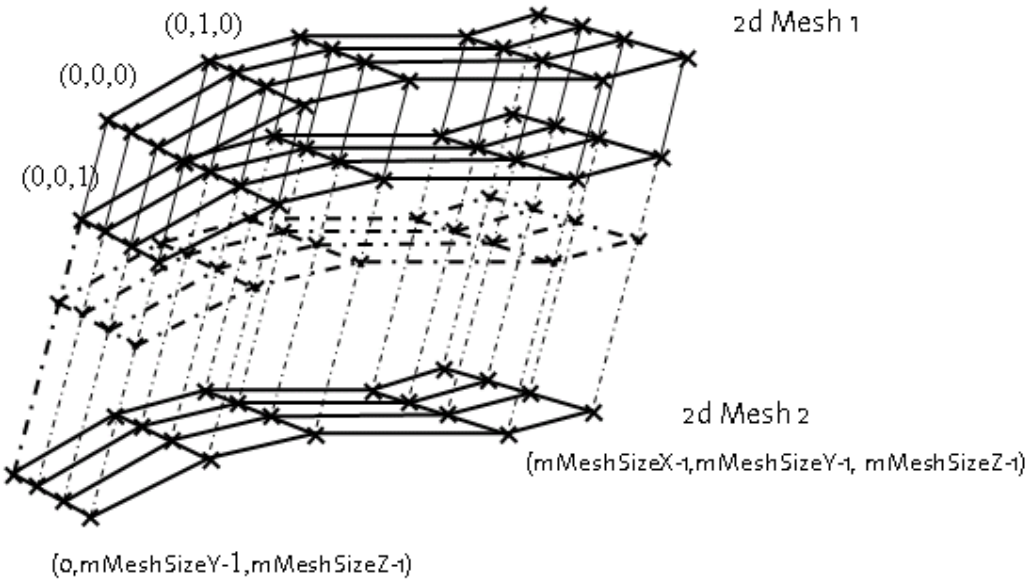

Figure 3.9: 3D Mesh defined by two 2D meshes.

The class "2Dmesh" is a subclass of the "3Dmesh" class. To create a 3D mesh, two 2D meshes have to be selected. Analogous to the creation of the 2D mesh, the interpolation function calculates the vertices between the two 2D meshes depending on the parameter MeshSizeZ set in the options interface.

The coordinates of each vertex are stored in three pointers VerticesX3D, VerticesY3D and VerticesZ3D. Each pointer is a 3D array reflecting the position of each vertex inside the volume. For example the first point of the second 2D mesh (that was used to define the 3D mesh) is stored in the 3D structure under:

VerticesX3D(0,0,mMeshSizeZ -1) = VerticesX _Mesh2(0,0)

VerticesY3D(0,0,mMeshSizeZ -1) = VerticesY _ Mesh2(0,0)

VerticesZ3D(0,0,mMeshSizeZ -1) = VerticesZ _Mesh2(0,0)

Both 2D meshes and 3D meshes can be tracked. After each step of the tracking procedure, the regularity of the mesh is checked and corrected if needed. The postprocessing software assigned the nearest equivalent tissue point of the next time frame to each tissue point, and therefore tracked each mesh vertex (landmark) independently. If inconsistent tracking of the vertices generated 2D mesh irregularities (crossing of connections), the tracking algorithm regularized the 2D mesh using the information of the neighbors of the mistracked vertices. This did not imply a loss of information, as the cells of the mesh were smaller than the filtered image resolution.

To sum-up, the tracking algorithm contained 5 steps: the drawing of two polylines for each of the EOMs. The 2D interpolation of these two polylines to form a 2Dmesh. The first tracking of the 2Dmesh over the 15 time frames, with HARP but without peak-combination, as peak-combination . The first correction of the 2Dmesh inconsistencies. The second tracking of the 2Dmesh over the 15 time frames, with HARP and peak-combination. The second correction of 2Dmesh inconsistencies.

2D and 3D mesh can be used to track tissues deformations in 3D CSPAMM data. Using 3D meshes, only the drawing procedure is modified: two pairs of polylines are needed, so that 2 more or less parallel 2D meshes can be defined. These two 2D meshes are then interpolated to create the 3D mesh. To analyze the behavior of the tracked tissues several strain functions have been implemented. They are methods of the 2D mesh, respectively 3D mesh class.

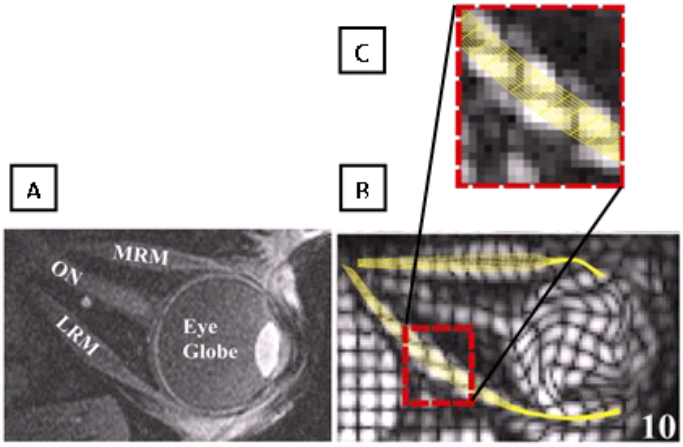

Figure 3.10: Mesh was defined on the 10th time frame with the aid of T1-weighted static MR image. (A) T1-weighted static MR image of the right orbit. (B) At the 10th time frame, the meshes (in yellow) are manually superimposed to the two horizontal EOMs. (C) Detail of the 10th time frame of Panel B showing the mesh structure: 11 segments cover the muscle width.

To calculate the local strain, the length of each of the *mMeshSizeX-1* segments along the tissues was averaged transversally to the tissue over the *mMeshSizeY-1* × *mMeshSizeZ-1* parallel connections. For calculation of the relative length change, the segment length at the first time frame (20° right gaze for right-to-left, and 20° left gaze for left-to-right eye movement, respectively) was selected as a reference. The relative length change of each segment was calculated by dividing its length at the actual time frame by its reference length. The deformation of each mMeshSizeX-1 averaged longitudinal segment was then smoothed by an averaging kernel which width corresponds to the number of segment per image voxel. Therefore, for each tissue, the data of the *mMeshSizeX-1* segments were condensed into a number of segments corresponding to the number of voxel along the tissue. Finally, the deformation over time of each segment was smoothed with a three time frames broad averaging kernel.

3.3.2 Application of Mesh Algorithm to 3D CSPAMM Postprocessing

As small study was performed to test the capabilities of the mesh algorithm on 2D and 3D CSPAMM data of the orbit during eye movement, obtained as descript in the previous Chapter.

3.3.2.1 Method

A 40 x 11 2D tetragonal mesh was defined on the whole length of the ON and of each EOM on the 10th time frame (approximately gaze straight ahead - see Figure 3.10). To ascertain that the meshes lay on the tissues, anatomical images were taken as references and realigned the meshes if needed. These meshes divided the tissues length into 40 isometric longitudinal segments, which were numbered from 1 to 40 beginning at the scleral insertion of the EOMs, respectively of the ON. A good knowledge about the orbital anatomy was needed to correctly lay the meshes.

For 2D CSPAMM data, the mesh was laid on the ON, the MRM, and the LRM. For 3D CSPAMM data, an important new feature of the processing tools allowed drawing the 2D mesh

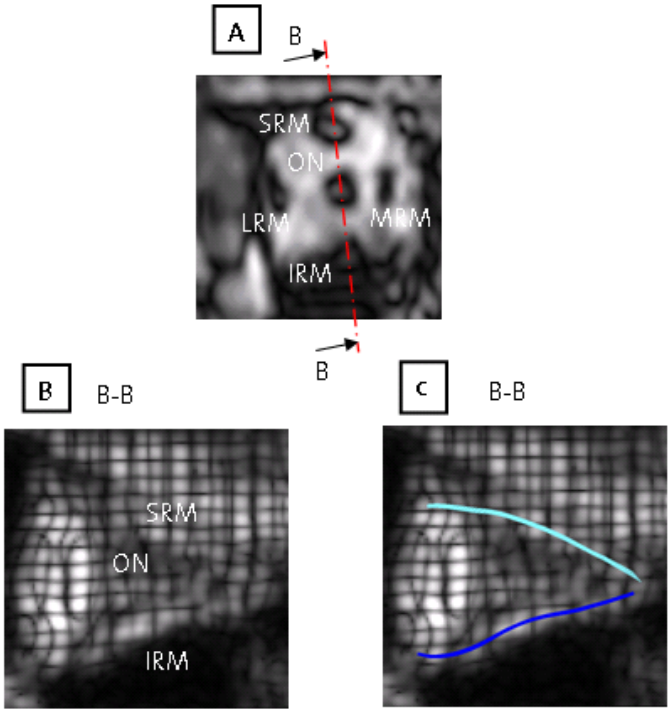

Figure 3.11: User-defined planes of a 3D CSPAMM dataset used to draw 2D meshes on the IRM and the SRM. (A) Coronal anatomy image (gaze straight ahead). The red line shows the position of the user-defined planes. (B) Selected plane to draw the meshes of the IRM and SRM (At the 10th time frame). (C) 2D meshes (in dark, respectively light blue) manually superimposed to the IRM and SMR on the selected plane of the 3D CSPAMM images.

on the other EOMs. The 2D mesh was laid on the same three muscles as for 2D datasets; and additionally, on the IRM, SOM, and SRM. The IOM could not be reliably determined due to its vicinity to the sclera and the susceptibility artifacts due to the air-tissue interface. Within the user-interface, it was possible to define any plane intersecting the 3D image volume. By selecting a convenient plane for each muscle, the 2D meshes were drawn on muscles. The plane was set to see as much as possible of the tissues. The 2D meshes on IRM and SRM were drawn in the same plane; for the SOM another plane was selected. Afterwards, the meshes were automatically tracked over the 15 time frames and enabled the quantification of the inhomogeneous deformation along the EOMs.

The deformation profile of each tissue (ON, MRM, and LRM) was calculated for 2D and 3D data. Each deformation profile based on 2D data was compared with a 3D dataset for gaze direction left-to-right (subject 1) and right-to-left (subject 2). For 3D data, the deformation profile of the other EOMs (IRM, SOM, and SRM) was calculated for both gaze directions (subject 1 and subject 2 - see Figure 3.11 and Figure 3.12).

The relative length of each segment is represented as a function of its position along the tissue, plotting the longitudinal deformation profile of the healthy muscle for a given time frame during 40° horizontal eye movement. The length of each of the 8 segments along the tissue is scaled by its length at the first time frame at 20° left gaze (black/yellow solid line, 1st time frame). The length of each segment at the first time frame was set to 1.0. The deformation of each particular segment can be traced by following the relative length of the segment.

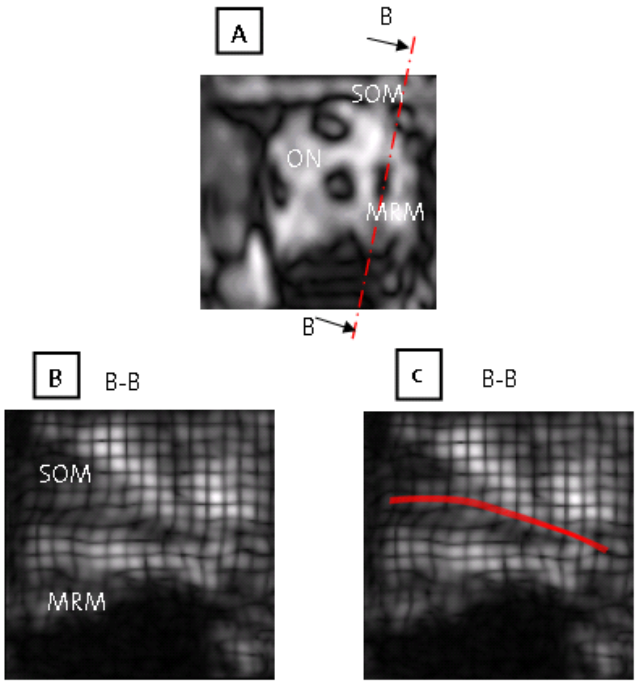

Figure 3.12: User-defined plane of a 3D CSPAMM dataset used to draw 2D meshes on the SOM. (A) Coronal anatomy image (gaze straight ahead). The red line shows the position of the user-defined planes. (B) Selected plane to draw the SOM (At the 10th time frame). (C) 2D mesh (in red) manually superimposed to the SOM on the selected plane of the 3D CSPAMM images.

3.3.2.2 Results

The deformation profiles of LRM, MRM and ON based on 3D data showed similar results as for 2D data for left-to-right direction and right-to-left. For both datasets, the LRM and the MRM showed a heterogeneous local deformation and for all time frames, the maximal deformation amplitude was closer to the orbital apex than to the scleral insertion of the muscles. The location of the maximal tissue deformation was in accordance between the results based on 2D data and 3D data. But, the comparison of the maximal local deformation showed a difference between 2-6% between the 2D and 3D data.

The ON deformations were smaller than the deformation of the LRM and MRM segments. The profile of subject1 as well as subject2 showed a smaller deformation for 2D data. In both gaze directions (2D and 3D data); the deformation of the ON segments was more homogenous than the deformation of the LRM and MRM. But, the ON relative segment lengths did not reach a minimum at the 8th or 9th time frame for both eye movement directions as in [Piccirelli, et al. 2009a]. This is expected, considered that 2D data project a 3D deformation on the image plane.

The 3D tagging dataset allowed recognizing the IRM, SOM and SRM. By choosing a convenient plane of the 3D data volume, the whole IRM, SOM and SRM could be tracked. The deformation profile is reported for both gaze directions. The deformation for IRM, SRM and SOM were very small compared to the horizontal EOMs; but the profile also showed a smaller deformation as for ON based on 3D data. The deformation increased with time for all three muscles: except for the IRM profile of subject2 (right-to-left), the blue time frames showed the largest deformations (see Figure 3.13).

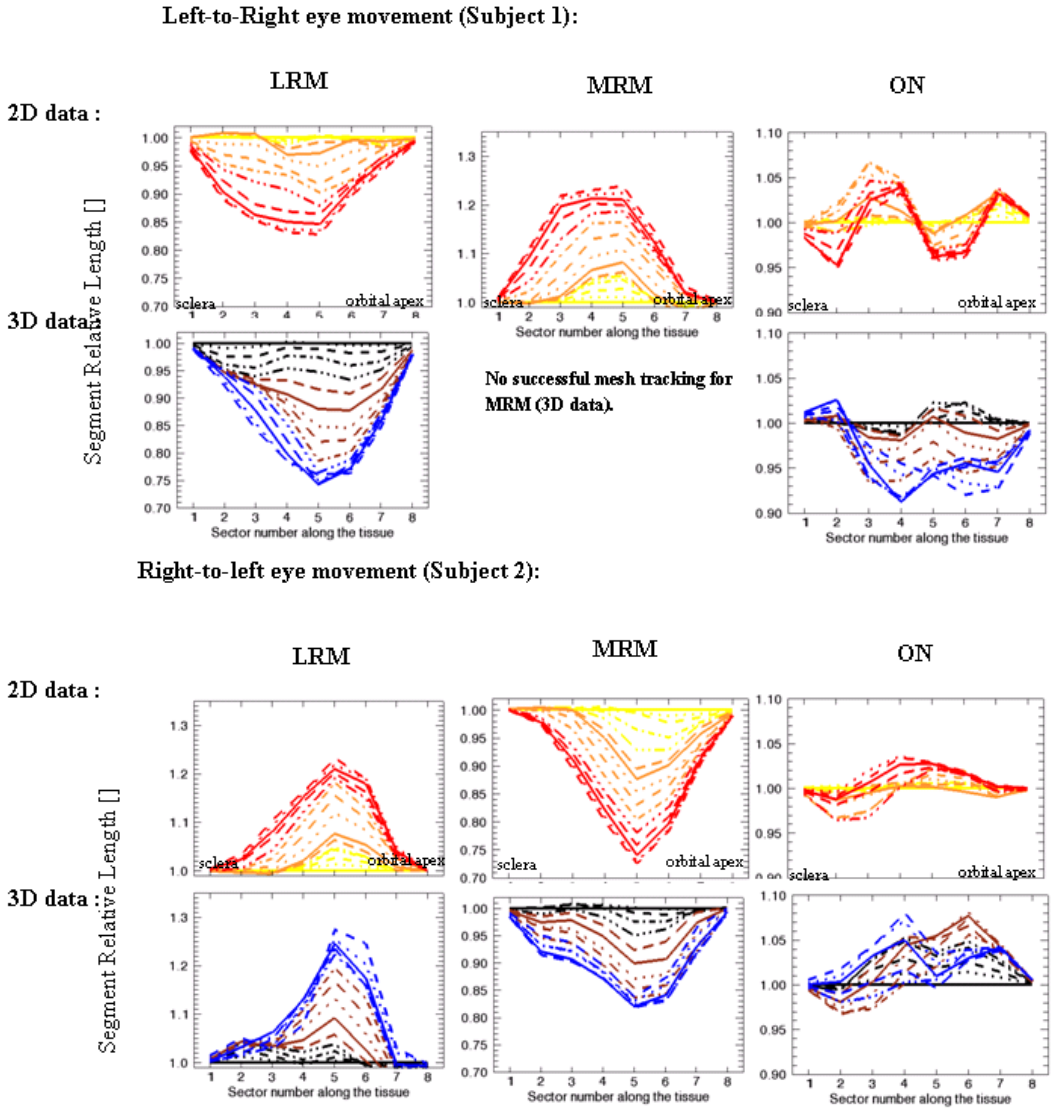

Figure 3.13: Deformation profile of the LRM, MRM, and ON for right-to-left eye movement (of the right eye of subject 1 resp. 2) based on 2D data and 3D data. X-axis: the three muscles are partitioned longitudinally into 8 segments. Segment 1 is located on the scleral insertion, segment 8 at the orbital apex. Y-axis: The segment length relative to its length at the first time frame. Each profile corresponds to one of the fifteen time frames. The first five time frames were drawn in black, respectively yellow, the middle five in brown, respectively orange and the last five in blue, respectively red. Segment 5 shows the greatest deformation of all segments, for both EOMs.

By comparing the profiles of one gaze direction with the other, it seemed that the local maximum in one direction became a local minimum deformation in the other eye movement direction. Even though, the deformations were very small, the blue time frames of all three EOMs showed this behavior (see Figure 3.14).

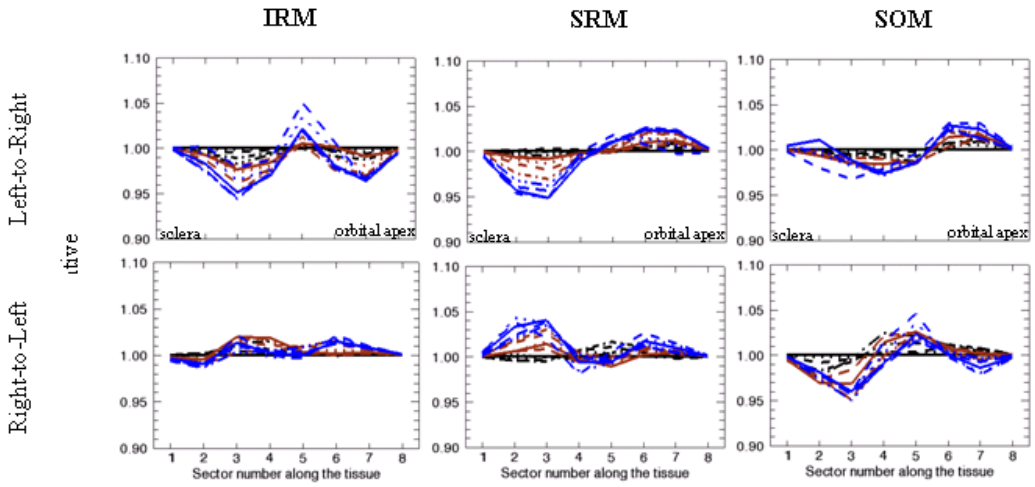

Figure 3.14: Deformation profiles for IRM, SOM and SRM obtained from 3D data, during right eye movements from 20° left to 20° right (subject 1) and from 20° right to 20° left (subject 2). X-axis: the three muscles are partitioned longitudinally into 8 segments. Y-axis: The segment length relative to its length at the first time frame. Each profile corresponds to one of the fifteen time frames. The first five time frames are drawn in black, the middle five in brown, and the last five in blue. The line type has a period of 6 time frames.

3.3.2.3 Discussion

The mesh algorithm allowed to resolve the local deformation along the EOMs and ON at a scale similar to the image resolution. 2D meshes were successfully used to track the tissues' deformation on 2D and 3D CSPAMM data. Optimized scan parameters and postprocessing software allowed quantifying the local deformation of all EOMs (except IOM) obtained from 3D CSPAMM during eye movements. Nevertheless, the tracking stability on the lower SNR 3D CSPAMM data may benefit from 3D meshes. Due to the anatomical arrangement of the muscles in the orbit, a 3D data and postprocessing may be suited to describe the real EOMs deformation during eye movement.

The local deformations calculated for the LRM and MRM matched the results based on 2D data within one StdDev. The deformation profile based on 2D and 3D data showed common characteristics such as the inhomogeneous deformation for LRM and MRM or the position of the deformation maxima. But for 2D data, the profile of subject1 as well as subject2 showed smaller deformations. The decrease of the measurable deformation in 2D compared to 3D is expected, considered the larger slice thickness of 2D data (4 mm) compared to the 3 mm slice thickness of the 3D data, and that 2D data project a 3D deformation on the image plane.

The 3D postprocessing tools allowed identifying the LRM, MRM, IRM, SRM and SOM by extracted the corresponding plane of the 3D tagging volume. The quantification of the deformation could be determined by tracking a 2D mesh for each muscle. The deformation profiles could be calculated, but the tracking in 3D data was more sensitive to the correct identification of the muscles than with 2D data, due to the low SNR of the data. It seemed that the 2D mesh correction algorithms were not sufficient for 3D data. An extension to a 3D mesh with a corresponding correction algorithm will improve the tracking quality of 3D data. The correct identification of the muscles on the tagging images may not be needed, if it is possible to define the mesh directly on the anatomical images and to track directly the previous defined mesh on the tagging images afterwards.

The scan time for 3D measurements was doubled compared to 2D (4.5min vs. 9 min), but the 3D technique provided information about the other muscles (IRM, SRM; and SOM). The 3D technique could show that those EOMs nearly did not deform during horizontal eye movement. By comparing the subjects, an opposite behavior between right-to-left and left-to-right direction was observed. The opposite behaviors of IRM, SRM and SOM between the two gaze directions for healthy subjects were not statistically significant due to the limited number of subjects.

The 3D motion-encoded MRI offers many advantages. It provides new insights into eye movement for all EOMs. Further studies will outline, if the advantages of the 3D technique justifies the longer acquisition time. This study has already shown that the tracking of IRM, SOM and SRM was possible. Clearly, an improvement of the tracking quality is essential to investigate also pathological subjects.

3.3.3 The Mesh Visualization

To facilitate the visualization of the deformation pattern along the orbital tissues, a software tool, called *meshcolor*, has been developed to color encode the stitches of the mesh as function of their strain.

3.3.3.1 Method

As descript above , the strain along a tissue can be tracked using a mesh. The deformation of the muscle or nerve could be more easily observed from a color coding of the local strain. The first time frame served as reference for the strain calculation, so the color of the mesh at the time frame 1 is always green. The color map is defined in such a way that for an increase of the border or the area the color will change to red and otherwise change to blue.

Every mesh cell has a unique bottom border line in X direction and a unique left border line in Y direction. The square area is defined proportional to their product, so three different color maps corresponding to these three parameters were made (see Figure 3.15).

In order to analyze the motion of orbital tissues, strain color map of the EOMs and ON were developed (see Figure 3.16).

3.3.3.2 Results and Discussion

An example of the color encoding of the mesh deformation over time is presented. The mesh covered the MRM, ON, LRM and tracked their deformation during eye movement from right to left. The meshes can track deformations in any of their dimension. Here under, the length, the thickness, and the volume (area) change of the three tissues are compared.

The mesh strain coloration gives an intuitive representation of the underlying tissue deformation. The deformation of the mesh along its length, or along its thickness, or even its cells' area can be color-encoded. The deformation obtained here are quite consistent to each other’s: The LRM elongates, get thinner, and its volume does not change much. The MRM do just the opposite.

Nevertheless, the actual motion resolution should be kept in mind, especially for the thickness changes. The mesh has to be broader than a pixel to be able to resolve truly independent movements. If the mesh is smaller than a pixel, it will underestimate the deformation. However, the data presented here have not been averaged on the resolution scale to be able to observe at which location the mesh tracking is mostly disturbed by noise and images artifacts (see Figure 3.17 to Figure 3.19).

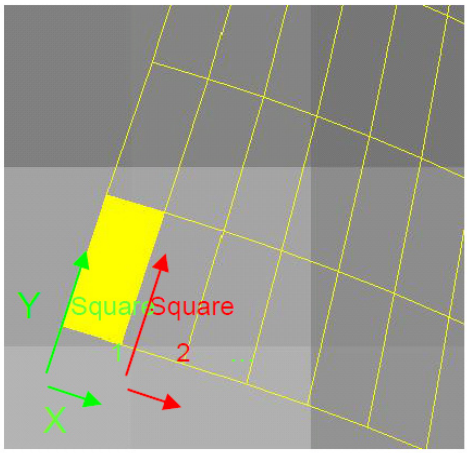

Figure 3.15: SegmentX is defined as a square's bottom border line along X (green arrow X). SquareArea: is defined as the area of the square among four mesh vertices. SegmentY is defined as a square's left border line along Y (green arrow Y)

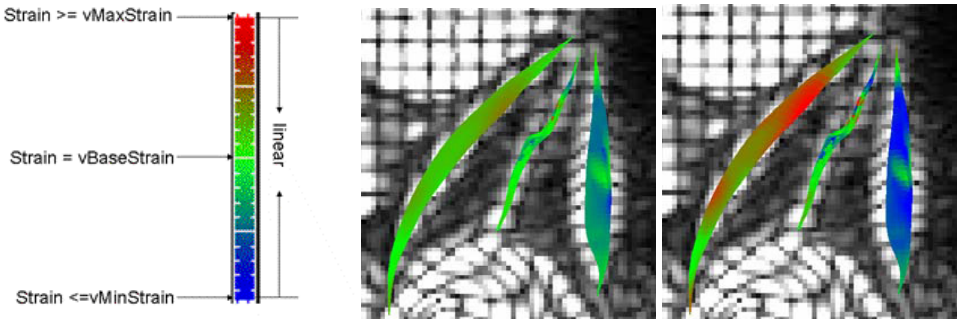

Figure 3.16: Color bar for the meshcolor. Setting the parameters vMaxStrain and vMinStrain, the color coding can be changed. (Middle Panel) vMaxStrain = 2.0, vMinStrain = 0.5. (Right Panel) vMaxStrain = 1.5, vMinStrain = 0.7.

3.4 Conclusion

In this Chapter, it was showed that the motion encoded by the CSPAMM images of the orbit presented in Chapter 2 can be automatically tracked and that the tissues deformation can be quantified. With 1D polylines of landmarks the quantification of the inhomogeneous deformation along the EOMs was possible for the first time. Using multidimensional structures for landmarks, called mesh, the differentiation of the local strain was possible down to the scale of the image resolution. The mesh algorithm allowed the quantification of the strain along all four rectus muscles and along the SOM. The multidimensionality of the mesh allows tracking not only longitudinal but also transversal deformations. The meshes are easier to draw than polylines and give more reliable results. The mesh based algorithm presented below is also applicable for the motion quantification from CDENSE and Q-Flow data.

Using the above mentioned postprocessing software, detailed insights into how the horizontal EOMs transformed smooth pursuit commands into eye movements. In healthy subjects, the longitudinal muscle deformation was heterogeneous. Furthermore, the shape of the EOM deformation profiles remained similar over the entire 40° movement range. For example, the

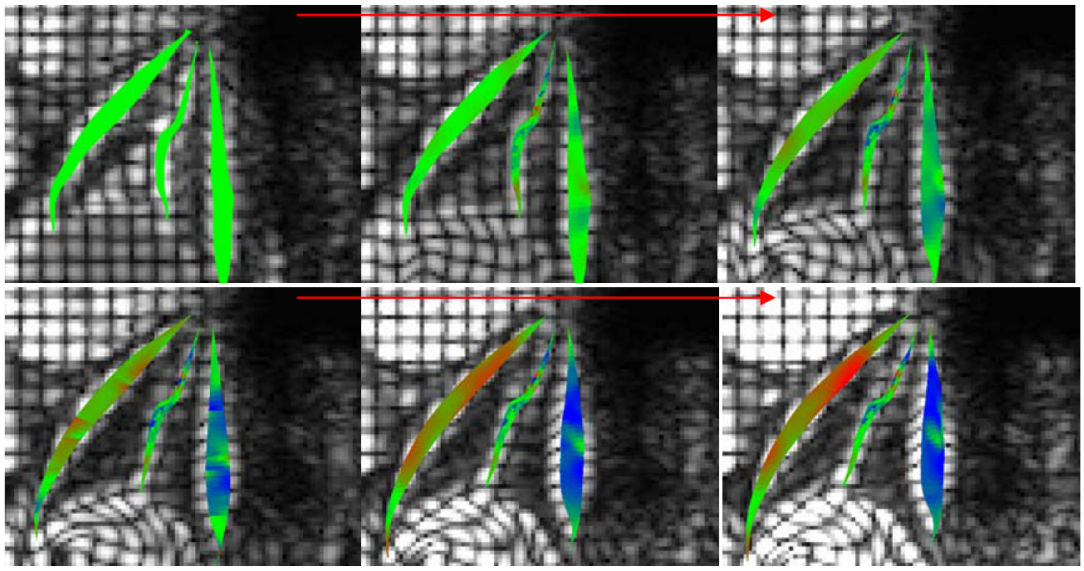

Figure 3.17: Color encoding of the mesh deformation along the tissues, i.e. in the x-direction. Contraction (shortening) during the right-to-left gaze is coded in blue, and elongation in red. The first time frame is used for the reference lengths (uniform green color). The time frames 1, 5, 8, 10, 12, and 15 out of 15 are depicted (movement range ±20°).

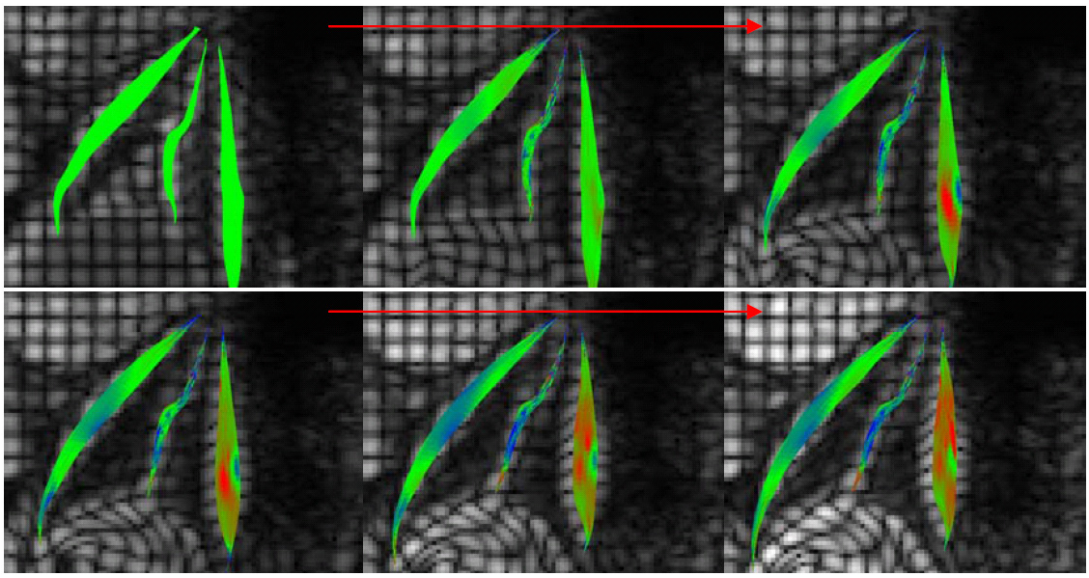

Figure 3.18: Color encoding of the mesh thickness change, i.e. strain in the y-direction transversal to the tissues. Thickness diminution during the right-to-left gaze is coded in blue, and thickening in red. The first time frame is used for the reference lengths (uniform green color). The time frames 1, 5, 8, 10, 12, and 15 out of 15 are depicted (movement range ±20°). The LRM thickness diminishes slightly during elongation. The MRM swell during contraction. The mesh on the ON is too thin to give meaningful information, as it is thinner than the image resolution.

extent of deformation at the 8th time frame was nearly half of the deformation at the 15th time frame. Considering the intramuscular coordinate system, the location of the maximal deformation did not shift during eye movement.

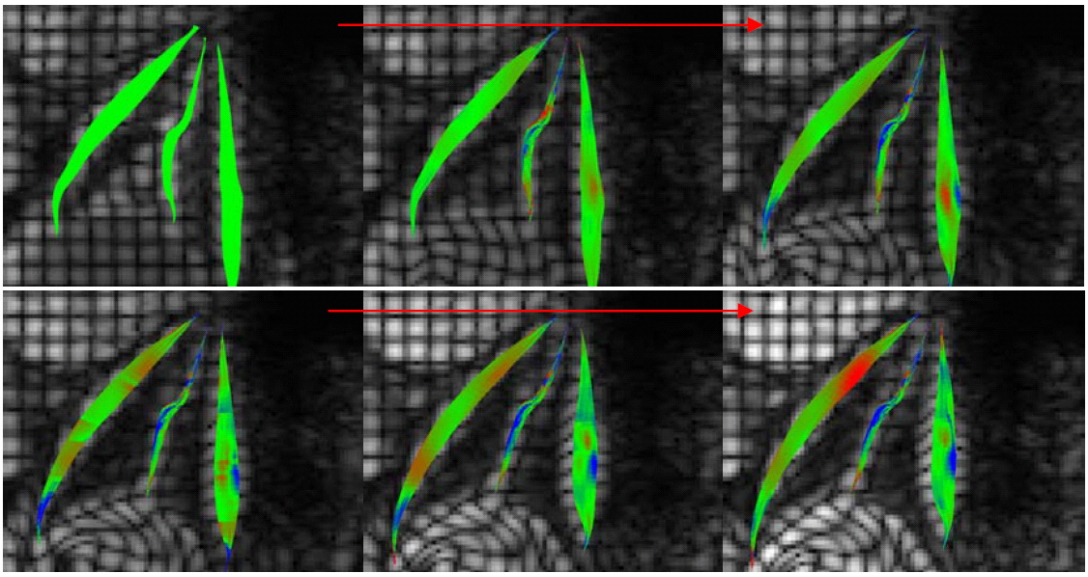

Figure 3.19: Color encoding of the mesh cells' area change during right-to-left eye movements. Tissue volume decrease is coded in blue, and increase in red. The first time frame areas are used as reference (uniform green color). The time frames 1, 5, 8, 10, 12, and 15 out of 15 are depicted (movement range ±20°). The EOMs mesh cells' areas were mostly constant. Only the LRM's center part slightly swelled.

The LRM deformed less than the MRM, which is expected because the LRM is longer than the MRM. The peak deformation correlated with the amplitude of the eye movement, but the deformation profiles remained similarly shaped over the entire movement range. Therefore, the profile shapes describe EOM relevant properties. On the other hand, the amplitude of the deformation was dependent on the eye movement range.

Chapter 4: Application to the Extraocular Muscles of Duane-Syndrome Patients

In this chapter, the quantification of the local deformation along EOMs obtained by postprocessing CSPAMM data with meshes gives insight into the mechanisms underlying the Duane's syndrome type I (DSTI). The DSTI is a pathology affecting the neuronal system controlling the EOMs. This Chapter has been published in [Piccirelli, et al. 2009a].

4.1 Introduction

To better understand the etiologies of ocular misalignment, the mechanics of the human orbit and especially the EOMs have been extensively studied. The anatomy of the complex system of orbital connective tissues was described using MRI coronal sections.[Ettl, et al. 1998] Different eye positions were imaged using CT,[Simonsz, et al. 1985] X-Ray,[Miller and Robins 1987] and MRI.[Demer, et al. 2002] Miller et al. showed that the path of the rectus muscles in the orbit changes depending on their contraction state.[Miller 1989] Other MRI studies documented EOM atrophy as a consequence of cranial nerve palsies.[Horton, et al. 1990; Demer, et al. 2006] Also, EOM tissue borders were followed with MRI.[Abramoff, et al. 2000] Gold beads were implanted inside monkey orbits to demonstrate orbital soft tissue deformation.[Miller, et al. 2006] All above-mentioned studies used static gaze positions for their analysis.

To further improve the understanding of EOM properties, force measurements targeted effective EOM activity in alert monkeys.[Miller and Robins 1992; Miller, et al. 2002] However, the EOMs have been largely inaccessible. Two years ago, tagging of the orbit[Piccirelli, et al. 2007] aimed to investigate noninvasively the inhomogeneous local deformation along the EOM length during eye movement.

The aim of this study is to present baseline data on horizontal EOM segments in normal subjects. Moreover, the kinetics of the local physiologic contraction/elongation of the MRM and the LRM for left-to-right movement will be compared with right-to-left movement. To demonstrate that tagging is able to differentiate normal from pathologic movement, the healthy physiological patterns were compared with those of two DSTI patients. To serve this need, the postprocessing technique was improved to increase the number of segments that could be differentiated along the EOMs. Landmark chains (polylines) along the EOMs were replaced by a two-dimensional tetragonal landmark grid (called mesh) covering the entire EOM length. Landmarks are dimensionless locations in the image, tracked through the 15 time frames. They are needed for tracking algorithms to work.

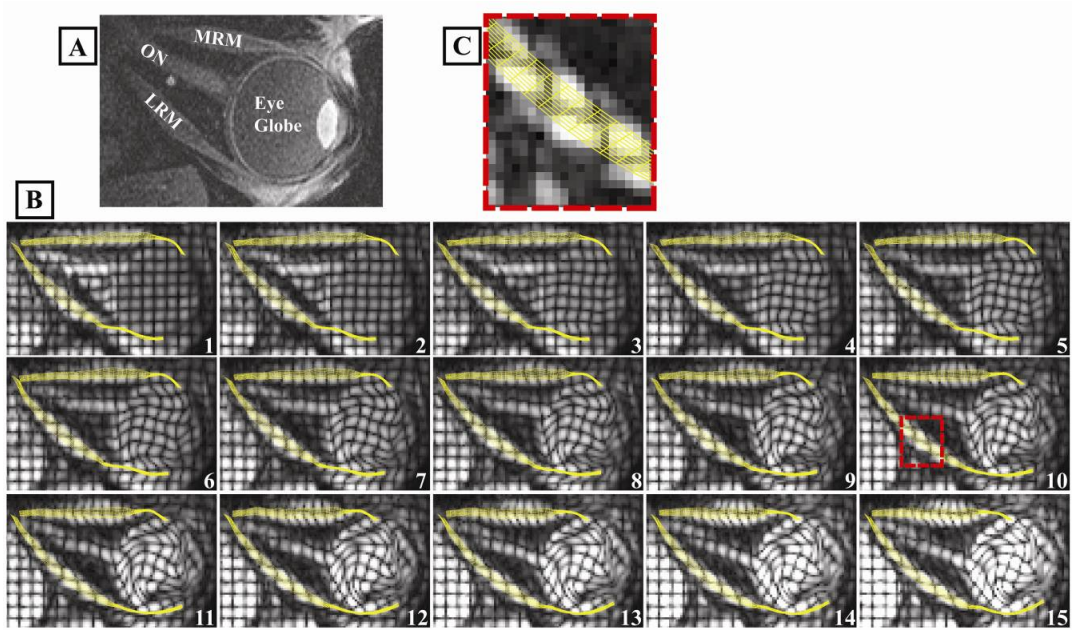

Figure 4.1: (A) T1-weighted static MR image of the right orbit. The MRM, the ON, and the LRM are depicted in one image plane. (B) The 15 time frames of the CSPAMM MRI of the orbit during right-to-left eye movement. The temporal resolution was 70ms. The magnetization (and therefore the signal) is modulated to create a tagging pattern that is bound with the tissues. The deformation of the tagging pattern serves to depict the differential movements within homogeneous tissues. At the 10th time frame, the meshes (in yellow) are manually superimposed to the two horizontal EOMs. Consequently, the meshes overlaid to the MRM and LRM are automatically tracked and enable the quantification of the inhomogeneous deformation along the EOMs. (C) Detail of the 10th time frame of Panel B showing the mesh structure: 11 segments cover the muscle width.

4.2 Materials and Methods

4.2.1 Subjects and Setup

The study was conducted according to the tenets of the Declaration of Helsinki and approved by the ethics committee of the Health Department of the Canton of Zurich, Switzerland. Each subject agreed to participate after the scientific value and possible risks of the study were explained. Eleven healthy right eyes (five women and six men; mean age: 32 years; range: 22 to 53 years of age) were imaged. The left eye of two of the eleven subjects, (a 25 year-old-woman and a 22 year-old-man) diagnosed with DSTI in the left eye, were also imaged. The DSTI patients showed the clinically classical abduction deficit and globe retraction in adduction. This pathology was chosen to investigate the local behavior of the LRM during adduction, when an elongation over the entire length of this muscle is expected. The healthy subjects of the control group were recruited by advertisement, the two patients were invited. Visual acuity of all subjects was sufficient to track the visual stimulus: a horizontal sinusoidally oscillating white square on a black background (target size = 0.4°) with amplitude of ±20° and a period of 2s (corresponding to a maximal angular eye velocity of 63°/s). The stimulus induced smooth pursuit eye movements. For the presentation of the visual stimulus, a computer, projector, projection screen, and the software "Presentation" (Neurobehavioral Systems Inc., Albany CA, USA) were used. A mirror allowed the subjects to gaze out of the bore to the projection screen. Similar setup and stimulus paradigms

were used as described in Piccirelli, et al.[Piccirelli, et al. 2007] A receive-only surface coil of 47mm diameter was placed on one eye like a monocle, so that the subject could see the target through it. Foam pads immobilized subject's head.

4.2.2 MRI Sequence

Axial CSPAMM tagging images[Fischer, et al. 1993] were acquired with a gradient echo sequence acquired on a 1.5T system (Achieva 1.5T; Philips Healthcare, Best, The Netherlands - see Figure 4.1). The tagging image plane was defined on a semicoronal scan by straight ahead gaze, and included the orbital apex as well as the scleral insertions of the horizontal EOMs. The 40° right-to-left, and left-to-right eye movements, respectively were split into fifteen time frames of 12ms duration, separated by 58ms, resulting in an acquisition of 15x70=1050ms. The remaining 950ms of the 2s periodic eye movement served for signal recovery. Therefore, the two movement directions were acquired separately. The period of the signal modulation is called tagline distance. In this study, it was set to 2.5mm. To shorten the imaging time, the modulation is applied at first in one direction and then in the other direction, producing two datasets with perpendicular taglines.[Rutz 2008] These two datasets are then multiplied to form the tagging grid. A state of the art introduction to tagging is given in the PhD Thesis of Dr. A. Rutz.[Rutz 2008] Other parameters were identical to those described previously[Piccirelli, et al. 2007]: FOV 140 × 140mm^2, scan resolution 1.2 × 1.2 × 4.0mm^3, number of signal averages 8, reconstruction matrix 256 × 256. The use of an EPI factor of 5 shortened the acquisition time to 4.5min. The mesh vertices were tracked through the 15 time frames.

4.2.3 Postprocessing

The new postprocessing technique corrects potential polyline crossing (see the animated Figure 2 in [Piccirelli, et al. 2007] - or Figure 3.2). The postprocessing software assigns the nearest equivalent tissue point of the next time frame to each tissue point, and therefore tracks each mesh vertex (landmark) independently.[Piccirelli, et al. 2007] If inconsistent tracking of the vertices generated mesh irregularities (crossing of connections), the tracking algorithm regularized the mesh using the information of the neighbors of the mistracked vertices. This does not imply a loss of information, as the cells of the mesh were smaller than the filtered image resolution.[Piccirelli, et al. 2007]

The 41x11 two-dimensional tetragonal meshes were manually drawn on the whole length of the ON and of each EOM on the 10th time frame (approximately gaze straight ahead, see Figure 4.1). To ascertain that the meshes lay on the tissues, anatomical images were taken as references and realigned the meshes if needed. These meshes divided the tissues length into 40 isometric segments, which were numbered from 1 to 40 beginning at the scleral insertion of the EOMs, respectively of the ON. A good knowledge about the orbital anatomy is needed to be able to lay the meshes on the correct tissues; nevertheless, no further training is needed.

For each EOM, the consistency of the mesh lengths between the two datasets was checked. The length of the two horizontal rectus muscles should be equal at the end of the left-to-right eye movement compared to the beginning of the right-to-left movement. Due to possible head movement between two consecutive scans, the length of the EOM lying in the image plane can slightly vary. The limitation of this difference to less than 10% was attempted. If not achieved, the dataset was rejected. As a further consistency check, the length of the LRM mesh had to exceed the length of the MRM mesh. This was the case for all datasets (see Table 1).

Table 5.1

EOM Mesh Lengths of each Subject at the First and Last Time Frame for Both Movement Directions

Subject	Eye	Ocular movement direction	Length of the LRM [mm]		Length of the MRM [mm]	
			20° left gaze	20° right gaze	20° left gaze	20° right gaze
Subject 1	Right eye	Left-to-right	49.3	41.0	36.4	43.2
		Right-to-left	47.4	41.0	36.1	43.8
Subject 2	Right eye	Left-to-right	50.3	40.9	35.9	41.7
		Right-to-left	47.6	39.1	35.0	43.7
Subject 3	Right eye	Left-to-right	50.0	42.5	38.0	44.6
		Right-to-left	51.9	44.5	41.2	48.1
Subject 4	Right eye	Left-to-right	42.2	34.6	34.0	39.8
		Right-to-left	45.6	37.9	34.4	42.5
Subject 5	Right eye	Left-to-right	43.2	36.5	31.8	39.6
		Right-to-left	45.1	37.4	32.0	39.1
Subject 6	Right eye	Left-to-right	43.7	38.0	32.8	36.7
		Right-to-left	47.3	39.7	34.2	39.8
Subject 7	Right eye	Left-to-right	48.3	41.1	29.3	34.4
		Right-to-left	47.2	41.0	31.7	35.2
Subject 8	Right eye	Left-to-right	38.1[(1)]	32.8[(1)]	28.2	34.0
		Right-to-left	43.6	39.0	31.2	36.0
Subject 9	Right eye	Left-to-right	43.6	35.9	26.6	32.9
		Right-to-left	42.0	32.3	29.0	35.1
Subject 10	Right eye	Left-to-right	50.6	43.8	24.3	27.6
		Right-to-left	52.0	45.3	26.2	30.1
Subject 11	Right eye	Left-to-right	46.5	38.9	36.0	41.2
		Right-to-left	[(2)]	[(2)]	[(2)]	[(2)]
Patient 1	Left eye	Left-to-right	37.9	39.9	38.4	35.8
		Right-to-left	39.1	40.7	38.9	36.2
Patient 2	Left eye	Left-to-right	38.3	40.9	39.5	35.2
		Right-to-left	38.2	40.4	38.5	34.4

[(1)] This subject's data was excluded from further analysis as the anterior part of the LRM was not in the image plane.

[(2)] The subject's eye movements were not accurate enough. Consequently tracking of the EOMs could not be performed with sufficient accuracy.

For each subject, the lengths of the EOM meshes in mm are listed separately at the beginning and at the end of the left-to-right movement and of the right-to-left movement.

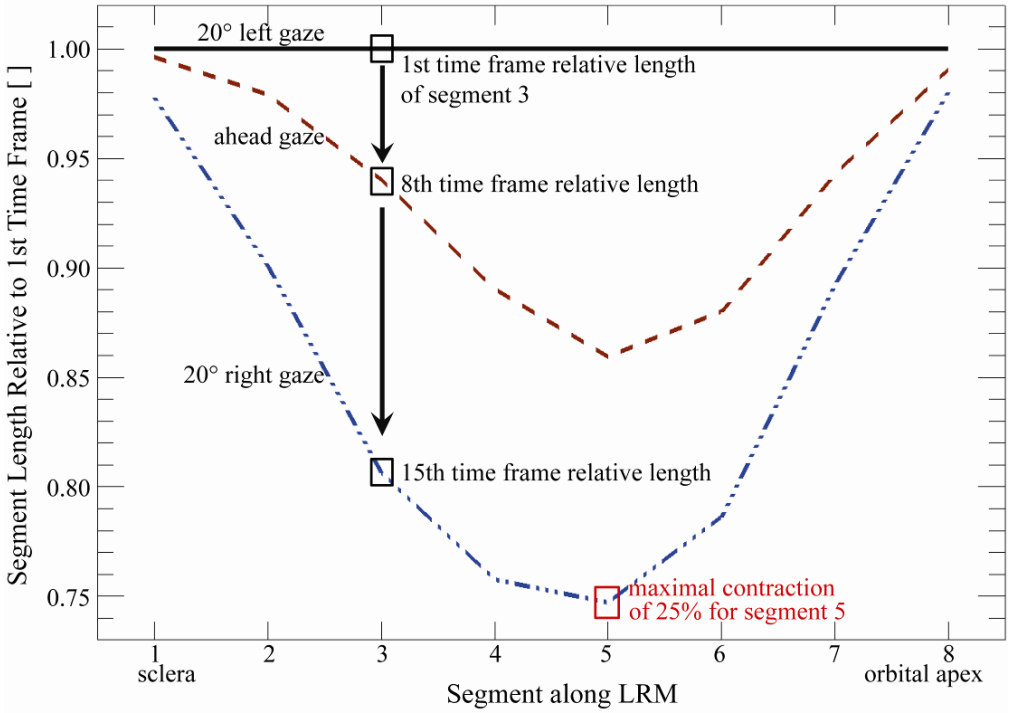

Figure 4.2: Contraction profile of the right eye's LRM of subject #9, depicting a dynamic representation of an EOM changing from elongation to shortening. X-axis: segment #1 is located on the scleral insertion, segment #8 at the orbital apex. Y-axis: The length of each segment at the first time frame is defined as 1.0. Black solid line: the 1st time frame corresponds to 20° left gaze. Trivially, the relative length of each segment is equal to 1.00 at the first time frame, as shown for segment #3 (black box on the black line). Brown dashed line: the 8th time frame corresponds approximately to gaze straight ahead. The change of gaze induced a shortening of segment #3 (top vertical arrow pointing down). Blue dash-dot line: the 15th time frame corresponds to 20° right gaze. The further contraction of the LRM induced an additional shortening of segment #3 (lower vertical arrow pointing down to lowest black box). Segment #5 showed the greatest shortening of all LRM segments, its length at the 15th time frame was 75% of its length at the 1st time frame. Therefore, the greatest local contraction of the LRM was 25%.

The postprocessing software is based on TagTrack 1.5.6 (GyroTools Ltd., Zurich, Switzerland) integrating HARP[Osman, et al. 1999] with peak-combination.[Ryf, et al. 2004b] A circular band pass filter was applied to extract the harmonic peak in Fourier space. The diameter of the filter corresponded to 2.3 image pixels.

4.2.4 Evaluation of the Meshes

For each of the 13 imaged eyes, the length of each of the 40 segments of the EOMs and ON was averaged transversally to the tissue over the 11 parallel connections. For calculation of the relative length change, the segment length at the first time frame (20° right gaze for right-to-left, and 20° left gaze for left-to-right eye movement, respectively) was selected as a reference. The relative length change of each segment was calculated by dividing its length at the actual time frame by its reference length (see Figure 4.2). The deformations of the 40 segments were then smoothed by a 5 segment broad averaging kernel. Therefore, the data of the 40 segments were condensed into eight independent segments for each EOM. These eight segments take the limited imaging and postprocessing resolution into account. Thus, the deformations of these eight segments are independent from each other. Finally, the deformation over time of each segment was smoothed

with a three time frames broad averaging kernel. The relative length of each segment is represented as a function of its position along the LRM, plotting the longitudinal deformation *profile* of the muscle for a given time frame.

The deformation profiles of each tissue for each gaze direction were averaged for the eleven healthy right eyes. For each segment, the StdDev among the healthy eyes was calculated.

4.3 Results

A representative contraction profile of a healthy right LRM (Subject #9) during 40° horizontal eye movement is shown in Figure 4.2. The length of each of the 8 segments along the LRM is scaled by its length at the first time frame at 20° left gaze (black solid line, 1st time frame). The length of each segment at the first time frame was set to 1.0. The deformation of each particular segment can be traced by following the relative length of the segment (as an example, the vertical arrows show the deformation of segment 3). For the left-to-right abducting movement, the segment with the greatest contraction was segment 5, showing a 25% shortening. The anterior half of the EOMs contracted less than the posterior half for the 40° movement range. The shape of deformation profile at the 8th time frame (gaze straight ahead) was similar to the shape of the deformation at the 15th time frame (right gaze).

In healthy subjects, the local deformation along the horizontal EOMs was heterogeneous. Figure 4.3 summarizes the deformation profiles of all eleven subjects' healthy right eyes for all 15 time frames. The anterior half of the EOMs deformed less than the posterior half, in accordance with the results of Miller.[Miller 1989] For all time frames, the maximal deformation amplitude was closer to the orbital apex than to the scleral insertion of the muscles. All deformation maxima were situated at approximately 2/3 of the muscle lengths from the scleral insertions. For the right eye left-to-right movement (abduction), the maximal local contraction of the LRM was 22%, while the MRM elongated locally up to 30%. For movements from right-to-left (adduction), the maximal local elongation of the LRM was 26%, while the MRM contracted locally by 26%. The maximal local deformations of the LRM (contraction 22%, elongation 26%) were smaller than the maximal local deformations of the MRM (contraction 26%, elongation 30%). This result is expected as the LRM is longer than the MRM. Nevertheless, the deformation kinetics was almost homogeneous: nearly no change of profile shape was observed during the eye movement. Furthermore, for each EOM, the difference between abduction and adduction deformation profiles is hardly striking.

The ON deformations were roughly ten times smaller than the deformation of the EOM segments (Panels A.3 and A.6 of Figure 4.3). The deformations of the ON segments were also more homogenous than the deformation of the EOMs. The ON relative segment lengths reached a minimum at the 8th or 9th time frame for both eye movement directions, corresponding approximately to gaze straight ahead.

Panel B of Figure 4.3 shows the corresponding StdDevs among the 11 subjects. Each curve corresponds to a time frame. The StdDevs increased with time, but stayed below 8% of the normalized segment lengths. The larger StdDevs of the LRM segments of the (slimmer) anterior half compared to the (thicker) posterior half were due to (in plane) partial volume effects that appeared at the interface of tissues with different movements. The average StdDev at the 15th time frame of the segments 10 to 30 was around 0.06. This corresponded to a mean StdDev increase of 0.06 / 15 = 0.4% per time frame. If the tissue deformations of all subjects were identical (no biological variation), the average tracking error per time frame could be estimated to be 0.4% of the segment length at that time frame.

Subsequently, the deformations of two DSTI horizontal EOMs were compared to the healthy group. Some segments of the DSTI EOMs deformed inversely to the healthy EOMs (see Figure 4.4). Patients' data outside the (4 StdDevs broad) error bars interval differed significantly from

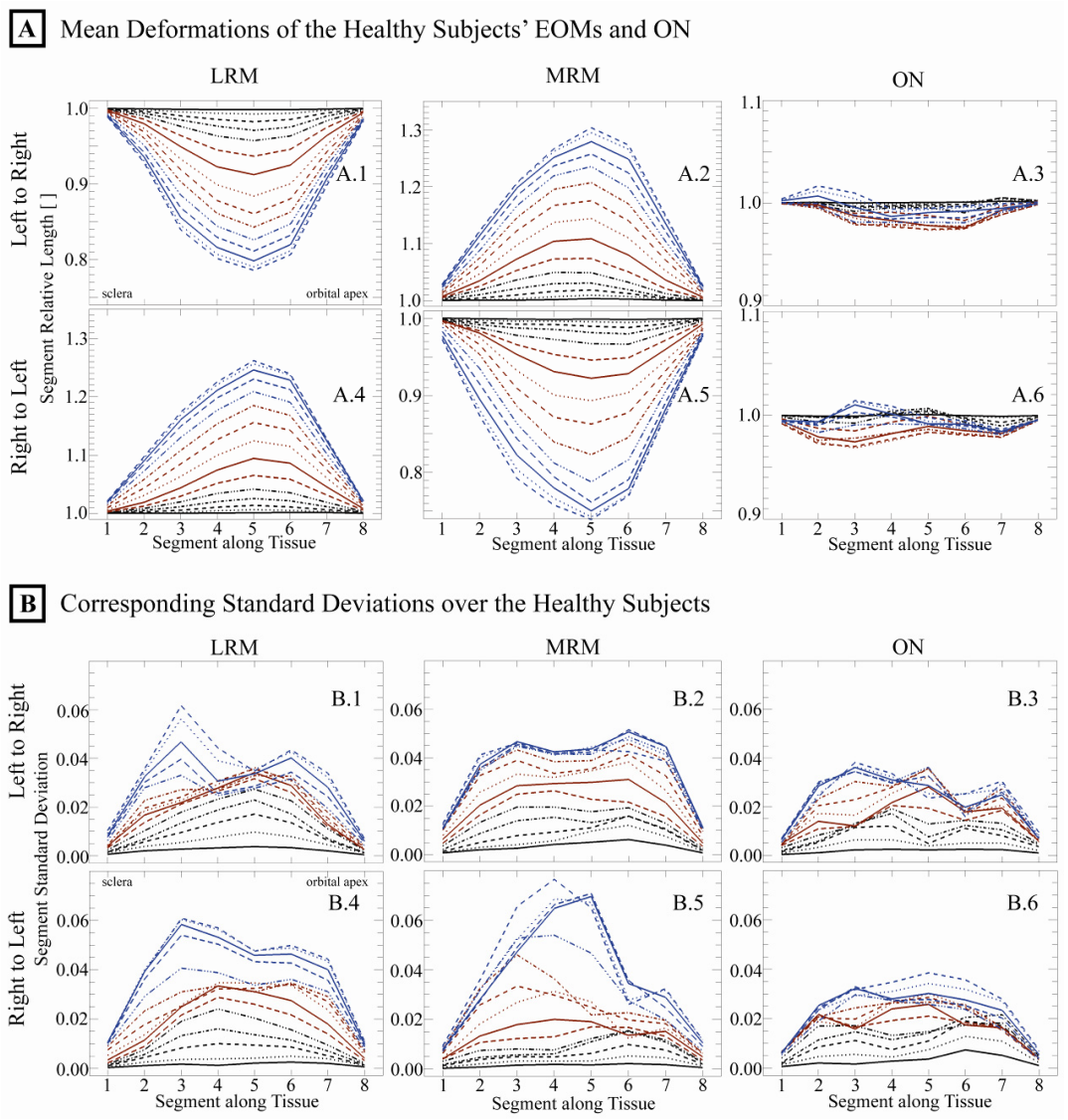

Figure 4.3: ***(A)*** *Summary (average for eleven healthy subjects) profiles of LRM, MRM, and ON (columns), during right eye movements from 20° left to 20° right (first row) and from 20° right to 20° left (second row). X-axis: the two muscles and the ON are partitioned longitudinally into 8 segments. Y-axis: each profile corresponds to one of the fifteen time frames. The first five time frames are drawn in black, the middle five in brown, and the last five in blue. The line type has a period of 6 time frames.* ***(A.1)*** *Relative lengths of the 8 segments of the contracting LRM (compared to the segment lengths at the first time frame) during the eye movement from left-to-right.* ***(A.2)*** *Relative lengths of the segments of the relaxing MRM during eye movement from left-to-right* ***(A.3)*** *Relative lengths of the segments of the ON during eye movement from left-to-right. The relative length of the segments during eye movement from right-to-left are shown in* ***(A.4)*** *for the LRM, in* ***(A.5)*** *for MRM and in* ***(A.6)*** *for the ON. The deformation along the EOMs is heterogeneous, with a maximum deformation posterior to the middle of the muscle. Nevertheless, the deformation kinetics are nearly homogeneous along the EOMs (nearly no change of shape of profiles during the movement). The deformation characteristics of the ON can be interpreted as non-real, since the length of the ON is depicted as a projection of the ON into the image plane and not as a real 3D curved orbital path of the ON.* ***(B.1 to B.6)*** *Corresponding StdDevs among the subjects of the relative lengths in A.1 to A.6. For each profile, the same color and line type are used as the corresponding profile in the A-panels. The StdDevs among the subjects was small (below 8%) and increased from time frame 1 to 15.*

normal. In particular, the deformation of the posterior part of the DSTI LRMs differed significantly from the healthy group. In Sub-panels A.6-A.8, segments 7 and 8 showed aberrant contraction (see arrows, values below 1.0), segments 5 and 6 showed a smaller elongation than normal, and segments 1, 2, and 3 showed an elongation very similar to normal. In Sub-panel A.1, following the pathological contraction of the posterior LRM segments 7 and 8, there was a small but significant elongation at the beginning of the opposite movement. At the beginning of abduction (Sub-panel A.2) the DSTI LRMs contracted. From gaze straight ahead, this contraction did not result in attempted abduction (Sub-panels A.3-A.4). Conversely, in Sub-panels B.2-B.4, the anterior segments 1 and 2 of the DSTI MRM deformed inversely to the healthy MRM, whereas the DSTI MRM posterior half deformed similarly to the normal MRM. Albeit, due to a smaller eye movement, the DSTI MRMs deformed less than the healthy subjects' MRMs.

The local maximal deformations of the DSTI EOMs were shifted in comparison to the healthy EOMs. In contrast to healthy subjects, the DSTI LRM maximal deformations were located on segment 3, closer to the scleral insertion. (Figure 4.4, Panel A). The LRM anterior half deformed more than the posterior half. In contrast, the location of the DSTI MRM maximal deformations was slightly shifted backward to the orbital apex. The maximal local contraction of the LRM was 7% for patient #1 and 8% for patient #2, respectively, while the MRM relaxed locally up to 17% and 27%, respectively. The LRM maximal local elongation was 11% and 14%, respectively, whereas the MRM contracted locally 12% and 19% at most, respectively.

4.4 Discussion

Analysis of motion-encoded MRI provided new detailed insights into how the horizontal EOMs transformed smooth pursuit commands into eye movements. In healthy subjects, the local muscle deformation was heterogeneous. During the entire 40° horizontal eye movement, the maximum deformation amplitude was located nearer to the orbital apex than to the muscles' scleral insertion. A smaller than 40° eye movement led to a smaller but similarly shaped deformation profile. However, the shape and timing of the deformation profiles were altered in two DSTI patients: the aberrant innervation of 3rd cranial nerve fibers into the LRM led to a pathological contraction of the posterior segment of this muscle during adduction. The effect of the pathological neuronal command could be resolved by analyzing the kinetics of deformation of specific EOM segments. The added knowledge supports the accepted hypothesis of the mechanism of globe retraction in adduction in patients with DSTI.[Miller, et al. 1982]

4.4.1 Normal Deformation Profiles of Antagonistic EOMs during Smooth Pursuit

For each eye movement direction, the shape of the EOM deformation profiles remained similar over the whole 40° movement range. For example, the amount of deformation at the 8th time frame (gaze straight ahead) was nearly half of the deformation at the 15th time frame (20° horizontal gaze). The maximal deformation was always located at the same muscle segment during eye movement. Furthermore, the deformation profiles of the two EOMs were similar for the two eye movement directions.

The inter-subject variability of the EOM deformation profiles was low, since the StdDev among the subjects was small in relation to the entire EOM length (4% in average). Yet, the StdDev is not negligible when it is compared to the observed segmental length changes.

In the present study, the LRM deformed to a lesser extent than the MRM, which is expected as the LRM is longer than the MRM. The peak deformation correlated with the amplitude of the eye movement, but the deformation profiles remained similarly shaped for the whole movement

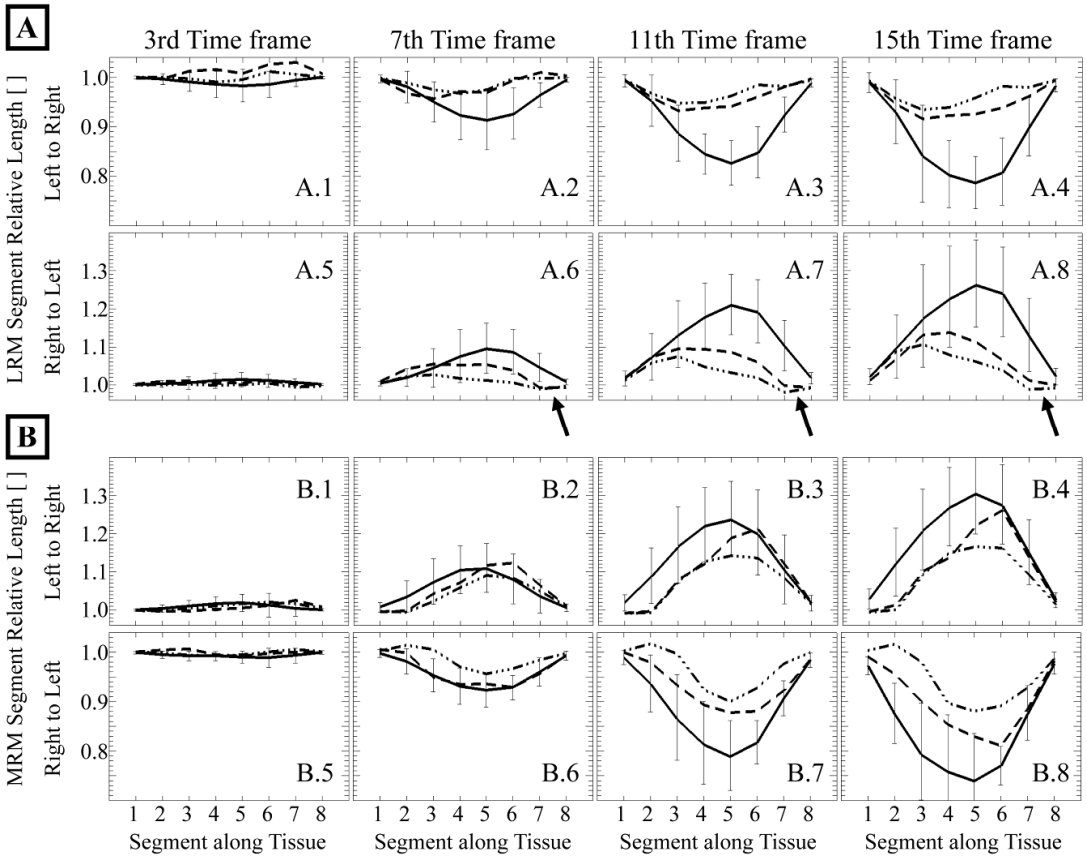

Figure 4.4: Contraction and elongation of the 11 healthy subjects (solid line, all right eyes, error bars: ± 2 StdDevs) and the two DSTI patients, all left eyes, two dashed lines). The gaze directions are switched between the left and the right eye, i.e. the deformation pattern of the right healthy eye EOMs during left-to-right eye movement are compared to the deformation pattern of the left DSTI eye EOMs during right-to-left eye movement. The analysis of these eight segments takes the limited imaging and post processing resolution into account, and therefore, they are independent from each other. Panel A shows the deformation profile of the LRM, panel B shows the deformation profile of the MRM. The first row of each panel corresponds to the eye movement from 20° left to 20° right, the second row to the eye movement from 20° right to 20° left. The columns correspond to the 3rd, 7th, 11th, and 15th time frame, respectively. The error bars are 4 StdDevs wide, so patients' data outside this interval differ significantly (p<0.05). ***(A)*** *The deformation of the posterior half of the DSTI LRMs differed significantly from the healthy group. Sub-panels A.6-A.8: segments 7 and 8 show aberrant contraction in one of the two patients (arrows). Sub-panel A.8: segments 5 and 6 show a smaller relative to normal elongation, and segments 1, 2, and 3 show a similar to normal elongation. Sub-panel A.1: Following the aberrant contraction of the posterior LRM segments 7 and 8, there is a small but significant elongation at the beginning of the opposite movement.* ***(B)*** *In contrast to the LRM, the MRM parallels the ends of the error bars in the control group, since the amplitude of eye movement is reduced.* ***(B5 to B8)*** *However, in one of the two DSTI patients, the anterior segments 1 and 2 of the MRMs contracted instead of relaxed as expected. The DSTI LRM total elongation was smaller than the DSTI MRM contraction.*

range. Therefore, the profile shapes describe EOM relevant properties. On the other hand, the amplitude of the deformation is dependent on the eye movement range.

The ON segment lengths relative to the first time frame reached a minimum at the 8th or 9th time frame for both eye movement directions. These time frames correspond to gaze straight ahead during which the distance from the ON globe insertion to the orbital apex is shortest. In this

position, the ON is curled in the orbit. Since the deformation of the ON could only be reported in the axial image plane, the ON curling out of this plane is misleadingly interpreted as shortening of the ON.

4.4.2 Duane's Syndrome Type I: Altered EOM Deformation Profile as a Consequence of Aberrant Innervation

As documented in postmortem dissections,[Matteucci 1946; Miller, et al. 1982] the LRM is not innervated by the sixth cranial nerve (CN6) in most patients with DSTI. The LRM is innervated by an aberrant branch of the oculomotor nerve (CN3) which normally supplies the MRM. Electromyography[Breinin 1957; Huber 1980] confirmed the LRM endplate functionality by the presence of CN3 action potentials into the muscle. MR imaging showed that aberrant CN3 branches connect with the LRM, [Ozkurt, et al. 2003; Yuksel, et al. 2005] or even that co-innervation of the LRM by the CN3 and the CN6 may occur.[Demer, et al. 2007]

Early studies on DSTI argued that globe retraction in adduction may result from contraction of the agonist MRM combined with missing elongation of the antagonist LRM due to fibrotic reorganization.[Heuck 1879; Duane 1905; DeRespinis, et al. 1993] The co-contraction hypothesis[Walsh and Hoyt 2005] arose from first careful histological examinations[Matteucci 1946] and electromyography data.[Breinin 1957] The present study demonstrates that the DSTI LRM posterior quarter (segments 7 and 8) contracted on adduction (Figure 4.4) leading to globe retraction. Although the LRM anterior segments relaxed to a greater extent than expected, the reported data showed that the entire elongation of the LRM was smaller than the MRM contraction (Figure 4.4) which indeed induced globe retraction. Nevertheless, it is noteworthy that the globe retractions on adduction of the two DSTI patients in our study were relatively small on clinical testing, and were recorded in a limited adduction of not more than 20°.

4.4.3 Postprocessing of Motion-Encoded MRI

The mesh algorithm takes into account that the shapes of the EOMs and the ON remain smooth and regular, which justifies the correction of the mesh irregularities. Tracking the same meshes without the correction of mesh irregularities induced a much higher sensitivity to image noise. The mesh algorithm improved the stability of the tracking procedure and allowed the characterization of eight independent segments along the horizontal EOMs. Since the mesh vertices were homogeneously spread over the tissue width, a higher precision of the tracking procedure was achieved.

A different manner of connecting polylines was recently described. Pan et al. used meshes for the heart[Pan, et al. 2005] and Liu et al. for the tongue[Liu, et al. 2006] to correlate two dimensional motion-encoded image sets, thereby gaining 3D information. Their methods require an additional loop in the tracking algorithm (see Figure 3 in [Pan, et al. 2005]). Our method separates the tracking from the correction procedure, in order not to assign mechanical properties to the tissues a priori, such as smoothness or elasticity (§2.3 in [Pan, et al. 2005]), which would be difficult to determine and would change with the activation of the muscular contraction.

4.4.4 Main Limitations and Future Developments

Manual positioning of the mesh on the EOMs may be a source of errors. Automatic positioning of the meshes would enhance the precision of the methodology. The limited image resolution induced through-slice and in-slice partial volume effects. These effects are accentuated by the fat

shift and the manual positioning of the image slice. Use of 3D imaging with a slight resolution improvement would reduce these artifacts. The scanner bore length and diameter limited the amplitude of the visual target oscillation and hence the gaze movement range.

In conclusion, motion-encoded MRI of the orbit has a number of potential clinical applications. Our work provided deformation profiles for healthy subjects as reference data for a more detailed understanding of the physiology of the EOMs during eye movement. Moreover, using this noninvasive technique, the consequences of aberrant innervation on individual EOM segments in two patients were demonstrated.

4.5 Summary

To study EOM function, the local physiologic contraction and elongation (deformation) along human horizontal EOMs were quantified using motion-encoded MRI. Eleven subjects (healthy right eye) gazed at a target that moved horizontally in a sinusoidal fashion (period 2s, amplitude ±20°), during MR imaging with an optimized protocol. In addition, EOM longitudinal deformations of two patients with DSTI were analyzed. The horizontal EOMs and the ON were tracked through 15 time frames and their local deformation was calculated. Eight segments were separated along the EOMs and compared for left-to-right and right-to-left eye movements. In healthy subjects, the maximal EOM deformation was situated at approximately 2/3 of the muscle lengths from the scleral insertions. The EOM deformations were similar for the entire movement range as well as in both movement directions. In two patients with DSTI, the abnormal innervation of LRM affected specific EOM segments only. The posterior muscle segments contracted and the anterior muscle segments relaxed during adduction. Motion-encoded MRI is a useful technique to advance the understanding of the physiology and pathophysiology of EOMs in humans during eye movement.

Chapter 5: Application to the Vitreous

This Chapter has been published in [Piccirelli, et al. 2011].

5.1 Introduction

The vitreous is a viscous aqueous solution structured by collagen fibers and hyaluronic acid polymers.[Worst and Los 1995; Forrester, et al. 2002] It fills the intraocular space between the lens and the retina. The primary role of the vitreous is to maintain the ocular globe volume, and therefore it needs to be replaced after vitrectomy. Nevertheless, the vitreous and its potential substitutes have to fulfill several other functional and physiological constraints,[Stefansson 2009] the most obvious being transparence to visual light and adequate refraction index. To maintain good vision, appropriate osmotic pressure and viscoelastic properties are important as well.[Neal, et al. 2005]

The vitreous viscoelasticity has both a biochemical and a mechanical impact on the retina. First, it influences diffusive and convective molecular transport.[Xu, et al. 2000] The transport of oxygen and cytokines through the vitreous modifies retinal angiogenesis. Retinal neovascularization can induce traction retinal detachment.[Stefansson 2009] Second, the vitreous viscoelasticity has an impact on the shear stress induced by the vitreous on the retina during eye movement. Excessive shear stress can damage the retina and - once a retinal tear develops – will induce filling of the subretinal space with liquefied vitreous, which separates the photoreceptors from the underlying retinal pigment epithelium, leading to retinal detachment that requires surgical treatment in order to prevent permanent visual loss.[Gariano and Kim 2004; Stefansson 2009]

Collagen membranes compartmentalize the vitreous space. In each of these compartments, the vitreous viscoelastic properties may vary. The binding between these collagen membranes with the hyaluronic acid polymers also impacts on the viscoelastic properties of the vitreous.[Forrester, et al. 2002; Nickerson, et al. 2008] Moreover, the connections of these membranes (going through the retina) with the sclera impede the vitreous deformation locally and increase the (shear) stress acting on the retina, thus increasing the risk of retinal detachment.

The movement of the vitreous relative to the retina is easily revealed by the movement of floaters when moving the eye.[White and Levatin 1962] Nevertheless, so far, the viscoelasticity of the vitreous body has been measured only ex vivo,[Nickerson, et al. 2008] where it varied as a function of the location inside the eyeball.[Lee, et al. 1992] In vivo vitreous deformation data are limited to the work of Zimmerman in 1980, who measured optically the relaxation pattern of the vitreous after a step rotation (saccade) of the eye,[Zimmerman 1980] and Walton et al. in 2002, who used ultrasound.[Walton, et al. 2002] Applying these methods, only the bulk movement of the whole vitreous was considered, so inhomogeneous deformation within the vitreous could not be observed. Buchsbaum, et al. in 1984 tested the adequacy between the vitreous viscoelasticity data obtained ex vivo and the Zimmermann's in vivo relaxation pattern.[Buchsbaum, et al. 1984] The concordance was found to be poor, according to Buchsbaum (p. 294), due to the excessive eye accelerations used by Zimmermann and to a potential inhomogeneity of the vitreous viscoelastic properties, among other factors.

A sinusoidally moving gaze target induces the most accurate eye movements. Vitreous deformation during sinusoidal eye movement has been modeled as a spherical homogenous fluid

rotating around a diameter.[Buchsbaum, et al. 1984; David, et al. 1998] This analytical model uses two dimensionless parameters *a* (modified Womersley number) and *b* (phase angle),

$$a = R_0\sqrt{\omega/|\varepsilon + i\nu|} \quad \text{and} \quad b = \arctan(-\nu/\varepsilon),$$

from which the kinematic viscosity ν and elasticity ε can be derived:

$$\varepsilon = \frac{\omega R_0^2}{a^2\sqrt{1+\tan^2 b}} \quad \text{and} \quad \nu = -\varepsilon \tan b,$$

where R_0 represents the eye radius and ω the circular frequency. The relation to the complex shear modulus *G* is:

$$G = G' + iG'' = \rho\omega(\varepsilon + i\nu),$$

where ρ is the mass density and G' and G'' are the elastic and viscous components of the modulus, respectively. This model is based on the assumption that the viscoelastic properties are homogeneous throughout the vitreous. David et al. in 1998 used ex vivo vitreous viscoelasticity[Lee, et al. 1992] to describe the vitreous deformation.[David, et al. 1998] To better understand the vitreous deformation pattern and to validate simulations,[Buchsbaum, et al. 1984; David, et al. 1998; Repetto 2006] eyeball models have been built.[Repetto, et al. 2005; Stocchino, et al. 2007] Hardware models were needed, as no in vivo measurements methodology existed.[Sebag 2008] However, these models can neither take into account the complex structure of the vitreous[Worst and Los 1995] nor the inter-subjects differences in vitreous properties.

Attempts to determine the mechanical properties of orbital tissues in vivo have been done using MR Elastography.[Litwiller, et al. 2007; Li, et al. 2009] MR Elastography encodes the propagation of externally induced shear waves with phase-locked bipolar gradients.[Muthupillai, et al. 1995] MR Elastography of the vitreous delivers good results post-mortem[Litwiller, et al. 2010] or under anesthesia in animal models[Clayton, et al. 2010]. Nevertheless, MR Elastography encoding is degraded in vivo by the small eye movements necessary to maintain fixation.[Oyster 1999a] Even at a resolution of 0.2x0.2 x1.0mm^3 conventional MRI[Dumars, et al. 2008] could not provide the desired breakthrough in the understanding of the intrinsic vitreous structure.[Gonzalez, et al. 1984; Sebag 2008]

To clarify the role played by the intravitreal membranes, using – instead of antagonizing – eye movements, an MRI method phase-locked to the eye movement itself was developed to determine the vitreous deformation and estimate the viscoelasticity in vivo. The local deformation of the vitreous during sinusoidal eye movements was visualized and quantified. Specific postprocessing software was developed to track the deformation of the monophasic vitreous through the entire ocular movement. The applicability of the commonly used analytical model first described by Buchsbaum et al.[Buchsbaum, et al. 1984; David, et al. 1998; Repetto 2006] to estimate the viscoelastic properties of the vitreous in vivo will be discussed. The change of the vitreous viscosity with age was investigated, as the vitreous is commonly assumed to liquefy with age.[Oyster 1999a]

5.2 Materials and Methods

5.2.1 Subjects and Setup

The study was conducted according to the tenets of the Declaration of Helsinki and approved by the ethics committee of the Health Department of the Canton of Zurich, Switzerland. Each subject agreed to participate after the scientific value and possible risks of the study were explained. The right eye of nineteen healthy subjects (eight women and eleven men; mean age: 32 years; range:

14 to 62 years of age) were imaged. Visual acuity of all subjects was sufficient to track the visual stimulus.

A horizontal oscillating white square on a black background (target size = 0.4°, luminance = 5.1 ± 1 cd/mm^2 on a background of 0.05 ± 0.02 cd/mm^2) was used to induce sinusoidal smooth pursuit eye movements with an amplitude of ±20° and a period of 2s (corresponding to a maximal angular eye velocity of 63°/s). Sinusoidal movements were chosen because the vitreous model used to fit the imaged deformation is analytically solvable for sinusoidal eye movements. For the presentation of the visual stimulus, a computer, projector, projection screen, and the software "Presentation" (Neurobehavioral Systems Inc., Albany CA, USA) were used as described in [Piccirelli, et al. 2007]. A mirror allowed the subjects to gaze out of the bore to the projection screen. For the MR signal acquisition, a receive-only surface coil of 47mm diameter was placed on the right eye like a monocle, so that the subject could see the target through it. Foam pads immobilized the subject's head. The room light was turned off to maximize the contrast of the stimulus.

5.2.2 MRI Sequence

Axial 2D CSPAMM tagging images[Fischer, et al. 1993] were acquired on a 1.5T MRI scanner (Achieva 1.5T; Philips Healthcare, Best, The Netherlands) with a multishot segmented EPI gradient echo sequence (Figure 5.1 and Figure 5.2). The lens center and the scleral insertion of the ON defined the imaging plane. The 40° right-to-left eye movement was split into fifteen time frames of 70ms (with 12ms of acquisition and 58 ms of separation), resulting in a total acquisition of 15x70=1050ms. The remaining 950ms of the 2s periodic eye movement served for MR signal recovery. The tagline distance was 3mm. Other parameters were identical to those described previously: 140 × 140 mm^2 FOV, 1.2 × 1.2 × 4.0 mm^3 scan resolution, 8 signal averages, and a 256 × 256 reconstruction matrix.[Piccirelli, et al. 2007] The use of an EPI factor of 5 shortened the acquisition time to 4.5 minutes.

5.2.3 Postprocessing

A postprocessing technique specially dedicated to the vitreous geometry was developed, based on the mesh tracking algorithm introduced by Piccirelli, et al.[Piccirelli, et al. 2009a]

The vitreous was overlaid at the 9th timeframe (approximately gaze straight ahead) with a 60x36 radial mesh centered on the center of rotation and with its outermost polygon on the sclera (in green in Figure 5.3, middle Panel). To ascertain that the meshes lay only on the vitreous, anatomical images were taken as references and realigned the meshes if needed.

Using the dedicated mesh-algorithm, the mesh vertices were tracked through 15 time frames. The software was based on TagTrack 1.7.0 (GyroTools Ltd., Zurich, Switzerland) integrating HARmonic Phase (HARP)[Osman, et al. 1999] with peak-combination.[Ryf, et al. 2004b] A circular band pass filter was applied to extract the harmonic peak in Fourier space. The diameter of the filter corresponded to 2.3 image pixels.[Kuijer 2000]

The quantified vitreous deformation could be used to challenge the analytical model commonly used to describe the vitreous deformation.[Buchsbaum, et al. 1984; David, et al. 1998; Repetto 2006] As opposed to the data obtained by Zimmermann during fast eye movements,[Zimmerman 1980] the deformation of the vitreous during rather slow sinusoidal eye movement should be better described by the model. In effect, the model estimates the vitreous deformation for repetitive sinusoidal eye movements. If this model correctly describes the physics of the vitreous deformation, then the viscoelastic properties of the vitreous can be estimated by fitting the model parameters to the observed vitreous deformation.

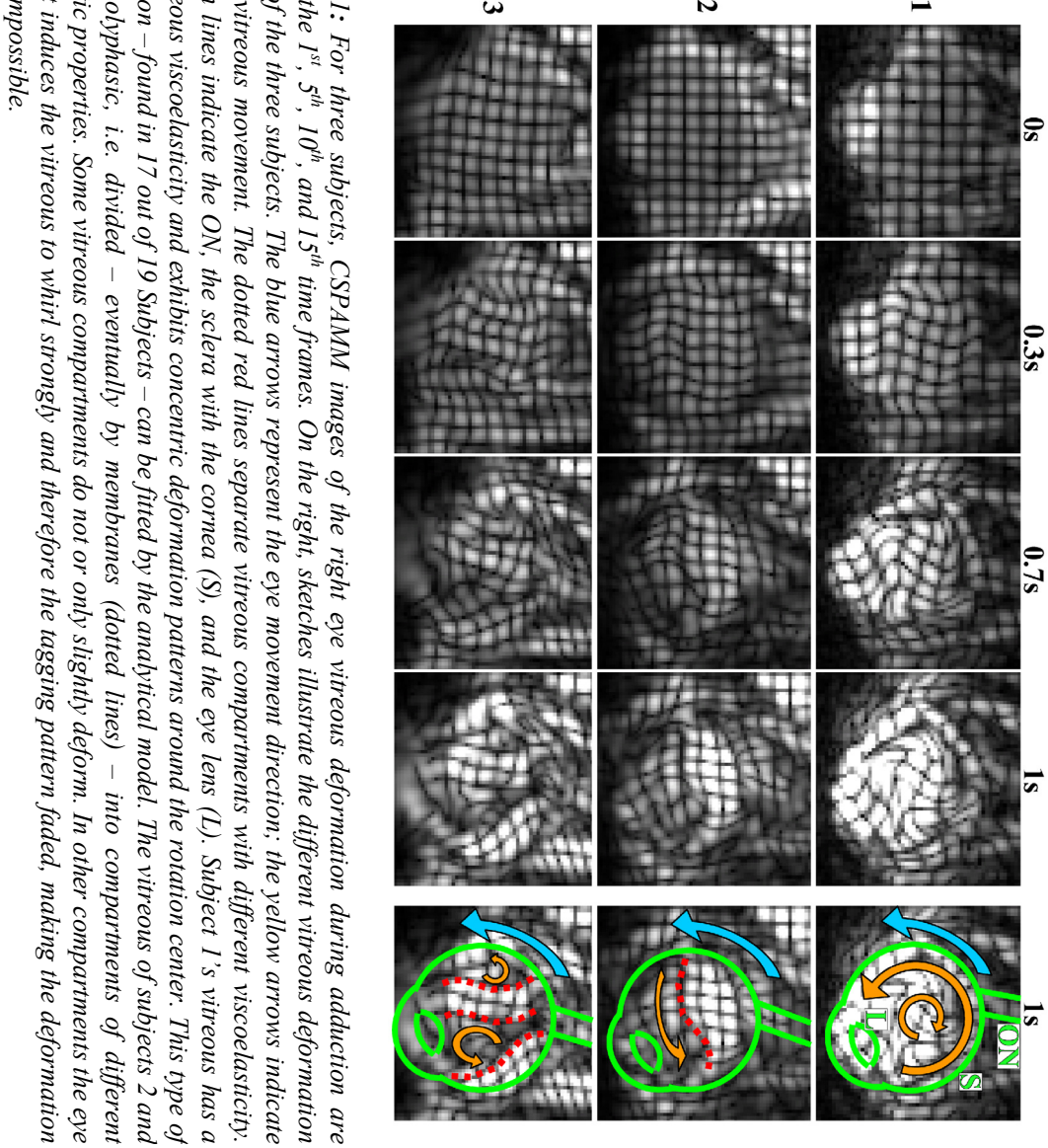

Figure 5.1: For three subjects, CSPAMM images of the right eye vitreous deformation during adduction are shown at the 1st, 5th, 10th, and 15th time frames. On the right, sketches illustrate the different vitreous deformation patterns of the three subjects. The blue arrows represent the eye movement direction; the yellow arrows indicate the local vitreous movement. The dotted red lines separate vitreous compartments with different viscoelasticity. The green lines indicate the ON, the sclera with the cornea (S), and the eye lens (L). Subject 1's vitreous has a homogeneous viscoelasticity and exhibits concentric deformation patterns around the rotation center. This type of deformation – found in 17 out of 19 Subjects – can be fitted by the analytical model. The vitreous of subjects 2 and 3 were polyphasic, i.e. divided – eventually by membranes (dotted lines) – into compartments of different viscoelastic properties. Some vitreous compartments do not or only slightly deform. In other compartments the eye movement induces the vitreous to whirl strongly and therefore the tagging pattern faded, making the deformation tracking impossible.

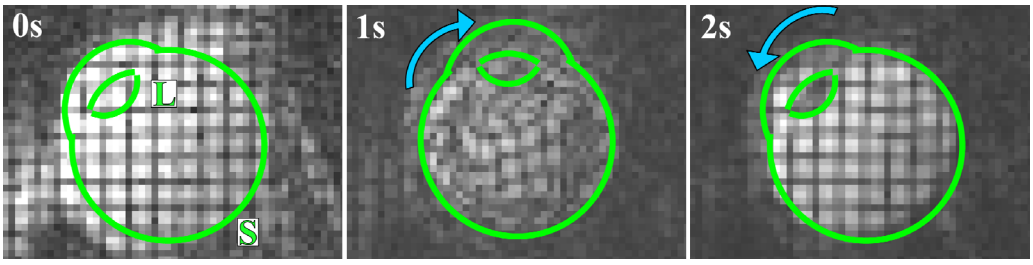

Figure 5.2: Axial CSPAMM images of a right eye vitreous deformation during a complete adduction-abduction-adduction cycle are shown at the 1st, 15th, and 30th time frames. The blue arrows represent the eye movement direction. The green lines indicate the sclera with the cornea (S), and the ocular lens (L). The vitreous of this subject has a homogeneous viscoelasticity and exhibits concentric deformation patterns around the rotation center. The eye movement induces

the vitreous to whirl and therefore the tagging pattern to deform strongly. Nevertheless, this deformation is reversed by the eye's abduction, making the rectangular tagging pattern reappear at the 30th time frame. This proves that the whirling of the vitreous due to this type of sinusoidal eye movement remains in the laminar regime, as opposed to turbulent flow. The signal decrease of the eye lens due to its shorter T1 can also be observed.

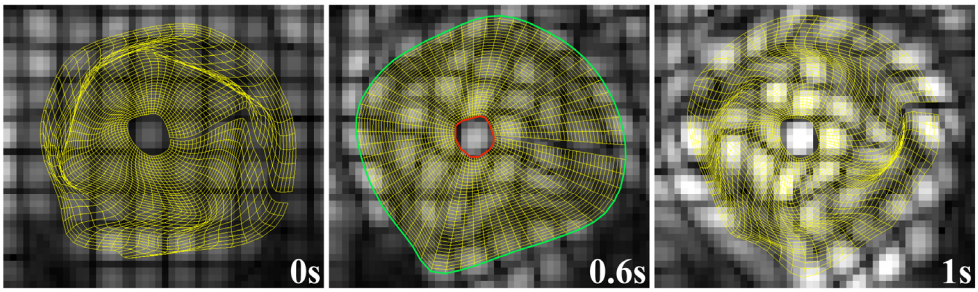

Figure 5.3: Axial CSPAMM image of the right eye vitreous during abduction-to-adduction at the 1st (0s), 9th (0.6s), 15th (1s) time frames. Superposed on the vitreous is the automatically tracked mesh (in yellow). At the 9th time frame, the red polygon was laid around the rotation center and had a radius slightly bigger than the tagline distance. The green polygon was laid on the border of the vitreous, i.e. on the sclera and the lens. The mesh was defined by radial interpolations of the red and green polygons. The mesh includes 36 concentric polygons of 60 vertices each. Each concentric polygon was tracked through the 15 time frames. The rotation of these concentric polygons is reported in function of time, in Figure 5.4A. To better illustrate the mesh deformation, one segment of the concentric polygons has not been drawn.

The rotation angle of each concentric polygon forming the mesh was used to find the parameters *a* and *b* – of the analytical model described in Buchsbaum et al.[Buchsbaum, et al. 1984] – best describing the vitreous motion. A L2 norm showed the best fitting results. To avoid fitting problems, if several of the outermost polygons exhibited a similar rotation pattern (difference<0.5°) at the interface vitreous-sclera, only the innermost of these polygons were considered to lay on the interface sclera-vitreous (or vitreous cortex-vitreous center) and were included in the fitting procedure. By doing so, polygons lying on the sclera that would spoil the fitting of the model were avoided, which assumes that only the outermost polygon is lying on the interface sclera-vitreous. The radii of the outermost and innermost polygons were taken into account for fitting. The outermost polygon rotation amplitude was determined and included in the model, before the rotation of the concentric polygons as a function of time was fitted with the analytic viscoelastic model[Buchsbaum, et al. 1984; David, et al. 1998] to determine the parameters *a* and *b*. The fit was done for *a* in the range [1:20] with a step of 0.19, and for *b* in the range [–3.0:–0.1] with a step of 0.03. Nota bene, a mechanical system at a movement frequency higher than a (potential) resonance frequency, will have a phase shift below $-\pi/2$,[Gerthsen, et al. 1992] which implies that the value of *b* would be $-\pi < b < -\pi/2$, even for an overdamped system. This impacts the sign of the viscosity, but not the elasticity, as seen from the above equations.

To verify the consistency and stability of the postprocessing procedure, the accordance of the mesh rotation between several datasets (acquired on the same day) was checked for each subject. In addition, for four subjects, the left-to-right eye movement was acquired. Finally, for the same four subjects, the whole procedure was repeated on another day.

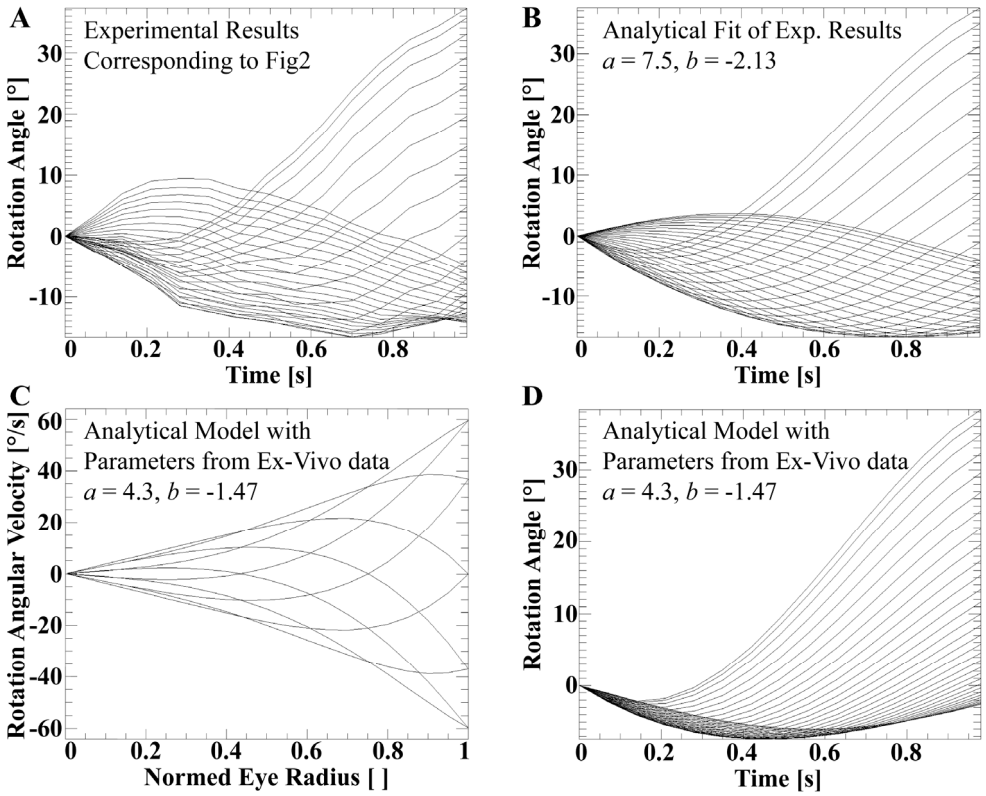

*Figure 5.4: (**A**) Rotation angle as a function of time for each of the up to 36 concentric polygons of the mesh of Figure 5.3. The outermost polygon undergoes a sinusoidal rotation of nearly 40°, corresponding to the gaze movement. The rotations of the other polygons differ in amplitude and phase. (**B**) Analytical model fitted to the vitreous deformation depicted in Panel A, determining a and b, from which the viscoelasticity can be calculated. (**C**) Deformation of the vitreous expected from a typical ex vivo data set.[Lee, et al. 1992; David, et al. 1998] At r=0, the center of the eye ball, the circumferential velocity component represented here is (set to) zero due to symmetry, as the eye ball was assumed to be spherical. (**D**) From the radial velocity distribution for each time (see Figure 7 in David, et al.[David, et al. 1998]), the rotation angle over time of concentric circles was calculated for a better comparison with Panels (A) and (B).*

5.3 Results

For all 19 subjects, the acquisition of CSPAMM images of the vitreous deformation was successful. The reproducibility of the final fitting results for acquisitions on two different days and eye movement directions were, for the first four subjects, within a 10% range, i.e. the obtained values *a* and *b* did not vary by more than 10%. Therefore only one examination with one movement direction (adduction) was acquired for the 15 following subjects.

The vitreous deformations of two subjects (women, 51 and. 22 years old) were clearly polyphasic, i.e. divided into compartments of different viscoelastic properties. During eye movement, some compartments of the vitreous underwent only bulk deformation, i.e. did not or only slightly deform, whereas others underwent swirling deformations (Figure 5.1, subjects 2 and 3). These compartments seemed sharply separated (doted red lines in Figure 5.1), corresponding to reported intravitreal membrane patterns.[Busacca 1967; Eisner 1982; Worst and Los 1995] For subject 2, the posterior part of the vitreous remained almost static and deformed only slightly. On the contrary, the anterior part was affected by the eye movement and deformed more strongly. Subject 3's vitreous showed a complex compartmental structure. Four vitreous compartments

with different deformation patterns could be differentiated. These compartments are oriented perpendicularly to those of subject 2.

The other 17 subjects had a monophasic vitreous (i.e., homogeneous viscoelasticity), with a deformation pattern similar to subject 1 (Figure 5.1) and Figure 5.2. The vitreous exhibited concentric deformation movements around a rotation center. The phase and the amplitude of these concentric rotations depended upon their distance to the rotation center and were subject dependent. With increasing distance from the rotation center, the vitreous rotation amplitude increased and the phase shift relative to the eye movement decreased. The deformation of the vitreous was reversible, and after a period of the movement came back to the original configuration, as expected for laminar flows.

Quantitative evaluation could be obtained for all 17 subjects with a monophasic vitreous, as the vitreous deformation could be successfully tracked over the whole movement range, using the dedicated mesh algorithm (Figure 5.3). Each of the concentric polygons could be tracked through the 15 time frames. Nevertheless, some inconsistency of the mesh due to tracking imperfection was still visible in the locations of the highest shear deformation. For subject 1, the four outermost polygons described the same rotation patterns, and therefore were considered to lay on the sclera. The rotations of the inner 32 concentric polygons were plotted in function of time in Figure 5.4A (for the mesh of Figure 5.3). The outermost polygon underwent a sinusoidal rotation slightly below 40°, in concordance to the gaze movement. The rotation of the other polygons differed in amplitude and phase. The innermost polygon changed its rotation direction around 0.3s after the sclera, had a movement range of nearly 16° and a phase delay relative to the sclera of nearly 1.3s. As expected for a viscoelastic fluid, the amplitude and phase varied smoothly from the innermost to the outermost polygon.

By fitting the vitreous deformation with the analytical model, the parameters a and b could be specifically determined (Figure 5.4B). For comparison, the deformation pattern expected from ex vivo vitreous viscoelasticity measurements is depicted in Figure 5.4D. This procedure was repeated for all 17 subjects with a monophasic vitreous. The a and b values are plotted in function of the subject's age (Figure 5.5). The values obtained for a vary from 4.0 to 7.6, and for b from –2.66 to –2.02. The correlation coefficients between the age and a respectively b are -0.27 and 0.09 - both not significant. The correlation coefficient between a and b is -0.76 - significant with a double-sided p-value smaller than 0.01.

5.4 Discussion

The deformation of the vitreous during sinusoidal eye movement was determined in-situ, revealing the topology of the intravitreal structures' influence on the vitreous dynamic. Polyphasic and monophasic vitreous could be differentiated. For the first time, the inhomogeneous deformation of the monophasic vitreous could be quantified in vivo. These results challenge the commonly used viscoelastic deformation model of the vitreous, and the assumed deformation pattern and the resonance properties of the system, and accentuate the need for extended models.

The presented method resolves the local deformation of the vitreous during eye movement. In the image plane, the local movement of the vitreous can be followed up to the scale of the image resolution. The combined use of HARP[Osman, et al. 1999] (to downsize the smallest displacement resolvable) and of sequential acquisition (to shorten the time phase duration) made the determination of the vitreous viscoelasticity possible, as discussed by Buchsbaum.[Buchsbaum, et al. 1984] Inhomogeneous deformation patterns inside the vitreous can be determined for both monophasic and polyphasic vitreous. The good SNR (SNR) of the vitreous tagging pattern was achieved due to the use of a small surface coil, and to the long MR signal recovery time of the vitreous.[Fischer, et al. 1993]

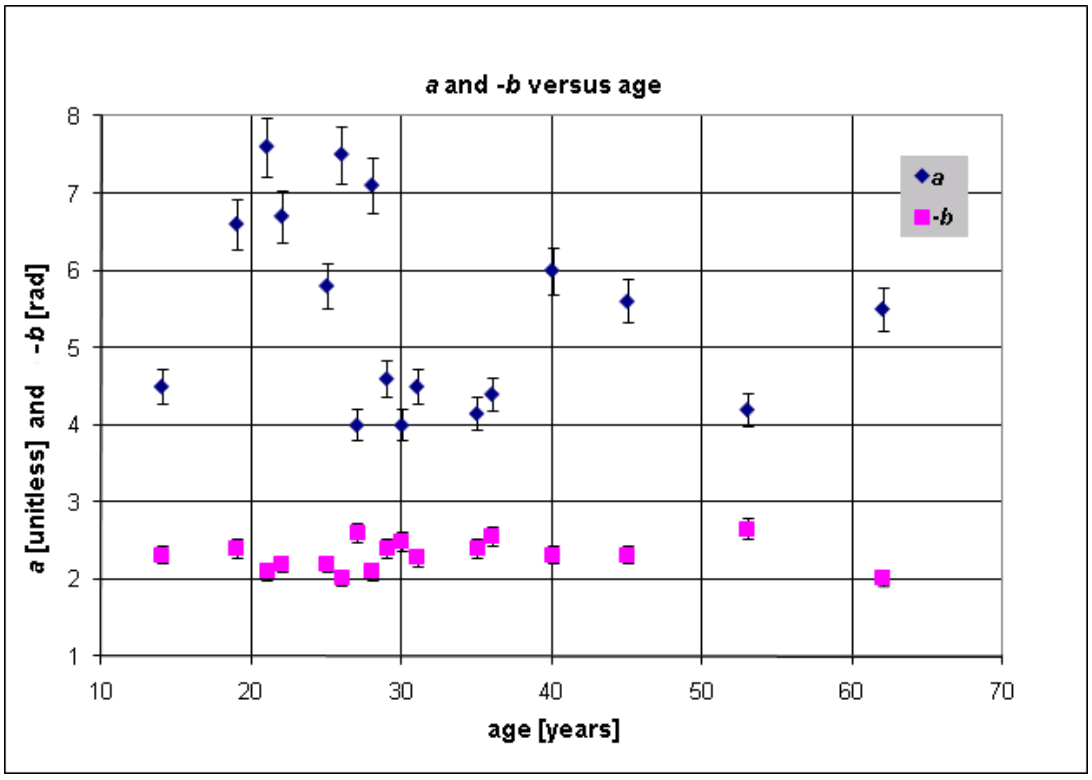

Figure 5.5: For each of the 17 subjects with monophasic vitreous, the a and -b values obtained from the fitting of the vitreous deformation with the analytical model are plotted as a function of the subject's age. The correlation coefficient between the age and a resp. b are -0.27 and 0.09, both not significant. The correlation coefficient between a and b is -0.76, significant with a double-sided f-test p-value smaller than 0.01. The drawn measurement error ranges on a and b are of 10%.

5.4.1 Determination of the Vitreous Deformation in Vivo

For a monophasic vitreous, the rotation angle as a function of the distance to the rotation center was resolved and quantified. By contrast, the movement of "mouches volantes" gives only a basic impression of the vitreous deformation,[White and Levatin 1962] that lacks systematic description of the vitreous deformation. Zimmermann, in 1980, was the first to investigate quantitatively the vitreous deformation during eye movement.[Zimmerman 1980] With an optical system, the relaxation of the vitreous after saccadic eye movements was determined. A laser beam traversing the vitreous was used to depict a scattering pattern on the retina. The movement of this scattering pattern was used to describe the vitreous deformation. This method assumes the vitreous rotates as a single bulk solid, and therefore a single angle was defined to describe the vitreous rotation over time. Zimmerman's method's major drawback is the exclusion of shear deformations of the vitreous. The same concerns apply to ultrasound methods.[Walton, et al. 2002] The smaller rotation angle of the inner vitreous compared to the outermost vitreous is presumably due to dissipation of the traction force acting on the vitreous periphery.

The reversibility of the vitreous deformation during the second half of the movement was easily tested. To visualize the deformation of the vitreous over the whole period (right-to-left and left-to-right) of the eye movement, 32 time frames (instead of 15) were acquired for some subjects with monophasic vitreous(see Figure 5.2), and advantage was taken of the long MR signal recovery time of the vitreous magnetization (T_1~5s).[Patz, et al. 2007] The deformation of the vitreous was reversible, indicating that only a small amount of dissipative turbulent flow was created during the

movement. Analytical simulations[Repetto 2006] and hardware models[Stocchino, et al. 2007] predicted turbulent flow in the neighborhood of the eye lens. The presence of intravitreal membranes[Eisner 1982] may be responsible for diminishing the turbulences around the lens. Only at the vitreous-sclera interface was a small signal decrease observed. This could be due to magnetic field inhomogeneities or to the T_1 difference between the retina and the vitreous.

The image resolution was sufficient to resolve regions of different deformation patterns inside the vitreous. The viscoelastic deformation varied between subjects. For the 17 subjects with monophasic vitreous, the qualitative comparison between the depth and the phase shift of the peripheral movement propagation into the center of the vitreous allows a rough estimation of the underlying viscoelastic vitreous properties. Moreover, for the first time the convection of the vitreous predicted by a vitreous membrane model[Repetto, et al. 2004] was observed.

Two of the 19 studied subjects had a polyphasic vitreous and their deformation patterns were very different from each other. The vitreous of subject 2 (woman, 51 years old, low myopia) was separated in two zones (Figure 5.1). The anterior zone deformed more than the posterior zone. This anterior-posterior separation could be due to vitreous collapse[Oyster 1999a; Eisner 2008] or to inhomogeneities of the vitreous structure[Busacca 1967]. Vitreous collapse is a common aging process,[Bishop 2000] as 65% of the population older than 65 years have a detached vitreous.[Oyster 1999a] During shrinkage, the vitreous detaches from the posterior retina and fluid vitreous humor fills the space between the collapsed vitreous structure and the retina. This process may occasionally lead to the development of peripheral retinal tears at the site of the anteriorly located vitreous base and ultimately to retinal detachment. The deformation of the anterior part of subject 2's vitreous during the eye movement may be due to the presence of fibers connecting the retina with the vitreous and to the resulting higher vitreous viscosity. On the contrary, in the less viscous posterior vitreous, where the collagen fibers are absent after a collapse, only little vitreous deformation is visible.

In contradistinction, the zone pattern of subject 3's vitreous (woman, 22 years old, high myopia) does not correspond to a vitreous collapse pattern. The four observed zones are oriented in the anterior-posterior direction. This orientation is rather consistent with an intact vitreous structure, as reported by Eisner.[Eisner 1982, 2008] The two compartments on the medial and lateral side of the vitreous especially seem to correspond to the reported tractus preretinalis originating at the ora serrata.[Worst and Los 1995] Nevertheless, the alternation of zones of different viscoelasticity does not correspond to Worst's description of a more rigid vitreous cortex and a more fluid inner core.[Worst and Los 1995]

5.4.2 Quantification of the Vitreous Deformation and Vitreous Viscoelastic Model

The quantification of the vitreous deformation challenges the commonly used viscoelastic vitreous deformation model.[Buchsbaum, et al. 1984; David, et al. 1998; Repetto 2006] This model assumes small displacement amplitudes. Our main finding is that the in vivo viscoelastic deformation of the vitreous can be satisfyingly fitted by this simple analytical model only for values of the parameter b lower than $-\pi/2$. The phase shift of the rotation of the inner vitreous relative to the sclera was bigger than $\pi/2$; i.e. $-\pi < b < -\pi/2$. Therefore the mechanical system studied has a resonance frequency which is lower than the one used for the eye movements (0.5Hz).

The parameter a (modified Womersley number) decreases with age (see Figure 5.5). Nevertheless, the correlation between age and a is rather weak (-0.27). The correlation coefficient between a and b is relatively high: -0.76. From the obtained a and b values, the viscosity and elasticity are derived as summarized in Table 5.1.

	Elasticity ε [m^2/s]	kinematic Viscosity ν [m^2/s]
minimum value	0.026	0.050
maximum value	0.181	0.132
average value	0.093	0.089
StdDev	0.053	0.028

Table 5.1: Vitreous viscosity ν and elasticity ε calculated from the parameters a and b of the commonly used viscoelastic vitreous model best fitting the in vivo vitreous deformation.

The viscoelastic deformation determined in vivo differs remarkably from the one expected by the simple analytical model using averaged ex vivo viscoelasticity measurements. As mentioned by Nickerson et al.,[Nickerson, et al. 2008] this difference might be explained by the degradation of the intravitreal collagen fiber structure through the vitreous extraction,[Lee, et al. 1992] the time elapsed between the extraction and the ex vivo measurements, or several others issues related to ex vivo viscosity measurements.[Vappou, et al. 2007] A modification of the hyaluronic acid polymerization state could also impact on the vitreous viscoelastic properties.[Worst and Los 1995] Even after age related vitreous liquefaction, collagen structures, eventually collapsed, are still present inside the eye globe, and can affect the vitreous rheology. Moreover, the variety of methodologies, shear frequencies, and viscosity definitions used in the literature[Bettelheim and Wang 1976; Kawano, et al. 1982; Buchsbaum, et al. 1984; Lee, et al. 1992; Nickerson, et al. 2008; Swindle, et al. 2008] combined with frequency dependence and bimodality[Gisladottir, et al. 2009] of the vitreous viscoelasticity, make a meaningful comparison difficult. Nevertheless, the value found for the storage and loss components of the viscoelastic modulus G - at the relatively low eye movement frequency used - are around 3±1 hPa, which is one order of magnitude above the values obtained from the high frequency ex vivo measurement made after degradation of the intravitreal membranes.[Bettelheim and Wang 1976; Buchsbaum, et al. 1984; Nickerson, et al. 2008]

The viscosity and the elasticity act both on the depth and on the phase shift of the propagation of the sclera movement into the center of a monophasic vitreous. Nevertheless, the propagation depth and phase shift are the relevant mechanical properties of the movement that determine the local shear stresses inside the eye globe. Therefore, it seems reasonable to postulate that the appropriate description of pathological vitreous will not be its viscoelasticity, but its movement propagation depth and phase shift.

5.4.3 Main Limitations and Future Developments

The analytical model assumes homogeneous viscoelastic properties of the fluid and a spherical shape of the vitreous space. Furthermore, the model is linear in the force deformation relationship, which may not hold for the relatively big deformation observed. Nevertheless, an “apparent” viscoelasticity of the subjects’ vitreous can be determined. The small difference between 2D and 3D models with a spherical or anatomically correct eye shape, pointed out by Repetto et al., is not relevant for our study.[Repetto, et al. 2005; Repetto 2006] The concavity of the vitreous space created by the eye lens has a small but not negligible impact on the deformation pattern. Other models, taking into account the geometry of the eye globe,[Repetto, et al. 2005; Stocchino, et al. 2007] would presumably improve the biomechanical understanding of our in vivo data. For example, the simple membrane model proposed by Repetto et al. in 2004 (see their Figure 7),[Repetto, et al. 2004] could explain the observed pattern of vitreous convention, which slightly modified the location of the vitreous whirling center for the right-to-left eye movement compared to the left-to-right eye movement.

For some subjects, several concentric polygons in the periphery described the same rotation over time. A possible explanation could be the rather rigid cortex of the vitreous moving similarly to the sclera to which it is attached. Another explanation could be the limited resolution and the relatively high signal intensity of the sclera at the first time frame, inducing several polygons to describe the rotation pattern of the sclera. The analytical model is not able to take into account varying viscoelastic properties, therefore only the innermost of the polygons describing a rotation similar to the outermost polygon was considered for fitting. Therefore, the effective radius of the innermost polygon was used for fitting.

The limited resolution of the acquired images and the further worsening due to harmonic peak extraction[Rutz 2008] may prevent the visualization and moreover the quantification of the details of vitreous deformation, like the deformation in the neighborhood (< 2mm) of the eye lens. Moreover, due to the ample vitreous rotation, the limited resolution in conjunction with the quite broad tagline distance creates signal voids through partial volume effects. Vitreous whirling induces the tagging pattern to fade, making the deformation tracking more difficult. The accuracy of the determination of the vitreous rotation center is limited by the resolution and the non-automatic procedure. On the other hand, the limited resolution itself and the size of the innermost polygon give a tolerance upon the exact determination of the rotation center. The ocular lens and intravitreal structures may also modify the position of the whirling center of the vitreous depending upon the eye movement direction, as has been modeled by Repetto et al.[Repetto, et al. 2004]

The effect of the HARP filter size on the quantification of the deformation pattern was also tested. In fact, a primary resolution limitation of rotation angle of small structures is inherent to the HARP filtering. The smaller an object is, the broader its Fourier transform. For an object of double the size of the acquired resolution almost no rotation can be depicted without losing information about the object size or shape. For an object of the size of the image, the maximal illustratable rotation is of 60° - using a circular HARP filter. The vitreous was about 2.5cm in diameter. If it rotated as a whole, the maximal illustratable rotation would be of around 55°. From an object of about one fifth of the vitreous size, SNR begins to decrease as soon as the rotation exceeds 30°. As the quantification of the deformation pattern remained unchanged by increasing the filter size, it was concluded that the filter size used was sufficient.

As pointed out by Buchsbaum,[Buchsbaum, et al. 1984] the viscoelasticity may depend upon the movement range and speed. Similar experiments with different eye movements may provide further insight into any non-linearity of vitreous mechanical properties.

In conclusion, our novel method enabled us to rigorously validate or refute models of vitreous dynamics in vivo. The difference between the observed deformation of the vitreous and the one expected from ex vivo measurements of the vitreous viscoelasticity is remarkable, and is presumably due to the presence of intact intravitreal structures. A model incorporating membranes immerged into a viscoelastic fluid inside an eye ball geometry including the eye lens could probably adequately explain our reported in vivo data of vitreous deformation.

Noteworthy, and possibly relevant for eye movement control,[Schovanec 2001] is the modification of the eye ball inertia through the vitreous deformation. This issue should be considered when modeling the orbital mechanics.

Further studies are needed to investigate if the vitreous viscoelasticity and/or the tractions at the vitreous base are relevant for retinal tears to appear. Saccadic eye movements may give rise to an informative decay phase, especially for the determination of resonance frequencies, as shown by Zimmermann.[Zimmerman, et al. 1985] The vitreous rheology may also play a role in eye lens pathologies. Epidemiological studies about vitreous liquefaction were, up to now, unlikely to be measured.[Oyster 1999b] Now, the provided tools make the study of these clinically relevant topics possible.

5.5 Summary

Retinal detachment results in visual loss and requires surgical treatment. The risk of retinal detachment depends, among other factors, upon the vitreous rheology, which varies with age. Up to now, the viscoelasticity of the vitreous body has only been measured in cadaver eyes. However, the ex vivo and in vivo viscoelasticity may differ, due to the effect of intravitreal membranes. Therefore, a MRI method and appropriate postprocessing tools were developed to determine the vitreous deformation and viscoelastic properties in eyes of living humans. Nineteen subjects (8 women and 11 men; mean age: 33 years; age range: 14 to 62 years) gazed at a horizontal sinusoidal moving target during the segmented acquisition of CSPAMM images. The center of the lens and the scleral insertion of the ON defined the imaging plane. The vitreous deformation was tracked with a dedicated algorithm, and fitted with the commonly used viscoelastic model to determine the model parameters: the modified Womersley number *a* and the phase angle *b*. The vitreous deformation was successfully quantified in all 17 volunteers having a monophasic vitreous. The model parameters' mean and StdDev were determined to be 5.5±1.3 for *a* and -2.3±0.2 for *b*. The correlation coefficient (-0.76) between *a* and *b* is significant. At the eye movement frequency used, the mean storage and loss moduli of vitreous are around 3±1 hPa. For two subjects, the vitreous deformation is clearly polyphasic: some compartments of the vitreous are gel-like and others liquefied. These compartments' boarders correspond to reported intravitreal membrane patterns. The deformation of the vitreous can now be determined in situ, leaving the structure of the intravitreal membranes intact. Their effect on vitreous dynamics, presumably, challenges actual vitreous viscoelastic models. The determination of the vitreous deformation will help quantify local vitreous stresses and their correlation with retinal detachment.

Chapter 6: Discussion, Outlook, and Conclusion

6.1 Main Findings, Importance and Limitations

A better understanding of the causes of ocular misalignment may improve the treatment of disorders of the oculomotor system. Conventional strabological investigative methods, such as Hess and Harms tangent screens' tests, intra-operative forced duction tests, or static MRI, are useful to characterize the underlying eye movement disorders. Nevertheless, in more complex cases, the insight given by these techniques into the pathophysiology of the diseases does not always allow a clear diagnosis, even more after preceding surgery. The biomechanical linking of eye movement data with static orbital tissue conformations is indeed difficult. Information about the dynamics of the orbital tissue conformation during eye movements is sought, as these new observations would challenge eye plant models.

The presented methods permit to induce repetitive and accurate eye movements inside the scanner bore, to accelerate image acquisition, and to automatically quantify the deformation of orbital tissues. A clinically usable visual stimulus induced eye movements inside the scanner repetitive enough to perform segmented acquisition. By using acceleration methods such as k-t BLAST and reduced FOV, the scantime is short enough to assure accurate eye movements. Further, the use of motion and velocity encoded images of the orbit increases the relevance of the acquired data and to optimally use limited scantime. For the remaining small aperiodic components of the eye movements that induce motion artifact in the phase encoding direction, methods have been proposed to efficiently diminish such motion artifacts.

If the impairment of one EOM persists, the other EOMs adjust. To study such phenomena, 3D data are necessary to depict the movement of all EOMs simultaneously. The methodological extension from 2D to 3D MRI data has also been demonstrated. 3D motion-encoded data of the orbit can be performed within a tolerable scan time, nevertheless, compensating for the decreased SNR relative to 2D data due to the reduced FOV is necessary.

Quantitative information has been extracted from dynamic MR data using the developed postprocessing tools. Thereby, new observables of the orbital mechanics and eye movement control can be used by computational models of the orbit to test hypotheses about ocular rotation, and thus improve the description of orbital mechanics and the origins of eye misalignment.

Using the technological improvements described in Chapters 2-5, the first high-resolution, motion-, and velocity-encoded images of the orbit during smooth pursuit eye movement were obtained. Inhomogeneous deformation along the EOMs has been described. Further, the inhomogeneous contraction along the EOMs has been differentiated between pathological (DSTI) and physiological EOM deformation. Different types of vitreous deformation patterns could be revealed, as well. For the first time, the deformation pattern of the vitreous during sinusoidal eye movements could be visualized, and visco-elastic model parameters could be quantified. These normative data have been used for model comparison.[Wei and Pai 2009; Wei, et al. 2010; Piccirelli, et al. 2011]

The new data that can be obtained with the methods in this thesis should, hopefully, allow the distinction of etiologic categories such as neural palsy, impaired neuromuscular transmission, and mechanical restriction of the EOMs from each other, and further provide insights into some causes of strabismus that challenge traditional concepts of etiology and suggest alternative treatments.

After surgical alteration of the muscle insertions or acute weakening of the muscle, the ocular motor system shows adaptive changes. The proposed techniques may improve the surgical approach by revealing hidden, unusual, and surprising findings on the orbital tissues functionality. The proposed methods enable the access to a multitude of new observations and the determination of material and control properties. Nevertheless, some relevant orbital models parameters such as the mass density or some friction constants may need to be determined using other techniques, to allow the number of model parameters to be diminished to offer a more stable and reliable determination of the clinically relevant information.

In the community interested in eye movement MRI, the nomenclature used to describe orbital chronographic-imaging is rather confusing. Shin, Demer, and Rosenbaum stated that "dynamic imaging refers to viewing the EOMs during different maintained gaze positions."[Shin, et al. 1996] In [Abramoff, et al. 2000] and [Bailey, et al. 1993] the same imaging method is named "cine imaging." Recently, Kau et al. designated it as "multi positional imaging",[Kau, et al. 2006] which seems most appropriate to describe multiple static imaging, as it is not associated with motion. On the other hand, "motion-encoded MRI" refers to imaging using a motion encoding feature and multiple time frames acquired during eye movement. The muscles' paths and contraction patterns may differ during eye movement versus gaze holding, as the resulting force and torque do not need to be null during the movement.[Weber, et al. 2005] The presented work might bring some clarification of these concepts and nomenclatures.

6.2 Applications and Recommendations for Developments

As stated above, 3D data improve the description of non-planar deformations, as is expected for most eye movements. Yet, SNR increase is needed to reliably track deformation data obtained from 3D CSPAMM measurements of the orbit during eye movement. The SNR increase that would result from the use of a surface coil array at 3T may make such quantification possible. More generally, orbital imaging will benefit from a dedicated coil array optimally covering both orbits, with multiple coils per eye. It seems reasonable that imaging both eyes simultaneously would give valuable clinical input for all pathologies involving both eyes, and halve the total examination time, or increase the SNR. However, this array should leave as much as possible of the visual field unobstructed. In addition, the relatively small sensitivity zone of a small coil allows using a small FOV that further shortens image acquisition time (with some SNR penalty). The SNR drop with depth due to the small diameter of the 47 mm diameter coil used in this work was more than compensated by its greater sensitivity.

Especially for 3D data, simultaneous acquisition of anatomical and motion-encoded images may ease the EOM detection in the motion-encoded image. The superposition of anatomical images with the motion- or velocity-encoded data will increase the objectivity of the postprocessing technique. Further, these anatomical images may enable automatic positioning of the 3D meshes (used for tracking) on the EOMs, which, in turn, will reduce postprocessing time. Also, the characterization of orbital fat and connective tissue deformation during eye movement will benefit from 3D acquisition. These tissues influence eye alignment, and optical flow tracking techniques applied to 3D tagged data will give new anatomical and physiological results and identify new sources of ocular movement impairment other than muscular diseases.

Velocity-encoded data may also be useful to determine disease etiologies. Velocity data may be easier to model, as one less derivation (or integration) is needed to connect it to forces. Computationally, a velocity field may also be easier to derive from models. However, magnetic field monitoring during the acquisition[Barmet, et al. 2008] may also be useful to reduce MR artifacts. By modifying the encoder gradient, the phase can be made sensitive to any derivative of the displacement, so that (relative) intraorbital local pressures could also be determined.[Buyens, et al. 2005]

Orbital connective tissues may also be investigated with acceleration-encoded data, even though similar issues as for motion-encoded imaging will appear. In particular, 3D data would be necessary to make a realistic description of these tissues.

CDENSE is more suited to depict small movements than CSPAMM, due to the lower requirements on the MR gradient system, and therefore may be adequate to depict the EOM deformation during small saccades. Small saccades (with a durations of about 20-40 milliseconds) are generally more accurately executable.

To efficiently study eye movement control, models of the orbital mechanics will have to consider the vitreous deformation to be able to incorporate correct eye ball inertia, which is relevant for the force-acceleration relationship. In other words, the force could be modeled from acceleration data, but only if the relevant tissues properties are well described.

The visualization and characterization of vitreous body dynamics during eye movement has the potential to increase the understanding of the dynamic interaction between the vitreous and the retina. Further studies may tell whether the average shear of the vitreous on the retina or/and the traction at the vitreous base induce retinal tears. Shear stress maps at the vitreous-retina interface should help to understand the pathophysiology of vitreous-retina interaction in retinal detachments. Appropriate models could be developed to obtain such information from our data.[Buyens, et al. 2005], and such understanding may help to optimize treatment in patients at risk for retinal detachment, which affects many individuals and leads to blindness when untreated.

The use of goggles with an integrated digital screen may allow more accurate and greater amplitude angles for the stimulus presentation in horizontal, vertical, and oblique gaze directions. Stimulus presentation with goggles and eye movement tracking during the MRI acquisition may improve the image quality, as only data scanned during accurate eye movements could be inserted into the offline image reconstruction. Through this, MR imaging of the orbit during saccades may even become feasible. This is especially important for clinical applications, as the stimulus tracking task may be more demanding for patients than for healthy subjects. Nevertheless, to expand the eye movement range the stimulus can induce would be interesting as pathological or physiological features of the orbital mechanics may be more easily identified. Eye movements with different velocities, different acceleration patterns, in all directions or even circular ones should increase the understanding of the orbital mechanics.

The hypotheses that the different eye movement types use the same muscular neurons and fibers is a highly debated topic of the field of neuro-ophthalmology, with wide reaching implications for other fields of research. For example, the development of a good understanding of the biomechanics of the VOR could clarify its intricate afferent-efferent mechanisms, needed for an effective stabilization of the retinal image in all 3 rotational degrees of freedom of the eye during head movements. The differentiation of diseases' etiologies, by determining which segments of the EOMs are functional and which are not, will impact on surgery planning and reveal the functional importance of the different muscle layers, muscle fibers, and proprioreceptors.

Further, more far-ranging developments would be the combination of dynamical measurements with other methods, like electromyography, electrocorticography, and fMRI recordings, that would give a more comprehensive view of the oculomotor system function.

The final aim is to allow the direct use of the methods on single subjects in clinical settings and provide data for models of the orbital mechanics and oculomotor control. The ability to determine single subject parameters reliably is important as different types of pathologies may induce different abnormal deformation patterns of the EOMs, and the surgery needs to be fitted to the particular needs of the patient. For example, early in its course, nerve palsy may affect a specific EOM segment, while deficits at the sensory neuronal level may show no specific EOM segment impairment.

6.3 Conclusion and Outlook

The daring dream of being able to differentiate disease etiology - and therefore impact on surgical planning - by determining which EOMs segments are not functional, at the different steps of a disease evolution, now seems possible. The new insights into the pathophysiological processes of loss and regain of muscular function due to metabolic or neuronal diseases may enable the categorization of diseases such as neural palsy, impaired neuromuscular transmission, and mechanical restriction of the EOMs. A detailed understanding of abnormal ocular motility in individual patients will facilitate diagnostic and management procedures, enable earlier diagnosis, and prevent inconveniences for patients.

These improvements would be also applicable outside of ophthalmologic practice. Models of musculoskeletal systems are broadly used to study disorders and to simulate surgical treatments. MRI data from individual subjects are revolutionizing the field of musculoskeletal modeling, by expanding the accuracy and utility of models used to study musculoskeletal and neuromuscular impairments.[Blemker, et al. 2007] Biomechanical parameters derived from MRI measurements - such as the viscoelasticity of the vitreous - can be included in dynamical models to achieve consistent and realistic representations of the anatomy and physiology.[Wei and Pai 2008] The animation of biological-like surrogates based on the simulation of realistic physiology and control will, as a result, be specified at a much higher level and will automatically reproduce important features such as dynamic constraints.[Wei, et al. 2010] Modeling procedures would greatly benefit from the new observables at disposition.

Surgical modeling applicable to individual patients could assist the physician in planning and execution of the optimal procedure, replacing thereby “trial and error” approaches. By minimizing the number of surgeries per patient, healthcare costs should be reduced.

References

Abd-Elmoniem K. Z., Stuber M., Osman N. F. and Prince J. L.
2005 ZHARP: three-dimensional motion tracking from a single image plane. *Inf Process Med Imaging* 19:639-51.

Abd-Elmoniem K. Z., Sampath S., Osman N. F. and Prince J. L.
2007 Real-time monitoring of cardiac regional function using fastHARP MRI and region-of-interest reconstruction. *IEEE transactions on bio-medical engineering* 54(9):1650-6.

Abramoff M. D., Van Gils A. P. G., Jansen G. H. and Mourits M. P.
2000 MRI dynamic color mapping: A new quantitative technique for imaging soft tissue motion in the orbit. *Invest Ophthalmol Vis Sci* 41(11):3256-3260.

Aguayo J., Glaser B., Mildvan A., Cheng H. M., Gonzalez R. G. and Brady T.
1985 Study of vitreous liquifaction by NMR spectroscopy and imaging. *Invest Ophthalmol Vis Sci* 26(5):692-7.

Ahrens A.
1891 *Die Bewegungen der Augen beim Schreiben*. University of Rostock, Rostock.

Aletras A. H., Ding S., Balaban R. S. and Wen H.
1999 DENSE: displacement encoding with stimulated echoes in cardiac functional MRI. *J Magn Reson* 137(1):247-52.

Amartur S. C. and Vesselle H. J.
1993 A new approach to study cardiac motion: the optical flow of cine MR images. *Magn Reson Med* 29(1):59-67.

Ambrose J. A., Lloyd G. A. and Wright J. E.
1974 A preliminary evaluation of fine matrix computerized axial tomography (Emiscan) in the diagnosis of orbital space-occupying lesions. *Br J Radiol* 47(563):747-51.

Axel L.
1984 Blood-Flow Effects in Magnetic-Resonance Imaging. *American Journal of Roentgenology* 143(6):1157-1166.

Axel L. and Dougherty L.
1989 MR imaging of motion with spatial modulation of magnetization. *Radiology* 171(3):841-845.

Bailey C. C., Kabala J., Laitt R., Weston M., Goddard P., Hoh H. B., Potts M. J. and Harrad R. A.
1993 Cine magnetic resonance imaging of eye movements. *Eye* 7:691-693.

Baltes C., Kozerke S., Hansen M. S., Pruessmann K. P., Tsao J. and Boesiger P.
2005 Accelerating cine phase-contrast flow measurements using k-t BLAST and k-t SENSE. *Magn Reson Med* 54(6):1430-8.

Baltes C., Hansen M. S., Tsao J., Kozerke S., Rezavi R., Pedersen E. M. and Boesiger P.
2008 Determination of peak velocity in Stenotic areas: Echocardiography versus k-t SENSE accelerated MR Fourier velocity encoding. *Radiology* 246(1):249-257.

Barboi A. C. and Barkhaus P. E.
2004 Electrodiagnostic testing in neuromuscular disorders. *Neurologic clinics* 22(3):619-41.

Barmet C., De Zanche N. and Pruessmann K. P.
2008 Spatiotemporal magnetic field monitoring for MR. *Magn Reson Med* 60(1):187-97.

Battocletti J. H., Halbach R. E., Sallescunha S. X. and Sances A.
1981 The Nmr Blood Flowmeter - Theory and History. *Medical Physics* 8(4):435-443.

Bergamin O., Zee D. S., Roberts D. C., Landau K., Lasker A. G. and Straumann D.
2001 Three-dimensional Hess screen test with binocular dual search coils in a three-field magnetic system. *Investigative Ophthalmology & Visual Science* 42(3):660-667.

Bergamin O., Wirth M. G. and Landau K.
2008 Binocular Vertical Rectus Muscle Recession For Comitant Vertical Strabismus. *J. Neuro-Ophthal.* 28(4):296-301.

Bernstein M. A., King K. F. and Zhou X. J.
2004 Phase Contrast. In *Handbook of MRI pulse sequences*, pp. 659-678. Elsevier Academic Press, Amsterdam.

Bettelheim F. A. and Wang T. J.

1976 Dynamic viscoelastic properties of bovine vitreous. *Experimental Eye Research* 23(4):435-41.

Bilaniuk L. T., Schenck J. F., Zimmerman R. A., Hart H. R., Jr., Foster T. H., Edelstein W. A., Goldberg H. I. and Grossman R. I.
1985 Ocular and orbital lesions: surface coil MR imaging. *Radiology* 156(3):669-74.

Bishop P. N.
2000 Structural macromolecules and supramolecular organisation of the vitreous gel. *Progress in Retinal and Eye Research* 19(3):323-44.

Blamire A. M.
2008 The technology of MRI -- the next 10 years? *Br J Radiol* 81(968):601-617.

Blemker S. S., Pinsky P. M. and Delp S. L.
2005 A 3D model of muscle reveals the causes of nonuniform strains in the biceps brachii. *Journal of biomechanics* 38(4):657-665.

Blemker S. S., Asakawa D. S., Gold G. E. and Delp S. L.
2007 Image-based musculoskeletal modeling: Applications, advances, and future opportunities. *Journal of Magnetic Resonance Imaging* 25(2):441-451.

Bloch F.
1946 Nuclear Induction. *Physical Review* 70(7-8):460-474.

Boesiger P., Maier S. E., Kecheng L., Scheidegger M. B. and Meier D.
1992 Visualization and quantification of the human blood flow by magnetic resonance imaging. *Journal of biomechanics* 25(1):55-67.

Botha C., de Graaf T., Root R., Wielopolski P., Schutte S., Post F., van der Helm F. and Simonsz H. J.
2005 Time-varying three-dimensional vector field visualisation for the analysis of retrobulbar fat mobility during eye motion. *Proceedings of the 11th annual conference of the Advanced School for Computing and Imaging*.

Bowman R. L. and Kudravcev V.
1959 Blood Flowmeter Utilizing Nuclear Magnetic Resonance. *Ire Transactions on Medical Electronics* 6(4):267-269.

Bradley W. G., Jr., Waluch V., Lai K. S., Fernandez E. J. and Spalter C.
1984 The appearance of rapidly flowing blood on magnetic resonance images. *AJR Am J Roentgenol* 143(6):1167-74.

Bradley W. G., Jr. and Waluch V.
1985 Blood flow: magnetic resonance imaging. *Radiology* 154(2):443-50.

Brecher G. A.
1934 Die optokinetische Auslösung von Augenrollung und rotatorischen Nystagmus. *Pflügers Arch Ges Physiol* (234):13-28.

Breinin G. M.
1957 Electromyography; a tool in ocular and neurologic diagnosis. II. Muscle palsies. *A.M.A* 57(2):165-75.

Breslau J., Dalley R. W., Tsuruda J. S., Hayes C. E. and Maravilla K. R.
1995 Phased-array surface coil MR of the orbits and optic nerves. *AJNR Am J Neuroradiol* 16(6):1247-1251.

Brookman P. (editor)
2010 *Eadweard Muybridge*. ISBN 9781845378378.

Bryant D. J., Payne J. A., Firmin D. N. and Longmore D. B.
1984 Measurement of flow with NMR imaging using a gradient pulse and phase difference technique. *J Comput Assist Tomogr* 8(4):588-93.

Buchsbaum G., Sternklar M., Litt M., Grunwald J. E. and Riva C. E.
1984 Dynamics of an oscillating viscoelastic sphere: a model of the vitreous humor of the eye. *Biorheology* 21(1-2):285-96.

Busacca A.
1967 Corps Vitre-Biomicroscopie Du Fond de L'Oeil. In *Biomicroscopie et Histopathologie de l'Oeil*, pp. 25-43. Schweizer Druck- und Verlagshaus ed. vol. 3, Zürich.

Büttner-Ennever J. A.
2007 Anatomy of the Oculomotor System. In *Neuro-Ophthalmology: Neuronal Control of Eye Movements*, edited by Straube A. and Büttner U., pp. 1-14. Developments in Ophthalmology. vol. 40, Behrens-Baumann W., general editor. Karger, Basel.

Buyens F., Jolivet O., De Cesare A., Bittoun J., Herment A., Tasu J. P. and Mousseaux E.
2005 Calculation of left ventricle relative pressure distribution in MRI using acceleration data. *Magn Reson Med* 53(4):877-84.

Carr H. Y.

1952 Free Precession Techniques in Nuclear Magnetic Resonance. PhD Thesis, Harvard University, Cambridge, MA.

Carr H. Y. and Purcell E. M.
1954 Effects of Diffusion on Free Precession in Nuclear Magnetic Resonance Experiments. *Physical Review* 94(3):630-638.

Char D. H., Sobel D., Kelly W. M., Kjos B. O. and Norman D.
1985 Magnetic resonance scanning in orbital tumor diagnosis. *Ophthalmology* 92(10):1305-10.

Chen S. I., Chandna A. and Abernethy L. J.
2005 Magnetic susceptibility artifact in orbital magnetic resonance imaging. *Strabismus* 13(1):1-3.

Cho Z. H., Oh C. H., Mun C. W. and Kim Y. S.
1986 Some results of high-flow-velocity NMR imaging using selection gradient. *Magn Reson Med* 3(6):857-62.

Clark R. A. and Demer J. L.
2002 Rectus extraocular muscle pulley displacement after surgical transposition and posterior fixation for treatment of paralytic strabismus. *American journal of ophthalmology* 133(1):119-28.

Clark R. A., Ariyasu R. and Demer J. L.
2004 Medial rectus pulley posterior fixation is as effective as scleral posterior fixation for acquired esotropia with a high AC/A ratio. *American journal of ophthalmology* 137(6):1026-33.

Clayton E. H., Wang Q., Song S. K. and Bayly P. V.
2010 Non-invasive Measurement of Vitreous Humor Stiffness in the Mouse using MR Elastography. In *Joint Annual Meeting ISMRM-ESMRMB*, Stockholm, Sweden.

Coats D. K., Paysse E. A. and Stager D. R.
2000a Surgical management of V-pattern strabismus and oblique dysfunction in craniofacial dysostosis. *J AAPOS* 4(6):338-42.

Coats D. K., Paysse E. A., Towler A. J. and Dipboye R. L.
2000b Impact of large angle horizontal strabismus on ability to obtain employment. *Ophthalmology* 107(2):402-5.

Collins C. C., O'Meara D. and Scott A. B.
1975 Muscle tension during unrestrained human eye movements. *J Physiol* 245(2):351-69.

Conneely M. F., Hacein-Bey L. and Jay W. M.
2008 Magnetic Resonance Imaging of the Orbit. *Seminars in Ophthalmology* 23(3):179-189.

Cormack A. M.
1963 Representation of a Function by Its Line Integrals with Some Radiological Applications. *Journal of Applied Physics* 34(9):2722-&.

Damadian R.
1971 Tumor Detection by Nuclear Magnetic Resonance. *Science* 171(3976):1151-&.

Damadian R., Goldsmith M. and Minkoff L.
1977 Nmr in Cancer .16. Fonar Image of Live Human-Body. *Physiological Chemistry and Physics* 9(1):97-&.

David T., Smye S., Dabbs T. and James T.
1998 A model for the fluid motion of vitreous humour of the human eye during saccadic movement. *Physics in medicine and biology* 43(6):1385-99.

Davis P. C. and Hopkins K. L.
1999 Imaging of the pediatric orbit and visual pathways: computed tomography and magnetic resonance imaging. *Neuroimaging Clin N Am* 9(1):93-114.

Delabarr E. B.
1898 A method of recording eye movements. *Am J Psychol* 9:572-574.

Demer J. L. and Miller J. M.
1995 Magnetic resonance imaging of the functional anatomy of the superior oblique muscle. *Invest Ophthalmol Vis Sci* 36(5):906-13.

Demer J. L.
2001 Clarity of words and thoughts about strabismus. *American journal of ophthalmology* 132(5):757-9.

Demer J. L., Clark R. A., Kono R., Wright W., Velez F. and Rosenbaum A. L.
2002 A 12-year, prospective study of extraocular muscle imaging in complex strabismus. *J Aapos* 6(6):337-47.

Demer J. L.

2002 The orbital pulley system: a revolution in concepts of orbital anatomy. *Annals of the New York Academy of Sciences* 956:17-32.

Demer J. L., Kono R. and Wright W.
2003 Magnetic resonance imaging of human extraocular muscles in convergence. *Journal of neurophysiology* 89(4):2072-85.

Demer J. L., Ortube M. C., Engle E. C. and Thacker N.
2006 High-resolution magnetic resonance imaging demonstrates abnormalities of motor nerves and extraocular muscles in patients with neuropathic strabismus. *Journal of Aapos* 10(2):135-42.

Demer J. L.
2007 Mechanics of the Orbita. In *Neuro-Ophthalmology: Neuronal Control of Eye Movements*, edited by Straube A. and Büttner U., pp. 132-157. Developments in Ophthalmology. vol. 40, Behrens-Baumann W., general editor. Karger, Basel.

Demer J. L., Clark R. A., Lim K. H. and Engle E. C.
2007 Magnetic resonance imaging evidence for widespread orbital dysinnervation in dominant Duane's retraction syndrome linked to the DURS2 locus. *Invest Ophthalmol Vis Sci* 48(1):194-202.

Demer J. L.
2008a Inflection in Inactive Lateral Rectus Muscle: Evidence Suggesting Focal Mechanical Effects of Connective Tissues. *Investigative Ophthalmology & Visual Science*.

Demer J. L.
2008b Inflection in inactive lateral rectus muscle: evidence suggesting focal mechanical effects of connective tissues. *Invest Ophthalmol Vis Sci* 49(11):4858-64.

DeRespinis P. A., Caputo A. R., Wagner R. S. and Guo S.
1993 Duane's retraction syndrome. *Survey of ophthalmology* 38(3):257-88.

Dodge R. and Cline T. S.
1901 The angle velocity of eye movements. *Psychol Rev* 8:145-157.

Dovat L., Lambercy O., Salman B., Johnson V., Milner T., Gassert R., Burdet E. and Leong T. C.
2010 A technique to train finger coordination and independence after stroke. *Disability & Rehabilitation: Assistive Technology* 5(4):279-287.

Drost M. R., Maenhout M., Willems P. J., Oomens C. W., Baaijens F. P. and Hesselink M. K.
2003 Spatial and temporal heterogeneity of superficial muscle strain during in situ fixed-end contractions. *Journal of biomechanics* 36(7):1055-63.

Duane A.
1905 Congenital deficiency of abduction, associated with impairment of adduction, retraction movements, contractions of the palpebral fissure and oblique movements of the eye. *Archives of ophthalmology* 34:133-159.

Dumars S., Andrews C., Chan W. M., Engle E. C. and Demer J. L.
2008 Magnetic resonance imaging of the endophenotype of a novel familial Mobius-like syndrome. *Journal of AAPOS* 12(4):381-9.

Edwards J. H., Hyman R. A., Vacirca S. J., Boxer M. A., Packer S., Kaufman I. H. and Stein H. L.
1985 0.6 T magnetic resonance imaging of the orbit. *AJR Am J Roentgenol* 144(5):1015-20.

Eggert T.
2007 Eye Movement Recordings: Methods. In *Neuro-Ophthalmology: Neuronal Control of Eye Movements*, edited by Straube A. and Büttner U., pp. 15-34. Developments in Ophthalmology. vol. 40, Behrens-Baumann W., general editor. Karger, Basel.

Eisner G.
1982 Clinical anatomy of the vitreous. In *Ocular Anatomy, Embryology, and Teratology*, edited by Jacobiec F. A., pp. 391-424. Harper & Row Publishers, Philadelphia.

Eisner G.
2008 Dr. Sherlock's Vitreous; DVD Supplement to the Goldmann-Lecture 2007. Swiss Ophthalmological Society, Heerbrugg.

Ettl A., Koornneef L., Daxer A. and Kramer J.
1998 High-resolution magnetic resonance imaging of the orbital connective tissue system. *Ophthalmic plastic and reconstructive surgery* 14(5):323-7.

Feinberg D. A., Crooks L. E., Sheldon P., Iii J. H., Watts J. and Arakawa M.
1985 Magnetic Resonance Imaging the Velocity Vector Components of Fluid Flow. *Magnetic Resonance in Medicine* 2(6):555-566.

Fischer S. E., Mckinnon G. C., Maier S. E. and Boesiger P.
1993 Improved myocardial tagging contrast. *Magnetic Resonance in Medicine* 30(2):191-200.

Fischer S. E., McKinnon G. C., Scheidegger M. B., Prins W., Meier D. and Boesiger P.
1994 True myocardial motion tracking. *Magn Reson Med* 31(4):401-13.
Fischer S. E., Stuber M., Scheidegger M. B. and Boesiger P.
1995 Limitations of stimulated echo acquisition mode (STEAM) techniques in cardiac applications. *Magn Reson Med* 34(1):80-91.
Fisher M. R., von Schulthess G. K. and Higgins C. B.
1985 Multiphasic cardiac magnetic resonance imaging: normal regional left ventricular wall thickening. *Am. J. Roentgenol.* 145(1):27-30.
Forbes G. S., Earnest F. t. and Waller R. R.
1982 Computed tomography of orbital tumors, including late-generation scanning techniques. *Radiology* 142(2):387-94.
Forrester J. V., Dick A. D., McMenamin P. G. and Lee W. R.
2002 The Vitreous. In *The Eye: Basic Sciences in Practice*, edited by Elsevier H. S., pp. 204. Edition: 2, illustrated ed. Saunders (W.B.) Co Ltd, London.
Frahm J., Haase A. and Matthaei D.
1986 Rapid NMR imaging of dynamic processes using the FLASH technique. *Magn Reson Med* 3(2):321-7.
Gamper U., Boesiger P. and Kozerke S.
2008 Compressed sensing in dynamic MRI. *Magnetic Resonance in Medicine* 59(2):365-373.
Gariano R. F. and Kim C. H.
2004 Evaluation and management of suspected retinal detachment. *American Family Physician* 69(7):1691-8.
Garroway A. N.
1974 Velocity measurements in flowing fluids by MNR. *Journal of Physics D: Applied Physics* 7(14):L159.
Gawler J., Sanders M. D., Bull J. W., du Boulay G. and Marshall J.
1974 Computer assisted tomography in orbital disease. *Br J Ophthalmol* 58(6):571-87.
Gentry L. R.
1998 Anatomy of the orbit. *Neuroimaging Clin N Am* 8(1):171-94.
Gerthsen C., Kneser H. O. and Vogel H.
1992 Physik - Ein Lehrbuch zum Gebrauch neben Vorlesungen. In *16. Auflage*, pp. 144-148. Springer-Verlag, Berlin.
Gilson W. D., Yang Z., French B. A. and Epstein F. H.
2004 Complementary displacement-encoded MRI for contrast-enhanced infarct detection and quantification of myocardial function in mice. *Magn Reson Med* 51(4):744-52.
Gilson W. D., Yang Z., French B. A. and Epstein F. H.
2005 Measurement of myocardial mechanics in mice before and after infarction using multislice displacement-encoded MRI with 3D motion encoding. *American journal of physiology* 288(3):H1491-7.
Gisladottir S., Loftsson T. and Stefansson E.
2009 Diffusion characteristics of vitreous humour and saline solution follow the Stokes Einstein equation. Graefe's archive for clinical and experimental ophthalmology = Albrecht von Graefes Archiv fur klinische und experimentelle Ophthalmologie 247(12):1677-84.
Glasauer S.
2007 Current Models of the Ocular Motor System. In *Neuro-Ophthalmology: Neuronal Control of Eye Movements*, edited by Straube A. and Büttner U., pp. 158-174. Developments in Ophthalmology. vol. 40, Behrens-Baumann W., general editor. Karger, Basel.
Goh P. S., Gi M. T., Charlton A., Tan C., Gangadhara Sundar J. K. and Amrith S.
2008 Review of orbital imaging. *European Journal of Radiology* 66(3):387-395.
Gonzalez R. G., Cheng H. M., Barnett P., Aguayo J., Glaser B., Rosen B., Burt C. T. and Brady T.
1984 Nuclear magnetic resonance imaging of the vitreous body. *Science* 223(4634):399-400.
Gorospe L., Royo A., Berrocal T., Garcia-Raya P., Moreno P. and Abelairas J.
2003 Imaging of orbital disorders in pediatric patients. *Eur Radiol* 13(8):2012-26.
Greil G. F., Germann S., Kozerke S., Baltes C., Tsao J., Urschitz M. S., Seeger A., Tangcharoen T., Bialkowsky A., Miller S. and Sieverding L.
2008 Assessment of left ventricular volumes and mass with fast 3D cine steady-state free precession k-t space broad-use linear acquisition speed-up technique (k-t BLAST). *Journal of Magnetic Resonance Imaging* 27(3):510-515.
Grover T. and Singer J. R.
1971 Nmr Spin-Echo Flow Measurements. *Journal of Applied Physics* 42(3):938-&.

Haase A., Frahm J., Matthaei D., Hanicke W. and Merboldt K. D.
1986 FLASH imaging. Rapid NMR imaging using low flip-angle pulses. *Journal of Magnetic Resonance (1969)* 67(2):258-266.
Hahn E. L.
1950 Spin Echoes. *Physical Review* 80(4):580.
Hahn E. L.
1960 Detection of Sea-Water Motion by Nuclear Precession. *Journal of Geophysical Research* 65(2):776-777.
Hansen M. S., Baltes C., Tsao J., Kozerke S., Pruessmann K. P., Boesiger P. and Pedersen E. M.
2004 Accelerated dynamic Fourier velocity encoding by exploiting velocity-spatio-temporal correlations. *Magnetic Resonance Materials in Physics Biology and Medicine* 17(2):86-94.
Hansen M. S., Baltes C., Tsao J., Kozerke S., Pruessmann K. P. and Eggers H.
2006 k-t BLAST reconstruction from non-Cartesian k-t space sampling. *Magnetic Resonance in Medicine* 55(1):85-91.
Haslwanter T., Buchberger M., Kaltofen T., Hoerantner R. and Priglinger S.
2005 SEE++: a biomechanical model of the oculomotor plant. *Annals of the New York Academy of Sciences* 1039:9-14.
Hawkes R. C., Holland G. N., Moore W. S., Rizk S., Worthington B. S. and Kean D. M.
1983 NMR imaging in the evaluation of orbital tumors. *AJNR Am J Neuroradiol* 4(3):254-6.
Helmholtz H.
1856 Handbuch der Physiologischen Optik. Voss, Leipzig.
Herrick R. C., Hayman L. A., Taber K. H., DiazMarchan P. J. and Kuo M. D.
1997 Artifacts and pitfalls in MR imaging of the orbit: A clinical review. *Radiographics* 17(3):707-724.
Heuck G.
1879 Uber angeborenenvererbten Beweglichkeits-defect der Augen. . *Klin Monatsbl Augenheilkd* 17:253.
Horton J. C., Tsai R. K., Truwit C. L. and Hoyt W. F.
1990 Magnetic resonance imaging of superior oblique muscle atrophy in acquired trochlear nerve palsy. *American journal of ophthalmology* 110(3):315-6.
Hounsfield G. N.
1973 Computerized Transverse Axial Scanning (Tomography) .1. Description of System. *British Journal of Radiology* 46(552):1016-1022.
Hu X. and Parrish T.
1994 Reduction of field of view for dynamic imaging. *Magn Reson Med* 31(6):691-4.
Huber A.
1962 Electromyography of eye muscles. Transactions of the ophthalmological societies of the United Kingdom 82:455-72.
Huber A.
1980 New techniques in diagnosis of eye muscle palsies: a review. *Journal of the Royal Society of Medicine* 73(2):115-22.
Huey E. B.
1898 Preliminary experiments of the physiology and psychology of reading. *Am J Psychol* 9:575-586.
Huey E. B.
1900 On the psychology and physiology of reading. *Am J Psychol* 11:283-302.
Jaffe M.
1882 Beobaehtungen mit der Pulsuhr von L. Waldenburgt. Nach dem Tode des Verfassers aus dessen naehgelassenen Papieren zusammengestellt. *Archiv f. pathol. Anat.* 90(1):3-42.
Jagla F., Jergelova M. and Riecansky I.
2007 Saccadic eye movement related potentials. *Physiological research / Academia Scientiarum Bohemoslovaca* 56(6):707-13.
Jahnke C., Nagel E., Gebker R., Bornstedt A., Schnackenburg B., Kozerke S., Fleck E. and Paetsch I.
2007 Four-dimensional single breathhold magnetic resonance imaging using kt-BLAST enables reliable assessment of left- and right-ventricular volumes and mass. *Journal of Magnetic Resonance Imaging* 25(4):737-742.
Jampel R. S.
2009 Motion-Encoded MRIs Provide Evidence against Orbital Pulleys. *Invest. Ophthalmol. Vis. Sci.* 51(8):3841-.
Janssen

1876. Bulletin de la Société française de Photographie.

Johnson M. T., Coltz J. D., Hagen M. C. and Ebner T. J.
1999 Visuomotor processing as reflected in the directional discharge of premotor and primary motor cortex neurons. *Journal of neurophysiology* 81(2):875-94.

Katz J., Peshock R. M., McNamee P., Schaefer S., Malloy C. R. and Parkey R. W.
1987 Analysis of spin-echo rephasing with pulsatile flow in 2D FT magnetic resonance imaging. *Magn Reson Med* 4(4):307-22.

Kau H. C., Tsai C. C., Ortube M. C. and Demer J. L.
2006 High-resolution magnetic resonance imaging of the extraocular muscles and nerves demonstrates various etiologies of third nerve palsy. *Am J Ophthalmol*:in press.

Kaufmann H. and Decker W. d.
1995 *Strabismus*. 2., neu bearb. und erw. Aufl. ed. Enke, Stuttgart.

Kawano S. I., Honda Y. and Negi A.
1982 Effects of biological stimuli on the viscosity of the vitreous. *Acta Ophthalmologica (Copenhagen)* 60(6):977-91.

Keele K. D.
1951 Leonardo da Vinci, and the movement of the heart. *Proc R Soc Med* 44(3):209-13.

Keele K. D.
1952 Leonardo da Vinci on the Movement ofthe Heart and Blood, London.

Keele K. D.
1961 Three Early Masters of Experimental Medicine-Erasistratus, Galen and Leonardo da Vinci. *Proc R Soc Med* 54(7):577-88.

Keeler R., Singh A. D. and Dua H. S.
2009 Ophthalmotropes: the eye in motion. *British Journal of Ophthalmology* 93(5):572.

Kono R. and Demer J. L.
2003 Magnetic resonance imaging of the functional anatomy of the inferior oblique muscle in superior oblique palsy. *Ophthalmology* 110(6):1219-1229.

Kouwenhoven M., Hofman M. B. M. and Sprenger M.
1995 Motion Induced Phase Shifts in MR: Acceleration Effects in Quantitative Flow Measurements—A Reconsideration. *Magnetic Resonance in Medicine* 33(6):766-777.

Kozerke S., Hasenkam J. M., Pedersen E. M. and Boesiger P.
2001 Visualization of flow patterns distal to aortic valve prostheses in humans using a fast approach for cine 3D velocity mapping. *Journal of Magnetic Resonance Imaging* 13(5):690-698.

Kozerke S., Tsao J., Razavi R. and Boesiger P.
2004 Accelerating cardiac Cine 3D Imaging using k-t BLAST. *Magnetic Resonance in Medicine* 52(1):19-26.

Kuijer J. P. A.
2000 Myocardial Deformation Measured with Magnetic Resonance Tagging. PhD Thesis, Vrije Universiteit, Amsterdam.

Kumar A., Welti D. and Ernst R. R.
1975 Nmr Fourier Zeugmatography. *Journal of Magnetic Resonance* 18(1):69-83.

Ladecola C.
2004 Neurovascular regulation in the normal brain and in Alzheimer's disease. *Nat Rev Neurosci* 5(5):347-360.

Lajeunie E., Catala M. and Renier D.
1999 Craniosynostosis: from a clinical description to an understanding of bone formation of the skull. *Childs Nerv Syst* 15(11-12):676-80.

Lauterbur P. C.
1973 Image Formation by Induced Local Interactions: Examples Employing Nuclear Magnetic Resonance. *Nature* 242(5394):190-191.

Lee B., Litt M. and Buchsbaum G.
1992 Rheology of the vitreous body. Part I: Viscoelasticity of human vitreous. *Biorheology* 29(5-6):521-33.

Leigh R. J. and Zee D. S.
2006 <<*The*>> *neurology of eye movements*. 4th ed. Oxford University Press, Oxford.

Li G., Zheng Y. and Yang E.
2009 The feasibility of using MR elastography to measure stiffness of eye's muscle. In *26th Annual Scientific Meeting of the ESMRMB*, Antalya, Turkey.

Li K. C., Poon P. Y., Hinton P., Willinsky R., Pavlin C. J., Hurwitz J. J., Buncic J. R. and Henkelman R. M.

1984 MR imaging of orbital tumors with CT and ultrasound correlations. *J Comput Assist Tomogr* 8(6):1039-47.

Lipton M. J., Higgins C. B., Farmer D. and Boyd D. P.
1984 Cardiac imaging with a high-speed Cine-CT Scanner: preliminary results. *Radiology* 152(3):579-582.

Litwiller D. V., Pulido J. S., Kruse S. A., Glaser K. J. and Ehman R. L.
2007 MR Elastography of the Eye: Initial Feasibility In *Joint Annual Meeting ISMRM-ESMRMB*, Berlin, Germany.

Litwiller D. V., Mariappan Y. and Ehman R. L.
2010 MR Elastography of the Ocular Vitreous Body. In *Joint Annual Meeting ISMRM-ESMRMB*, Stockholm, Sweden.

Liu X., Stone M. and Prince J.
2006 Tracking tongue motion in three dimensions using tagged MR images. *Proceedings of the IEEE ISBI*:1372-1375.

Lopata R. G. P., van Dijk J. P., Pillen S., Nillesen M. M., Maas H., Thijssen J. M., Stegeman D. F. and de Korte C. L.
2010 Dynamic imaging of skeletal muscle contraction in three orthogonal directions. *J Appl Physiol* 109(3):906-915.

Lund E. and Halaburt H.
1982 Irradiation dose to the lens of the eye during CT of the head. *Neuroradiology* 22(4):181-4.

Maier S. E., Fischer S. E., McKinnon G. C., Hess O. M., Krayenbuehl H. P. and Boesiger P.
1992a Acquisition and evaluation of tagged magnetic resonance images of the human left ventricle. *Comput Med Imaging Graph* 16(2):73-80.

Maier S. E., Fischer S. E., McKinnon G. C., Hess O. M., Krayenbuehl H. P. and Boesiger P.
1992b Evaluation of left ventricular segmental wall motion in hypertrophic cardiomyopathy with myocardial tagging. *Circulation* 86(6):1919-28.

Maier S. E., Scheidegger M. B., Liu K. and Boesiger P.
1996 Accurate velocity mapping with FAcE. *Magnetic resonance imaging* 14(2):163-171.

Mansfield P. and Maudsley A. A.
1976 Planar Spin Imaging by Nmr. *Journal of Physics C-Solid State Physics* 9(15):L409-&.

Mansfield P. and Maudsley A. A.
1977 Medical imaging by NMR. *Br J Radiol* 50(591):188-194.

Marey E.-J.
1865 Études physiologiques sur les caractères du battement du coeur et les conditions qui le modifient. *Journal de l'anatomie et de la physiologie* II:276.

Marey E.-J.
1866 Études graphiques sur la nature de la contraction musculaire. *Journal de l'anatomie et de la physiologie*:225-242 & 403-416.

Marey E.-J.
1876 Notice sur les titres et travaux scientifiques du Docteur Marey. Typographie Lahure, Paris.

Marey E.-J.
1890 *Le Vol des Oiseaux*. Masson, Paris.

Matteucci P.
1946 I difetti congeniti di abduzione con particolare riguardo alla patogenesi. *Rassegna Italiana D'ottalmologia* 15:345-80.

McVeigh E. R.
1996 MRI of myocardial function: motion tracking techniques. *Magnetic resonance imaging* 14(2):137-50.

Meier D., Maier S. and Bösiger P.
1988 Quantitative flow measurements on phantoms and on blood vessels with MR. *Magnetic Resonance in Medicine* 8(1):25-34.

Meyer C. H., Lasker A. G. and Robinson D. A.
1985 The upper limit of human smooth pursuit velocity. *Vision Research* 25(4):561-3.

Miller J. M. and Robins D.
1987 Extraocular muscle sideslip and orbital geometry in monkeys. *Vision research* 27(3):381-92.

Miller J. M.
1989 Functional anatomy of normal human rectus muscles. *Vision Research* 29(2):223-240.

Miller J. M. and Robins D.
1992 Extraocular muscle forces in alert monkey. *Vision research* 32(6):1099-113.
Miller J. M., Bockisch C. J. and Pavlovski D. S.
2002 Missing lateral rectus force and absence of medial rectus co-contraction in ocular convergence. *Journal of neurophysiology* 87(5):2421-33.
Miller J. M., Rossi E. A., Wiesmair M., Alexander D. E. and Gallo O.
2006 Stability of gold bead tissue markers. *J Vis* 6(5):616-24.
Miller N. R., Kiel S. M., Green W. R. and Clark A. W.
1982 Unilateral Duane's retraction syndrome (Type 1). *Archives of ophthalmology* 100(9):1468-72.
Moore G. E.
1948 Use of Radioactive Diiodofluorescein in the Diagnosis and Localization of Brain Tumors. *Science* 107(2787):569-571.
Moore J. E., Jr., Maier S. E., Ku D. N. and Boesiger P.
1994 Hemodynamics in the abdominal aorta: a comparison of in vitro and in vivo measurements. *J Appl Physiol* 76(4):1520-7.
Moran P. R.
1982 A flow velocity zeugmatographic interlace for NMR imaging in humans. *Magnetic resonance imaging* 1(4):197-203.
Morse O. C. and Singer J. R.
1970 Blood velocity measurements in intact subjects. *Science* 170(3956):440-441.
Moseley I., Brant-Zawadski M. and Mills C.
1983 Nuclear magnetic resonance imaging of the orbit. *British Journal of Ophthalmology* 67(6):333-342.
Müller-Forell W. and Pitz S.
2004 Orbital pathology. *European Journal of Radiology* 49(2):105-142.
Muthupillai R., Lomas D. J., Rossman P. J., Greenleaf J. F., Manduca A. and Ehman R. L.
1995 Magnetic resonance elastography by direct visualization of propagating acoustic strain waves. *Science* 269(5232):1854-7.
Napadow V. J., Chen Q., Wedeen V. J. and Gilbert R. J.
1999 Biomechanical basis for lingual muscular deformation during swallowing. *Am J Physiol Gastrointest Liver Physiol* 277(3):G695-701.
Neal R. E., Bettelheim F. A., Lin C., Winn K. C., Garland D. L. and Zigler J. S., Jr.
2005 Alterations in human vitreous humour following cataract extraction. *Experimental Eye Research* 80(3):337-47.
Nef T., Guidali M. and Riener R.
2009 ARMin III - arm therapy exoskeleton with an ergonomic shoulder actuation. *Applied Bionics and Biomechanics* 6(2):127 - 142.
Nickerson C. S., Park J., Kornfield J. A. and Karageozian H.
2008 Rheological properties of the vitreous and the role of hyaluronic acid. *Journal of biomechanics* 41(9):1840-6.
Niitsu M., Campeau N. G., Holsinger-Bampton A. E., Riederer S. J. and Ehman R. L.
1992 Tracking motion with tagged rapid gradient-echo magnetization-prepared MR imaging. *Journal of Magnetic Resonance Imaging* 2(2):155-163.
Oelhafen M., Schwitter J., Kozerke S., Luechinger R. and Boesiger P.
2006 Assessing arterial blood flow and vessel area variations using real-time zonal phase-contrast MRI. *Journal of Magnetic Resonance Imaging* 23(3):422-429.
Oh S. Y., Clark R. A., Velez F., Rosenbaum A. L. and Demer J. L.
2002 Incomitant strabismus associated with instability of rectus pulleys. *Invest Ophthalmol Vis Sci* 43(7):2169-78.
Osman N. F., Kerwin W. S., McVeigh E. R. and Prince J. L.
1999 Cardiac motion tracking using CINE harmonic phase (HARP) magnetic resonance imaging. *Magnetic Resonance in Medicine* 42(6):1048-1060.
Osman N. F., Sampath S., Atalar E. and Prince J. L.
2001 Imaging longitudinal cardiac strain on short-axis images using strain-encoded MRI. *Magn Reson Med* 46(2):324-34.
Oyster C. W.
1999a *The Human Eye: Structure and Function*. 1st edition ed. Sinauer Associates, Sunderland, Mass.
Oyster C. W.

1999b The Human Eye: Structure and Function, pp. 795, page 536. 1st edition ed. Sinauer Associates, Sunderland, Mass.

Ozkurt H., Basak M., Oral Y. and Ozkurt Y.
2003 Magnetic resonance imaging in Duane's retraction syndrome. *Journal of pediatric ophthalmology and strabismus* 40(1):19-22.

Paetsch I., Foll D., Kaluza A., Luechinger R., Stuber M., Bornstedt A., Wahl A., Fleck E. and Nagel E.
2005 Magnetic resonance stress tagging in ischemic heart disease. *American journal of physiology* 288(6):H2708-2714.

Pai D. K.
2010 Dynamic Simulation of Musculoskeletal Biomechanisms in 3D. Paper presented at the 34th Annual Meeting of the American Society of Biomechanics, Providence, Rhode Island, USA.

Pan L., Prince J. L., Lima J. A. and Osman N. F.
2005 Fast tracking of cardiac motion using 3D-HARP. *IEEE transactions on bio-medical engineering* 52(8):1425-35.

Pan L., Stuber M., Kraitchman D. L., Fritzges D. L., Gilson W. D. and Osman N. F.
2006 Real-time imaging of regional myocardial function using fast-SENC. *Magnetic Resonance in Medicine* 55(2):386-395.

Pappas G. P., Asakawa D. S., Delp S. L., Zajac F. E. and Drace J. E.
2002 Nonuniform shortening in the biceps brachii during elbow flexion. *J Appl Physiol* 92(6):2381-2389.

Pattichis C. S., Schofield I., Merletti R., Parker P. A. and Middleton L. T.
1999 Introduction to this special issue. Intelligent data analysis in electromyography and electroneurography. *Medical engineering & physics* 21(6-7):379-88.

Patz S., Bert R. J., Frederick E. and Freddo T. F.
2007 T(1) and T(2) measurements of the fine structures of the in vivo and enucleated human eye. *Journal of Magnetic Resonance Imaging* 26(3):510-8.

Pauli W.
1924 The question of the theoretical meaning of the satellite of some spectralline and their impact on the magnetic fields. *Naturwissenschaften* 12:741-743.

Pedersen H., Kozerke S., Ringgaard S., Nehrke K. and Kim W. Y.
2009 k-t PCA: Temporally constrained k-t BLAST reconstruction using principal component analysis. *Magnetic Resonance in Medicine* 62(3):706-716.

Petit L., Orssaud C., Tzourio N., Salamon G., Mazoyer B. and Berthoz A.
1993 PET study of voluntary saccadic eye movements in humans: basal ganglia-thalamocortical system and cingulate cortex involvement. *Journal of neurophysiology* 69(4):1009-17.

Pfeifer R., Lungarella M. and Iida F.
2007 Self-Organization, Embodiment, and Biologically Inspired Robotics. *Science* 318(5853):1088-1093.

Pfenninger L., Landau K. and Bergamin O.
2006 Comparison of Harms tangent screen and search coil recordings in patients with trochlear nerve palsy. *Vision research* 46(8-9):1404-10.

Piccirelli M., Luechinger R., Rutz A. K., Boesiger P. and Bergamin O.
2007 Extraocular muscle deformation assessed by motion-encoded MRI during eye movement in healthy subjects. *Journal of vision* 7(14(5)):1-10.

Piccirelli M., Luechinger R., Sturm V., Boesiger P., Landau K. and Bergamin O.
2009a Local deformation of extraocular muscles during eye movement. *Investigative Ophthalmology & Visual Science* 50(11):5189-96.

Piccirelli M., Luechinger R., Sturm V., Boesiger P., Landau K. and Bergamin O.
2009b Author Response: Motion-Encoded MRIs Provide Evidence against Orbital Pulleys. *Invest. Ophthalmol. Vis. Sci.* 51(8):3841-a-3842.

Piccirelli M., Bergamin O., Landau K., Boesiger P. and Luechinger R.
2011 Deformation of the Vitreous during Eye Movement. *NMR Biomed* in press.

Prompers J. J., Jeneson J. A. L., Drost M. R., Oomens C. C. W., Strijkers G. J. and Nicolay K.
2006 Dynamic MRS and MRI of skeletal muscle function and biomechanics. *NMR in Biomedicine* 19(7):927-953.

Pruessmann K. P., Weiger M., Scheidegger M. B. and Boesiger P.
1999 SENSE: Sensitivity encoding for fast MRI. *Magnetic Resonance in Medicine* 42(5):952-962.

Pruessmann K. P., Weiger M., Bornert P. and Boesiger P.

2001a Advances in sensitivity encoding with arbitrary k-space trajectories. *Magnetic Resonance in Medicine* 46(4):638-651.

Pruessmann K. P., Weiger M. and Boesiger P.
2001b Sensitivity encoded cardiac MRI. *J. Cardiov. Magn. Reson.* 3(1):1-9.

Purcell E. M., Torrey H. C. and Pound R. V.
1946 Resonance Absorption by Nuclear Magnetic Moments in a Solid. *Physical Review* 69(1-2):37-38.

Quaia C. and Optican L. M.
2003 Dynamic eye plant models and the control of eye movements. *Strabismus* 11(1):17-31.

Rabi I. I., Zacharias J. R., Millman S. and Kusch P.
1938 A new method of measuring nuclear magnetic moment. *Physical Review* 53(4):318-318.

Redpath T. W., Norris D. G., Jones R. A. and Hutchison J. M.
1984 A new method of NMR flow imaging. *Physics in medicine and biology* 29(7):891-5.

Repetto R., Ghigo I., Seminara G. and Ciurlo C.
2004 A simple hydro-elastic model of the dynamics of a vitreous membrane. *Journal of Fluid Mechanics* 503:1–14.

Repetto R., Stocchino A. and Cafferata C.
2005 Experimental investigation of vitreous humour motion within a human eye model. *Physics in medicine and biology* 50(19):4729-43.

Repetto R.
2006 An analytical model of the dynamics of the liquefied vitreous induced by saccadic eye movements. *Meccanica* 41:101-117.

Robinson D. A.
1963 A Method of Measuring Eye Movement Using a Scleral Search Coil in a Magnetic Field. *IEEE transactions on bio-medical engineering* 10(4):137-145.

Robinson D. A.
1975 A quantitative analysis of extraocular muscle cooperation and squint. *Investigative ophthalmology* 14(11):801-25.

Rontgen W. C.
1895 Ueber eine neue Art von Strahlen. (Vorläufige Mittheilung.). Würzburger Physik.-medic. Gesellschaft

Rutz A.
2008 Advances in Whole-Heart MRI Tagging for the Assessment of Myocardial Motion, ETH Phd Thesis N° 17902, Zurich.

Rutz A. K., Ryf S., Plein S., Boesiger P. and Kozerke S.
2008 Accelerated whole-heart 3D CSPAMM for myocardial motion quantification. *Magn Reson Med* 59(4):755-63.

Ryf S., Spiegel M. A., Gerber M. and Boesiger P.
2002 Myocardial tagging with 3D-CSPAMM. *Journal of Magnetic Resonance Imaging* 16(3):320-325.

Ryf S., Kissinger K. V., Spiegel M. A., Börnert P., Manning W. J., Boesiger P. and Stuber M.
2004a Spiral MR myocardial tagging. *Magnetic Resonance in Medicine* 51(2):237-242.

Ryf S., Tsao J., Schwitter J., Stuessi A. and Boesiger P.
2004b Peak-combination HARP: A method to correct for phase errors in HARP. *Journal of Magnetic Resonance Imaging* 20(5):874-880.

Ryf S., Schwitter J., Spiegel M. A., Rutz A. K., Luechinger R., Crelier G. R. and Boesiger P.
2005 Accelerated tagging for the assessment of left ventricular myocardial contraction under physical stress. *J Cardiovasc Magn Reson* 7(4):693-703.

Ryf S., Rutz A. K., Boesiger P. and Schwitter J.
2006 Is post-systolic shortening a reliable indicator of myocardial viability? An MR tagging and late-enhancement study. *J. Cardiov. Magn. Reson.* 8(3):445-451.

Rzedzian R. R. and Pykett I. L.
1987 Instant images of the human heart using a new, whole-body MR imaging system. *Am. J. Roentgenol.* 149(2):245-250.

Sampath S., Derbyshire J. A., Atalar E., Osman N. F. and Prince J. L.
2003 Real-time imaging of two-dimensional cardiac strain using a harmonic phase magnetic resonance imaging (HARP-MRI) pulse sequence. *Magn Reson Med* 50(1):154-63.

Scheidegger M. B., Maier S. E. and Boesiger P.
1991 FID-Acquired-Echos (FAcE): A short echo time imaging method for flow artefact suppression. *Magnetic resonance imaging* 9(4):517-524.

Schenck J. F., Hart H. R., Foster T. H., Edelstein W. A., Bottomley P. A., Redington R. W., Hardy C. J., Zimmerman R. A. and Bilaniuk L. T.
1985 Improved MR imaging of the orbit at 1.5 T with surface coils. *American Journal of Roentgenology* 144(5):1033-1036.
Schmid P., Stuber M., Boesiger P., Hess O. M. and Niederer P.
1995 Determination of displacement, stress- and strain-distribution in the human heart: a FE-model on the basis of MR imaging. *Technol Health Care* 3(3):209-14.
Schmitt K. U., Schlittler M. and Boesiger P.
2010 Biomechanical loading of the hip during side jumps by soccer goalkeepers. *J. Sports Sci.* 28(1):53-59.
Schoemaker I., Hoefnagel P. P., Mastenbroek T. J., Kolff C. F., Schutte S., van der Helm F. C., Picken S. J., Gerritsen A. F., Wielopolski P. A., Spekreijse H. and Simonsz H. J.
2006 Elasticity, viscosity, and deformation of orbital fat. *Invest Ophthalmol Vis Sci* 47(11):4819-26.
Schovanec L.
2001 Ocular Dynamics and Skeletal Systems. *IEEE control systems magazine* 21(4):70-79.
Schutte S., van den Bedem S. P., van Keulen F., van der Helm F. C. and Simonsz H. J.
2006 A finite-element analysis model of orbital biomechanics. *Vision research* 46(11):1724-31.
Sebag J.
2008 To see the invisible: the quest of imaging vitreous. *Developmental Ophthalmology* 42:5-28.
Sechtem U., Pflugfelder P. W., White R. D., Gould R. G., Holt W., Lipton M. J. and Higgins C. B.
1987a Cine MR imaging: potential for the evaluation of cardiovascular function. *Am. J. Roentgenol.* 148(2):239-246.
Sechtem U., Pflugfelder P. W., Gould R. G., Cassidy M. M. and Higgins C. B.
1987b Measurement of right and left ventricular volumes in healthy individuals with cine MR imaging. *Radiology* 163(3):697-702.
Sheehan F. T., Zajac F. E. and Drace J. E.
1997 Using cine phase contrast magnetic resonance imaging to non-invasively study in vivo knee dynamics. *Journal of biomechanics* 31(1):21-26.
Shin G. S., Demer J. L. and Rosenbaum A. L.
1996 High resolution, dynamic, magnetic resonance imaging in complicated strabismus. *Journal of Pediatric Ophthalmology & Strabismus* 33(6):282-290.
Simonsz H. J., Harting F., Dewaal B. J. and Verbeeten B. W. J. M.
1985 Sideways displacement and curved path of recti eye muscles. *Archives of Ophthalmology* 103(1):124-128.
Simonsz H. J.
2004 Christian Theodor Georg Ruete: The first strabismologist, coauthor of Listing's Law, maker of the first ophthalmotrope and inventor of indirect fundoscopy. *Strabismus* 12(1):53-57.
Singer J. R.
1959 Blood Flow Rates by Nuclear Magnetic Resonance Measurements. *Science* 130(3389):1652-1653.
Singer J. R.
1978 Nmr Diffusion and Flow Measurements and an Introduction to Spin Phase Graphing. *Journal of Physics E-Scientific Instruments* 11(4):281-291.
Singer J. R. and Crooks L. E.
1983 Nuclear Magnetic-Resonance Blood-Flow Measurements in the Human-Brain. *Science* 221(4611):654-656.
Sinha S., Hodgson J. A., Finni T., Lai A. M., Grinstead J. and Edgerton V. R.
2004 Muscle kinematics during isometric contraction: Development of phase contrast and spin tag techniques to study healthy and atrophied muscles. *Journal of Magnetic Resonance Imaging* 20(6):1008-1019.
Sklavos S., Porrill J., Kaneko C. R. and Dean P.
2005 Evidence for wide range of time scales in oculomotor plant dynamics: implications for models of eye-movement control. *Vision research* 45(12):1525-42.
Smolorz J., Sechtem U., Linden A. and Schicha H.
1988 Nuclear magnetic resonance imaging of the heart. *European Journal of Nuclear Medicine and Molecular Imaging* 13(12):653-660.
Sobel D. F., Mills C., Char D., Norman D., Brant-Zawadzki M., Kaufman L. and Crooks L.

1984 NMR of the normal and pathologic eye and orbit. *AJNR Am J Neuroradiol* 5(4):345-50.
Sobel D. F., Kelly W., Kjos B. O., Char D., Brant-Zawadzki M. and Norman D.
1985 MR imaging of orbital and ocular disease. *AJNR Am J Neuroradiol* 6(2):259-64.
Soellinger M., Ryf S., Boesiger P. and Kozerke S.
2007 Assessment of human brain motion using CSPAMM. *Journal of Magnetic Resonance Imaging* 25(4):709-14.
Spielberg S.
1934 Einfluss der Ermüdung auf den Gang. *Arbeitsphysiologie* 7:555-576.
Stefansson E.
2009 Physiology of vitreous surgery. Graefe's archive for clinical and experimental ophthalmology = Albrecht von Graefes Archiv fur klinische und experimentelle Ophthalmologie 247(2):147-63.
Stocchino A., Repetto R. and Cafferata C.
2007 Eye rotation induced dynamics of a Newtonian fluid within the vitreous cavity: the effect of the chamber shape. *Physics in medicine and biology* 52(7):2021-34.
Stone M., Davis E. P., Douglas A. S., NessAiver M., Gullapalli R., Levine W. S. and Lundberg A.
2001 Modeling the motion of the internal tongue from tagged cine-MRI images. *The Journal of the Acoustical Society of America* 109(6):2974-2982.
Straube A. and Büttner U. (editors)
2007 Neuro-Ophthalmology: Neuronal Control of Eye Movements. 40. Karger, Basel.
Stuber M., Nagel E., E. Fischer S., Spiegel M. A., Scheidegger M. B. and Boesiger P.
1998 Quantification of the local heartwall motion by magnetic resonance myocardial tagging. *Computerized Medical Imaging and Graphics* 22(3):217-228.
Stuber M., Spiegel M. A., Fischer S. E., Scheidegger M. B., Danias P. G., Pedersen E. M. and Boesiger P.
1999a Single breath-hold slice-following CSPAMM myocardial tagging. *MAGMA* 9(1-2):85-91.
Stuber M., Fischer S. E., Scheidegger M. B. and Boesiger P.
1999b Toward high-resolution myocardial tagging. *Magnetic Resonance in Medicine* 41(3):639-643.
Stuber M., Scheidegger M. B., Fischer S. E., Nagel E., Steinemann F., Hess O. M. and Boesiger P.
1999c Alterations in the Local Myocardial Motion Pattern in Patients Suffering From Pressure Overload Due to Aortic Stenosis. *Circulation* 100(4):361-368.
Suryan G.
1951 Nuclear resonance in flowing liquids. *Proc Indian Acad Sci [A]* 33:107-111.
Sweeney J. A., Luna B., Keedy S. K., McDowell J. E. and Clementz B. A.
2007 fMRI studies of eye movement control: investigating the interaction of cognitive and sensorimotor brain systems. *NeuroImage* 36 Suppl 2:T54-60.
Swindle K. E., Hamilton P. D. and Ravi N.
2008 In situ formation of hydrogels as vitreous substitutes: Viscoelastic comparison to porcine vitreous. *Journal of Biomedical Materials Research Part A* 87(3):656-65.
Tillery S. I. H. and Taylor D. M.
2004 Signal acquisition and analysis for cortical control of neuroprosthetics. *Current Opinion in Neurobiology* 14(6):758-762.
Tsao J., Boesiger P. and Pruessmann K. P.
2003 k-t BLAST and k-t SENSE: Dynamic MRI with high frame rate exploiting spatiotemporal correlations. *Magnetic Resonance in Medicine* 50(5):1031-1042.
Tsao J., Kozerke S., Boesiger P. and Pruessmann K. P.
2005 Optimizing spatiotemporal sampling for k-t BLAST and k-t SENSE: Application to high-resolution real-time cardiac steady-state free precession. *Magnetic Resonance in Medicine* 53(6):1372-1382.
Tsao J., Boesiger P. and Pruessmann K. P.
2006 Lattice permutation for reducing motion artifacts in radial and spiral dynamic imaging. *Magnetic Resonance in Medicine* 55(1):116-125.
Tweed D. and Vilis T.
1990 Geometric relations of eye position and velocity vectors during saccades. *Vision research* 30(1):111-27.
Underwood S. R.
1989 Cine magnetic resonance imaging and flow measurements in the cardiovascular system. *British Medical Bulletin* 45(4):948-967.
van de Graaf E. S., Felius J., van Kempen-du Saar H., Looman C. W., Passchier J., Kelderman H. and Simonsz H. J.

2009 Construct validation of the Amblyopia and Strabismus Questionnaire (A&SQ) by factor analysis. Graefe's archive for clinical and experimental ophthalmology = Albrecht von Graefes Archiv fur klinische und experimentelle Ophthalmologie 247(9):1263-8.

van den Bedem S. P., Schutte S., van der Helm F. C. and Simonsz H. J.
2005 Mechanical properties and functional importance of pulley bands or 'faisseaux tendineux'. *Vision research* 45(20):2710-4.

van Dijk P.
1984 Direct cardiac NMR imaging of heart wall and blood flow velocity. *J Comput Assist Tomogr* 8(3):429-36.

Van Dijk P., van der Meulen P., Pettigrew R. I., Bliimm R., Dannels W. and Doombos J.
1986 Dynamic studies of cardiac motion and flow with a fast multiphase MRI technique (Abstr.). *Journal of the American College of Cardiology* 7:197A.

Vappou J., Breton E., Choquet P., Goetz C., Willinger R. and Constantinesco A.
2007 Magnetic resonance elastography compared with rotational rheometry for in vitro brain tissue viscoelasticity measurement. *Magnetic Resonance Materials in Physics, Biology and Medicine* 20(5-6):273-8.

Vitanis V., Manka R., Boesiger P. and Kozerke S.
2009 Accelerated cardiac perfusion imaging using k-t SENSE with SENSE training. *Magn Reson Med* 62(4):955-65.

Wakeling J. M.
2009 The recruitment of different compartments within a muscle depends on the mechanics of the movement. *Biology Letters* 5(1):30-34.

Waldenburg L.
1878 Pulsuhr und Puls. *Berl. klin. Wochenschr* 15:696-702, 712-716.

Walsh F. B. and Hoyt W. F.
2005 Walsh and Hoyt's clinical neuro-ophthalmology. In *Volume 1: Visual Sensory System*, edited by Miller N. R., pp. 1009-1015. 6th ed. vol. 1. Lippincott Williams & Wilkins, Baltimore, Md. etc.

Walton K. A., Meyer C. H., Harkrider C. J., Cox T. A. and Toth C. A.
2002 Age-related changes in vitreous mobility as measured by video B scan ultrasound. *Experimental Eye Research* 74(2):173-80.

Webber A. L. and Wood J.
2005 Amblyopia: prevalence, natural history, functional effects and treatment. *Clinical and Experimental Optometry* 88(6):365-375.

Weber K. P., Bockisch C. J., Bergamin O., Landau K. and Straumann D.
2005 Modulation of saccade curvature during Bielsehowsky head-tilt testing in patients with unilateral trochlear nerve palsy and healthy subjects. *Journal of the Neurological Sciences* 238:S48.

Weber O. M., Eggers H., Spiegel M. A., Scheidegger M. B., Proksa R. and Boesiger P.
1999 Real-time interactive magnetic resonance imaging with multiple coils for the assessment of left ventricular function. *JMRI-J. Magn. Reson. Imaging* 10(5):826-832.

Weber W. E. and Weber E. F.
1992 Mechanics of the human walking apparatus. Transl. from the German Mechanik der menschlichen Gehwerkzeuge, Göttingen 1836,. Translated by Maquet P. and Furlong R. Springer Berlin.

Wei Q. and Pai D. K.
2008 Physically consistent registration of extraocular muscle models from MRI. *Conf Proc IEEE Eng Med Biol Soc* 2008:2237-41.

Wei Q. and Pai D. K.
2009 Longitudinal strain estimation in incompressible cylindrical tissues from magnetic resonance imaging. *Conf Proc IEEE Eng Med Biol Soc* 2009:7159-63.

Wei Q., Sueda S. and Pai D. K.
2010 Biomechanical simulation of human eye movement. Paper presented at the International Symposium on Biomedical Simulation.

Weiger M., Pruessmann K. P. and Boesiger P.
2000 Cardiac real-time imaging using SENSE. SENSitivity Encoding scheme. *Magn Reson Med* 43(2):177-84.

Weiger M., Pruessmann K. P. and Boesiger P.
2002 2D SENSE for faster 3D MRI. Magnetic Resonance Materials in Physics Biology and Medicine 14(1):10-19.

Weiss G.

1906 Die Chronophotographie. *Ergebnisse der Physiologie* 5(19):291-318.

White H. E. and Levatin P.
1962 "Floaters" in the eye. *Scientific American* 206:119-27.

Windhorst U.
2007 Muscle proprioceptive feedback and spinal networks. *Brain Research Bulletin* 73(4-6):155-202.

Wong A. M., Sharpe J. A. and Tweed D.
2002 Adaptive neural mechanism for listing's law revealed in patients with fourth nerve palsy. *Invest Ophthalmol Vis Sci* 43(6):1796-803.

Wong I., Leo S. W. and Khoo B. K.
2005 Loop myopexy for treatment of myopic strabismus fixus. *J AAPOS* 9(6):589-91.

Worst J. G. F. and Los L. I.
1995 *Cisternal Anatomy of the Vitreous*. Kugler Publications, Amsterdam.

Worthington B. S., Doyle M., Chapman B., Turner R., Ordidge R. J., Cawley M., Coxon R., Glover P., Coupland R. E., Morris G. K. and Mansfield P.
1986a Real-time cardiac imaging of adults using variations of echo-planar imaging (abstract). *Radiology* 161 (P):338.

Worthington B. S., Wright J. E., Curati W. L., Steiner R. E. and Rizk S.
1986b The role of magnetic resonance imaging techniques in the evaluation of orbital and ocular disease. *Clin Radiol* 37(3):219-26.

Wrenn F. R., Good M. L. and Handler P.
1951 The Use of Positron-Emitting Radioisotopes for the Localization of Brain Tumors. *Science* 113(2940):525-527.

Xu J., Heys J. J., Barocas V. H. and Randolph T. W.
2000 Permeability and diffusion in vitreous humor: implications for drug delivery. *Pharmaceutical Research* 17(6):664-9.

Yee R. D., Goldberg R. A., Jones O. W., Baloh R. W. and Honrubia V.
1983 Effect of eccentric gaze on pursuit. *Investigative Ophthalmology & Visual Science* 24(8):1108-1114.

Yuksel D., Optican L. M. and Lefevre P.
2005 Properties of saccades in Duane retraction syndrome. *Invest Ophthalmol Vis Sci* 46(9):3144-51.

Zerhouni E. A., Parish D. M., Rogers W. J., Yang A. and Shapiro E. P.
1988 Human heart: Tagging with MR imaging - A method for noninvasive assessment of myocardial motion. *Radiology* 169(1):59-63.

Zhong X., Epstein F. H., Spottiswoode B. S., Helm P. A. and Blemker S. S.
2008 Imaging two-dimensional displacements and strains in skeletal muscle during joint motion by cine DENSE MR. *Journal of biomechanics* 41(3):532-540.

Zimmerman R. A., Bilaniuk L. T., Yanoff M., Schenck J. F., Hart H. R., Foster T. H., Edelstein W. A., Bottomley P. A., Redington R. W. and Hardy C. J.
1985 Orbital magnetic resonance imaging. *American journal of ophthalmology* 100(2):312-7.

Zimmerman R. L.
1980 In vivo measurements of the viscoelasticity of the human vitreous humor. *Biophysics Journal* 29(3):539-44.

Acknowledgment

Many people have contributed to this work in one way or another. My heartfelt thanks go to …

Oliver Bergamin-Rémy and Roger Luechinger, for their enthusiastic cooperation, unlimited trust, and countless lessons. Special thanks also for the extreme freedom during my PhD studies, which allowed me to express my scientific curiosity and lively interests, and most of all, for the pleasure of discovering.

Prof. Peter Boesiger, head of the Institute for Biomedical Engineering (ETH) and Prof. Klara Landau, head of the Ophthalmology Department (USZ), for the opportunity to work in an excellent scientific environment, their faith in our work, steady support in every respect and thorough supervision.

Christof Baltes, Christopher Bockish, Gérard Crelier, Nicola De Zanche, Maria Del Carmen Fuentes, Prof. Sebastian Kozerke, Jurek Massner-Nordmeyer, Prof. Klaas Prüssmann, Andrea Rutz, Salome Ryf, Michaela Soellinger, Veit Sturm, Michael Wyss, for answering my questions, providing know-how, support, and enthusiasm, as well as for the relaxing coffee-breaks and good times.

Evelyne Balteau, Christof Barmet, Marianne Berg, Diane-Elise Bettendorff-Bakman, David Brunner, Martin Bührer, Xing Chen, Anna Cholinska, Jelena Curcic, Maha El-Zein, Rudolf Fischer, Alex Fuchs, Urs Gamper, Patric Hagmann, Tobias Hahn, Susanne Heinzer-Schweizer, Anke Henning, Andreas Hock, Maximilian Häberlin, Marco Jauslin, Lars Kasper, Verena Knobloch, Marcin Krajewski, Thomas Lange, Yves Lehareinger, Hendrik Mandelkow, Robert Manka, Dieter Meier, Prof. Peter and Eva Niederer, Jan Paska, Matteo Pavan, Sandrine Pernet, Carolin Reischauer, Prof. Markus Rudin and his group, Najat Salameh, Michael Schär, Carsten Schirra, Conny Schmidt, Johannes Schmidt, Kai-Uwe Schmitt, Betina and Vinzenz Schnepf, Rolf Schulte, Esther Singer, Philipp Stämpfli, Christian Stoeck, Reto Treier, Astrid van Lier, Johanna Vannesjö, Viton Vitanis, Jochen von Spiczak, Robert Vorburger, Prof János Vörös and his group, Kilian Weiss, Florian Wiesinger, Bruno Willi, Bertram Wilm, and many more, for friendly, exciting, and inspiring working atmosphere, and/or great moments of fun during my PhD time.

Nathalia, for fighting hard times and still smiling, and for being such a nice mother for our kids.

Danaé and Nephélie, for the joyful expressions even when I come home late.

My Parents and my big Family.

The Swiss National Science Foundation (SNF #3100AO-102197) for grant support.

The technical and financial support of Philips Healthcare, Best, NL.

Curriculum Vitae

Marco Piccirelli was Born on September 30th 1977 as the second son of Anita Rosina Angelucci and Antonio Piccirelli (from Torricella Peligna (CH), Italy – a beautiful small town facing the Maiella and the Adriatic Sea), and grew up in the neighborhood of Lausanne, Switzerland, on the *Lac Léman.*

After getting his Matura Type C (Sciences) from the *Gymnase Cantonale du Bugnon* in Lausanne, he started in 1996 his studies in Physics at the *Eidgenössische Technische Hochschule* (ETH) in Zurich. In spring 2001, he graduated after having completed his diploma thesis on solar cells in the Lab of Prof. Michael Grätzel.

In 2001, he compiled a Postgraduate Program in Biomedical Engineering with six months Internship in the Computed Tomography Lab at the *General Electric - Global Research Center* in Niskayuna (NY), USA. Work continued under the supervision of Prof. Reto Meuli during his 21 months long civil-service for Switzerland. Subsequently, he started the Didactic and Pedagogy Program of the *ETH Zürich* in Mathematics and Physics.

From 2004 to 2009 he also took charge of the management of the *Société Coopérative d'Habitation Lausanne,* an important real estate corporation, as President of the Control Board and Administrative Board Member.

Since 2005 he joined as a teaching and research assistant the *Institute for Biomedical Engineering* of the *University and ETH Zürich* in the Biophysics group of Prof. Peter Boesiger. His research, in very close collaboration with PD Dr. Oliver Bergamin-Rémy of the *Ophthalmology Department* of the *University Hospital Zurich*, was focused on magnetic resonance imaging of the orbit during eye movement.

From April 2009, he is full time appointed as Group Leader for Physics at the *Laboratory for Social and Neural Systems Research (SNS Lab)* of the *Department of Economics* of the *University of Zürich*, founded by Prof. Ernst Fehr and Prof. Klaas E. Stephan, where he leads the MR methodology developments.

Marco Piccirelli is also President of several scientific associations, married to Nathalia Piccirelli-Giontsis since 2009, and father of two sweet little girls named Danaé Thalia (*05.10.2009) and Nephélie Maria (*05.04.2011).

May, 2011.